UNIWERSYTET WARSZAWSKI

Wydział Fizyki

ROZPRAWA DOKTORSKA

Optimization of glass properties devoted to multi-thermal processes: Toward mid-infrared photonic components

Xavier Forestier

Doctoral dissertation prepared under the supervision of:

Prof. dr hab. inż. Ryszard Buczyński

University of Warsaw, Faculty of Physics, Poland

Acknowledgments

This thesis would not have existed without the support of the funding program of the European Union H2020 Innovative Training Network SUPUVIR (SUPercontinuum broadband light sources covering UV to IR applications).

First of all, I would like to thank my supervisor prof. dr. hab. inż. Ryszard Buczyński for giving me the opportunity to get into this prestigious Marie Sklodowska-Curie program. I would also like to thank dr. hab. inż. Mariusz Klimczak from Faculty of Physics, University of Warsaw for his help. The moments we have spent abroad together drinking wine and eating at Michelin star restaurants will not be forgotten. I hope you will remember the tables I've brought you to.

Thanks, Jarek for your full-time supervision for a year and a half! I do not know where I would be without your supervision. I would also like to thank Gregorz for his amazing personality and for his countless help with optical setups and measurements, you taught me so much. Thank you, Adam, for your positive energy and your help. The lab would not have been the same without my new glass scientist's dear friend Przemek, for all the interesting exchanges we have had!

I would also like to express my sincere gratitude to Pr. Troles for his amazing supervision during my secondment at the Glass and Ceramic group at the University of Rennes 1 as well to Guillaume Huss for taking so much time explaining me how to measure the generation of supercontinuum.

Special mention to Darek to teach me how to stack nanostructured core photonic crystal fibers, it is something quite epic to achieve once you stack your first preform! I will never forget this moment (thanks for the last line though). I cannot express enough my gratitude to Andrej for his invaluable insight in glass melting. Thanks for sharing these decades of experience. Thanks, Robert, for the polishing! Thank you, Anna, for your kindness and your smile, thanks so much to your amazing husband for helping with the furnaces, the home-made preform and the glove box.

Among the PhD students, I would like to thank Iurii for his humor and friendship, Mattia, Lily and Thuy for their joy and kindness as well as Damian for his rock-solid help.

I want to thank Damian again and my other friends outside of the labs for helping me going through my broken knee and the 2 months in the bed without walking. I could not have survived without the few of you guys! Thanks to my dear brother Ali for taking a plane from Los Angeles helping me for a week and my deep gratitude to Dorota for taking a plane from London…twice! Love you guys, I will never forget!

My amazing Polish experience would have been nothing without Ali (my dear brother), Alan (my other mother brother), Agustina (my crazy sista from South America), Lydia (my favorite sista to party and talk about philosophy), Dorota for being the amazing human being you are, for your constant support and help. I will never forget the long chats we had. I am so happy to have crossed your path, someday, coming back from Finland in a metro in Paris, finally ending up in the same plane to Warszawa and having fun, you are family! Finally, I would like to thank Edyta for sharing so much these years, you are forever in my heart! I would like to give a special thanks to my SUPUVIRA's fellows, especially to Marcello, Solveig, Etienne, Iurii, Manoj, Chetan, Abba, Kyei and Amar. I have so much crazy memories with you guys, I will never forget our workshops spent together.

Thx BouchBouch ainsi qu'à ta sœur Rana pour les corrections et le temps pris à lire ma thèse. Je vous dois un restaurant (3 étoiles).

To Solveig, my Dr. Sista! I cannot even recount the number of times that we have ended up laughing together uncontrollably, even in the middle of conferences. Your friendship, your patience, your amazing brain and your help have been so valuable. Thank you for being my friend!

To my "chéri" Dr. Etienne, your smile, your intelligence, your friendship "sans-faille" font de toi un frère! Je suis heureux et fier de t'avoir rencontré et de pouvoir compter sur toi. Merci pour ton amitié et l'aide précieuse sur les bases de l'optique non-linéaire.

To my dear friend, Dr. Marcello. You gave me the strength and the trust that I can only expect from a brother! Meeting you was life changing as you are one of the most brilliant minds that I have ever met! I will never forget our nights brainstorming about the world around a nice bottle of wine (or two… and of course nice food), as well as the tremendous work we have achieved at the university of Rennes 1 under the outstanding supervision of Pr. Troles for these nGRIN chalcogenide fibers.

Thanks to the Gamma Shield© team for helping me through this PhD and for your many ideas. I love you guys!

To Edyta, thank you so much for supporting me all these years. It is not easy to live with a PhD student sometimes. Thank you for bringing me joy and so much fun. Thank you for making me understand the great Polish culture better.

To my dad who died during my PhD and could not have the chance to see me achieve a long familial tradition! All my love, dad!

I have no word to express my love for my mother without whom none of this would have been possible. Thank you for your endless support and trust! Thank you for being who you are, thank you for your tremendous culture, thank you for your openness. I discovered the world because of you, and will continue to do so…

I dedicate this thesis to my mother…

Acronyms:

ANDi	All-normal dispersion
BS	Beam splitter
BSE	Backscattered electron
CTE	Coefficient of thermal expansion
DSC	Differential scanning calorimetry
DTA	Differential thermal analysis
EDS	Energy-dispersive x-ray spectroscopy
EM	Electromagnetic wave
EMT	Effective medium theory
FLIR	Forward looking infrared
FWM	Four waves mixing
GAS	Ga-As-Se
GNLSE	Generalized non-linear Schrödinger equation
HMFG	Heavy metal fluoride glasses
HMO	Heavy metal oxide
HMOG	Heavy metal oxide glasses
HSM	Hot-stage microscopy
IR	Infrared
LMA	Large mode area
MCT	Mercury-Cadmium-Telluride
MCVD	Modified chemical vapor deposition
MI	Modulation instability
Mid-IR	Mid-infrared
NA	Numerical aperture
nGRIN	Nanostructured gradient index
NLSE	Non-linear Schrödinger equation
OPD	Optical path difference
OPO	Optical parametric oscillator
OSA	Optical spectrum analyzer
RAP	Reactive atmosphere processing
RI	Refractive index
SC	Supercontinuum
SCG	Supercontinuum generation
SE	Secondary electron
SEM	Scanning electron microscopy
SPCG	SiO_2-PbO-CdO-Ga_2O_3
SPM	Self-phase modulation
TMFG	Transition metal fluoride glasses
TIR	Total internal reflection
TMA	Thermomechanical analysis
TZN	TeO_2-ZnO-Na_2O
UV	Ultraviolet
WDS	Wavelength dispersive spectrometry
ZDW	Zero dispersion wavelength

Table of contents

Introduction

Obsidian, a glass naturally occurring during volcanic activities, is one of the first use the humankind had with amorphous materials, tools and weapons. The first trace of human manufacturing glasses gets back to Egypt and Mesopotamia 5000 BC and were mostly used as art pieces until recently. Since then, it went from an art material to a technical material allowing a wide range of applications, from military defense to medicine, optics and even mechanics. The last 50 years, information optic led to a wide use of optical fibers to transmit information and to produce light sources and sensing apparatus. The need of glasses with appropriate physico-chemical properties such as the thermal and optical properties is growing as the applications appear. A new type of optical fibers emerged in the 1990's, photonic crystal fibers (PCF), allowing to tailor the dispersion profile to fully exploit the non-linear properties of glasses. Recently, a new type of method emerged to produce all-solid nanostructured fibers, giving a clear mechanical advantage over holey PCFs due to the all-solid nature of the fibers, enabling robust industry accepted components, especially important for biosensing or imagery.

Purposes of the thesis and problematics

In this thesis, the difficulty to synthetize heavy metal oxide glasses (HMOG), thermally stable enough to produce cost-effective lenses by the hot embossing method for applications from visible to mid-infrared (mid-IR) up to 5 to 7 µm was first addressed. Indeed, the vast majority of glasses either crystallize or crack during the thermal and mechanical treatments induced by the hot-embossing method. For this reason, a new glass system was developed during my thesis, namely SiO_2-PbO-CdO-Ga_2O_3. This glass system has shown to have large thermal stability, allowing the thermally intensive production of optical elements. The possibility to extend the transmission spectra of a sub-family of HMOGs, tellurites glasses, was then investigated by dehydrating them using fluorides and chlorides, which could extend their transmission from 3 µm to 5.5 µm in optical fibers.

Secondly, we addressed the difficulty to produce nanostructured graded index fibers and microlenses from chalcogenides glasses by the stack and draw method due to their tendency to crystallize and the difficulty to easily design their dispersion profile with a zero-dispersion wavelength (ZDW) generally situated around 6-7 µm. Chalcogenides glasses present a very large transmission from 1 µm to 20 µm, making them particularly appropriate for mid-IR applications. The stack and draw method, usually used for stable soft glasses such as silicates, has shown to be impractical with chalcogenides glasses so far, due to their lack of thermal stability. For the first time, chalcogenides-based nGRIN fibers were developed by the stack and draw method as well as microlenses for applications from 1 µm to 17 µm.

Finally, the validity of nGRIN fibers for the generation of supercontinuum from visible to mid-IR was investigated. The versatility offered by the core nanostructuration by the stack and draw method for dispersion management allows the usage of commercially available pump sources, allowing spectral broadening more easily for fibers with a ZDW in the mid-IR above 5 µm. This is especially true for chalcogenides glasses as mentioned previously. For this purpose, two similar nanostructuration processes with two different glass families were compared, silica-based fibers called MS15B3 previously produced at the Institute of Electronic Materials Technology (ITME), based on commercial fused silica with GeO_2

doped-silicate glasses, and chalcogenide fibers developed at the University of Rennes 1 and ITME for applications up to 7 µm.

The large difference of transmission and nonlinearity allows to compare the supercontinuum generation with similar structure but different regime which could lead to various applications due their vastly different transmission range. The stack and draw methods and the nanostructuration simulations used for the production of both types of fibers were the same.

Claims

-We can synthetize new heavy metal oxides glasses (HMOG) with improved thermal stability to produce cost effective lenses by the hot embossing method for applications from the visible up to 6 µm.

-We can extend the transmission of tellurite glasses by lowering the water content (limiting their transmission to 3 µm due to hydroxyl groups and free water), using halides compounds to produce optical fibers by the stack and draw method for applications up to 5.5 µm.

-We can nanostructure all-solid nGRIN fibers made of chalcogenide glasses to effectively design the dispersion profile, allowing the use of pump sources over a wide range of wavelengths to obtain mid-IR supercontinuum generation.

This thesis comprises the original research results obtained during the author's Ph.D. studies as well as his contribution to address the thesis mentioned before and is divided into the following chapters:

Chapter 1 - The vitreous state: this chapter focuses on the current state of the art of glassy material. A wide overview of the glass nature, the various glass families, and their properties will be exposed. Their typical physicochemical properties will be presented as well as their optical properties. Nonlinear properties involved in spectral broadening in optical fibers will also be presented in a second time in this chapter.

Chapter 2 - Methods of characterization of glassy materials: this chapter focuses on the various methods of characterization used for glassy materials. The most important physico-chemical properties measurements methods for optical glasses are presented from viscosity to transition temperature, coefficient of thermal expansion, transmission, refractive index or material dispersion. These measurements are critical for the development of optical elements considering the processes involved in the production of optical fibers and microlenses. Indeed, the multiple thermal and mechanical processes involved to produce lenses by the hot embossing method or photonic crystal fibers drawing are problematic as they tend to crystallize and/or crack. All the measurement methods mentioned in this chapter were used during this PhD work to characterize the glasses as well as the optical elements produced. The remaining chapters of this thesis are fully attributed to the author's work for his thesis.

Chapter 3 - Heavy Metal Oxides Glasses (HMOG): this chapter focuses on the development of a new heavy metal oxide glass system with improved thermal stability and transmission in the mid-IR to produce cost effective lenses by the hot embossing method. Indeed, thermal properties are critical to produce optical elements implying multiple heat treatments such as optical fibers or lenses [1].

We have shown that it was possible to develop glasses with transmission in the mid-IR up to 5 µm with a high thermal stability allowing multiple thermal processes involved in lens production. Due to the prospect of applications of tellurites based optical elements in the mid-IR and their extended transmission up to 5.5 µm as well as their nonlinear refractive index being 100 times larger than pure silica, I have also explored the possibility to synthetize purified tellurites glasses with a low water content to produce optical fibers. For this reason, I investigated various ways to dehydrate the materials produced in a controlled atmosphere glove box and used solid-state fluorides compounds to produce optical fibers by the stack and draw method. I fully contributed to this original work and fully assumed the synthesis of the newly developed glass system as well as its characterization. I contributed to the production of lenses by the hot embossing method and to their measurements in collaboration with Dr. Kujawak.

Chapter 4 - Chalcogenides glasses for the development of nanostructured core graded index fibers and micro-lenses by the stack and draw technique: this chapter investigates the possibility to develop graded index fibers by the stack and draw method with chalcogenide glasses, despites the multi-thermal processes involved. Chalcogenide fibers, due to their inherent crystallization tendency, were never produced by the stack and draw method. For the first time, the possibility to use highly stable chalcogenide glasses to produce mid-IR optical fibers by this method was shown. As a proof of concept, the possibility to produce chalcogenides based nanostructured micro-lenses derived from the stack and draw method was also investigated. I fully contributed to the fabrication of fiber optic preforms by the stack and draw method as well as the fiber drawing. I also took part into all the measurements of the preform and fibers as well as the production of the microlenses. Glass synthesis was done at the University of Rennes 1 in the Glass and Ceramic group by Dr. Meneghetti [3].

Chapter 5 - Supercontinuum generation in nanostructrured core all-solid fibers: this chapter investigates the possibility to generate a supercontinuum in a nanostructured core all solid fibers. Indeed, the nanostructuration of the core by the stack and draw method allows to tailor the dispersion profile easily, enabling flat dispersion over a wide range of wavelengths. For this purpose, two types of materials were compared: first, silica based nanostructured fiber composed of 2106 rods for a final core diameter of 7.15 µm [2] using nanosecond pulses and in a second time chalcogenide nanostructured fibers with a diameter ranging from 5.5 to 10 µm, tapering initial 10 µm optical fiber fabricated [3], pumped with femtosecond pulses. For the first time, chalcogenide nanostructured core gradient index fibers were developed by the stack and draw method. This opens a brand-new way to produce optical fibers for applications in the mid-IR up to 10 µm. We have shown that we can achieve a ZDW around 4 µm designing the dispersion profile of the fiber, even for chalcogenide fibers despite the ZDW typically located after 6 µm, which usually makes the pumping impossible with commercially available lasers. We try to solve this problem by the nanostructuration of the core in order to decrease the ZDW to commercially available wavelength around 4 µm. I was not involved in the fabrication of the silica based nanostructured fiber but was fully involved in the measurements of SCG at LEUKOS under the supervision of Pr. G. Huss. I contributed to the production of chalcogenides fibers as mentioned in Chapter 4 and collaborated with Dr. Petersen from DTU Photonic team to measure the generation of supercontinuum. I also was fully involved in the article writing published in 2021 in collaboration with Dr. Meneghetti [3]. I was not involved in the simulation of the various structures used to produce silica and chalcogenides fibers.

Publications in peer-reviewed journals related to the thesis

[1] **X. Forestier**, J. Cimek, I. Kujawa, R. Kasztelanic, D. Pysz, K. Orlinski, R. Stepien, R. Buczynski, *"Study of SiO_2 -PbO-CdO-Ga_2O_3 glass system for mid-infrared optical elements"*, Journal of Non-Crystalline Solids (2018).

[2] **X. Forestier**, T. Karpate, G. Huss, V. Tombelaine, G. Stepniewski, A. Anuszkiewicz, R. Kasztelanic, A. Filipkowski, D. Pysz, M. Klimczak, R. Buczynski, *"Supercontinuum generation in nanostructured core gradient index fibers"*, Applied Nanoscience, 10, 1997 (2020).

[3] M. Meneghetti, **X. Forestier**, C. R. Petersen, R. Kasztelanic, M. Klimczak, O. Bang, R. Buczyński and J. Troles, *"Graded Index Chalcogenide Fibers with Nanostructured Core",* Advanced Photonics Res., 2: 2000091 (2021).

Publications in peer-reviewed journals unrelated to the thesis

[4] M. Klimczak, D. Michalik, G. Stepniewski, T. Karpate, **X Forestier**, J. Cimek, R. Kasztelanic , D. Pysz, R. Stepien, R. Buczynski, *"Coherent supercontinuum generation in tellurite glass regular lattice photonic crystal fibers"*, Journal of the Optical Society of America B - special edition "Supercontinuum Generation" (2019)

[5] J. Cimek, **X. Forestier**, R. Stepien, M. Klimczak, R. Buczynski, *"Synthesis conditions of ZBLAN glass for mid-infrared optical components",* Photonics Letters of Poland, Vol 10, No1, 8-10 (2018).

Conference presentation

Conference IOS2020 - **X. Forestier**, M. Klimczak, R. Buczynski, *"Purification of tellurite glasses for mid-infrared applications"*, IOS2020 - The 15th Jubilee Conference. INTEGRATED OPTICS - SENSORS, SENSING STRUCTURES and METHODS (2020).

Workshops

- "SUPUVIR Summer School - Supercontinuum Broadband Light Sources for UV and IR applications" was held at the research institute FEMTO-ST (CNRS) in Besancon, France on 18-22 September 2017 (Author did a presentation about self-healing glasses and chalcogenides glasses for thermoelectricity).
- "SUPUVIR Photonics Symposium in Finland - A Symposium on Future Prospects for Photonics on Mid-Infrared Light Sources and Applications" was held at Tampere University of Technology (TUT), Finland, on 10-16 December 2017. (Heavy Metal Oxide glasses with silicates for the production of optical components).
- "SUPUVIR Workshop on Photonic Crystal Fiber Technology for Ultrafast Optics Applications" was held at the Institute of Electronic Materials Technology (ITME) in Warsaw, Poland, on 9-13 April 2018. (Author helped to organize part of the workshop and taught glass technology to the attendees such as the synthesis of a glass and their properties as well as Michelson interferometry technique for the measurement of bulk glasses).
- "SUPUVIR Microscopy and Sensing Workshop - Cambridge University - Supercontinuum in Microscopy and Biological Imaging Applications" was held by the University of Cambridge, UK, in November 2018.
- "PhD summer school in technical science entrepreneurship" was held by DTU Fotonik, Copenhagen, Denmark, on 11-18 August 2019.

Chapter 1: The vitreous state

The first trace of man-made glasses goes back to Mesopotamia and ancient Egypt empire 5000 and 3000 years ago respectively [1-2] while being naturally produced, notably with volcanic activity producing obsidian glasses. This natural glass, mostly made of silica, has many impurities and is unusable for everyday applications, besides being an art piece [3]. Since then, this unique amorphous state of matter was produced by humanity, leading to many applications from housing [4], to decoration, light sources [5-6], telecommunication [7], laser or various optical system, allowing us to explore the confinement of our universe and biological systems [8] to name a few. It is also commonly used for their mechanical properties notably for the car industry, as well as for the military such as bullet-proof panes. Since the development of glass science and the rise of companies such as Corning and Schott, many families of glass have been discovered. Four main families of inorganic glass have been discovered, oxides, fluorides, chalcogenides and more recently metallic glasses.

In this chapter, we will present the glassy state and its various properties, and we will briefly present the various glass families. We will also overview the various types of optical fibers and will summarize their specificities.

1. Glass

1.1 Definition

Various definitions of the vitreous states exist. A glass can be defined as a non-crystalline solid which exhibits the glass transition phenomenon [9]. The definition by Edgar D. Zanotto and John C. Mauro [10] is a more elaborated and complete version of Zarzycki's definition: "A glass is a non-equilibrium, non-crystalline condensed state of matter that exhibits a glass transition. The structure of glasses is similar to that of their parent super-cooled liquids (SCL), and they spontaneously relax toward the SCL state". Simplified, we can state that a glass is an amorphous material presenting the phenomenon of glass transition. In the contrary of crystals, which exhibit a short-range order, amorphous material such as glasses present no short-range order. Mid-range order structure can be observed in some glasses such as chalcogenides but are difficult to understand [11]. The glass network formation is yet to be understood completely, particularly for multicomponent glasses.

1.2 Important properties of the glassy state

1.2.1 Glass transition

The glass transition temperature (noted T_g) is defined as the transition from the supercooled liquid state to the amorphous state, characterized by a continuous and quasi linear evolution of the enthalpy H (or the volume V) [12]. The volume or enthalpy evolves as a function of the temperature as shown on (Figure 1). If the cooling rate of the liquid is high enough, the liquid goes to a supercooled liquid state without any

crystallization to finally reach an amorphous state. For higher cooling rate, the volume (or enthalpy) gets closer to the crystalline volume, meaning that the T_g is decreasing.

Glass transition temperature is characterized by a viscosity of $10^{13.4}$ Pa.s or $10^{12.4}$ Poise. At that viscosity, the time required for the equilibrium to be reached by the system is much higher than the relaxation time imposed by the cooling rate. This leads to an amorphous structure related to the molten state at which the atomic rearrangement process has been frozen, avoiding crystallization (short range order). Glasses are out of equilibrium (metastable) amorphous state of matter which exhibit the glass transition temperature T_g.

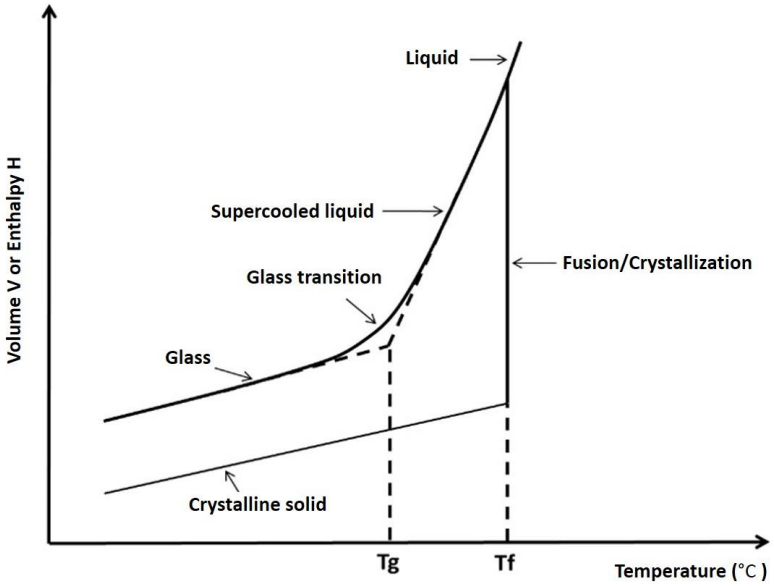

Figure 1: Evolution of the volume or enthalpy as a function of the temperature of a cooled melt [12].

1.2.2 Viscosity

Viscosity can be defined as the resistance opposed by a material to uniform flow. For a Newtonian liquid, viscosity in only function of the temperature and of the pressure. Viscous behavior of glasses can be described by the dynamic viscosity defined as the proportional constant between shearing force per surface unit (F/A) and gradient of the flow rate, also called shear rate dv/dx.

$$\frac{F}{A} = \eta \frac{dv}{dx}$$

For strong glasses, the viscosity follows Arrhenius law such as:

$$\eta(T) = \eta_0 . \exp\left(\frac{\Delta E_a}{k_b T}\right) \quad \text{(Poise or Pa.s)}$$

Viscosity of fragile glasses strongly depends on temperature and does not follow an Arrhenius law anymore. It can be described by Vogel-Fulcher-Taman model (VFT) [13]:

$$\log_{10} \eta(T, x) = \log_{10} \eta_\infty(x) + \frac{A_{(x)}}{T - T_0(x)}$$

where T is temperature, x is composition, and the three VFT parameters (η_∞, A, and T_0) are obtained by fitting the equation to experimentally measured viscosity data.

Angel proposed to classify glasses by their kinetic fragility index m [14] characterizing the slope of the variation of the viscosity as a function of the temperature (Figure 2) such as:

$$m = \left(\frac{d \log_{10} \eta}{d\left(\frac{T_g}{T}\right)}\right)_{T=T_g}$$

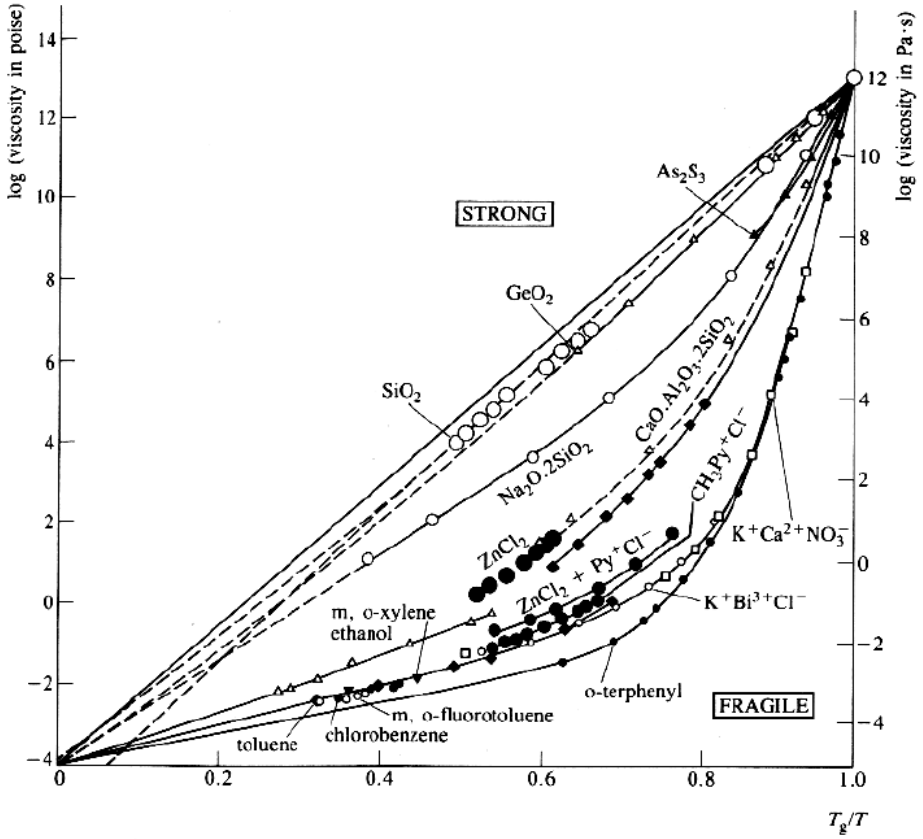

Figure 2. Logarithmic viscosities η of the melt as a function of the reduced temperature T_g/T showing the difference between strong glasses and fragile glasses according to Angell [14].

The viscosity of a soda lime silicate glass is a function of temperature (Figure 3). The various working temperatures are shown, the points annotated on the graph define various working ranges for a fixed temperature and viscosity of the glass, such as the Littleton temperature, temperature at which the glass deforms under its own weight. The viscosity of a glass is directly linked to the nature of the bonds forming the glass network and the component constituting it.

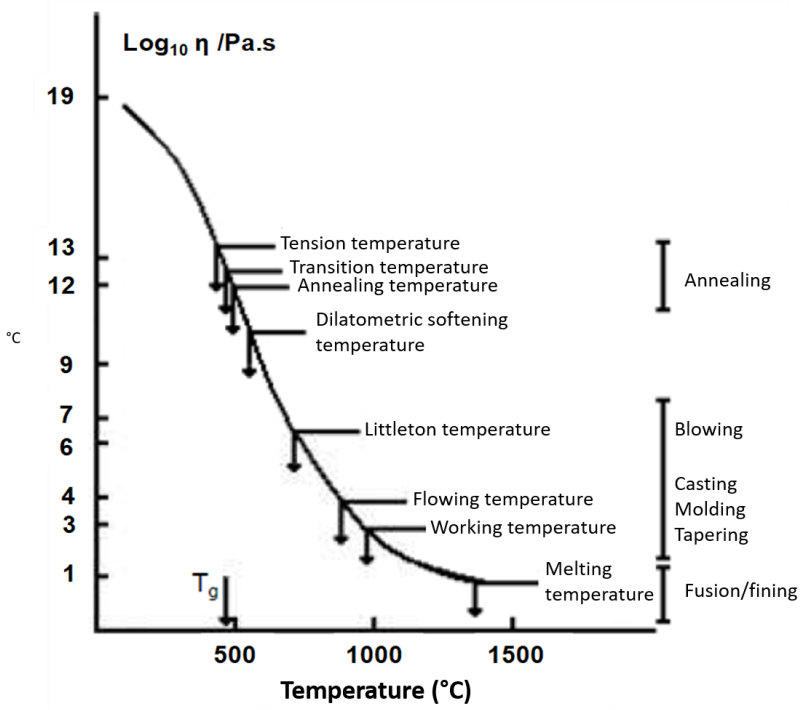

Figure 3. Viscosity logarithm of a Soda-Lime Silicate (SLS) glass as a function of the temperature [9].

1.2.3 Refractive index

We also evaluate an optical glass with its refractive index and its dispersion as a function of the wavelength. The refractive index n is characterized by n=c/v with c the speed of light in vacuum, v the speed of light into the medium. It strongly depends on the glass composition and the wavelength of the refracted light λ. The refractive index is a result of the sum of the polarizability of the ions and their bonds into the glass network. Globally, we see that the larger the ions, the more polarized are the electrons around the nucleus. We can classify the ions by their polarizability such as, for oxides glasses, $Bi^{+3}>Te^{4+}> Sb^{3+}>Zn^{+2}>Al^{3+}$ and for chalcogenides glasses $Te^{2-}>S^{2-}>O^{2-}>F^{-}$ [15]

In the case of low non-linear material or low intensity pulses, the macroscopic polarization can be considered as proportional to the electric field E associated to the incident wave, the excitation keeping a harmonic regime. The linear relation between the polarization and the field can thus be simplified, neglecting the anharmonic contribution such as:

$$P = \varepsilon_0 \chi^{(1)} E$$

with ε_0 the dielectric permittivity of the vacuum, P the polarization, $\chi^{(1)}$ the linear dielectric susceptibility.

In the harmonic regime, various frequencies do not interact with each other which leaves the polarization unchanged (Figure 4).

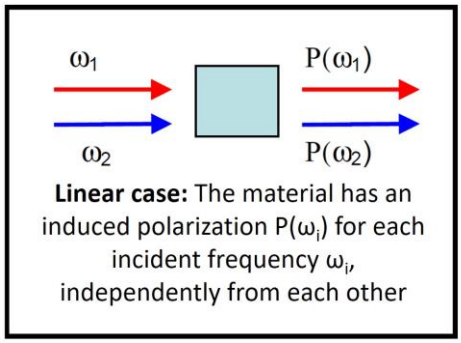

Figure 4. Linear case of two different frequencies travelling through a glass.

We can express the linear index of refraction n_0 with the first order susceptibility $\chi^{(1)}$ such as:

$$n_0^2 = 1 + \chi^{(1)}$$

This refractive index dispersion can also be interpreted with the Abbe number V. It can be calculated as a function of the refractive index at various wavelengths corresponding to the spectral rays of certain elements. For fluorides and oxides glasses, V is expressed such as:

$$V = \frac{n_D - 1}{n_F - n_C}$$

with n_D the refractive index of the sodium D-line (λ=589.2 nm), n_F the refractive index of the hydrogen F-line (λ=486.1 nm), and n_C the refractive index of the hydrogen C line (λ=656.3 nm).

Figure 5 shows the evolution of the Abbe number V as a function of the refractive index for the three main families of glasses mentioned earlier. V decreases with the atomic size of the components constituting the glass, so does the polarizability. As the polarizability decreases, the refractive index decreases as well.

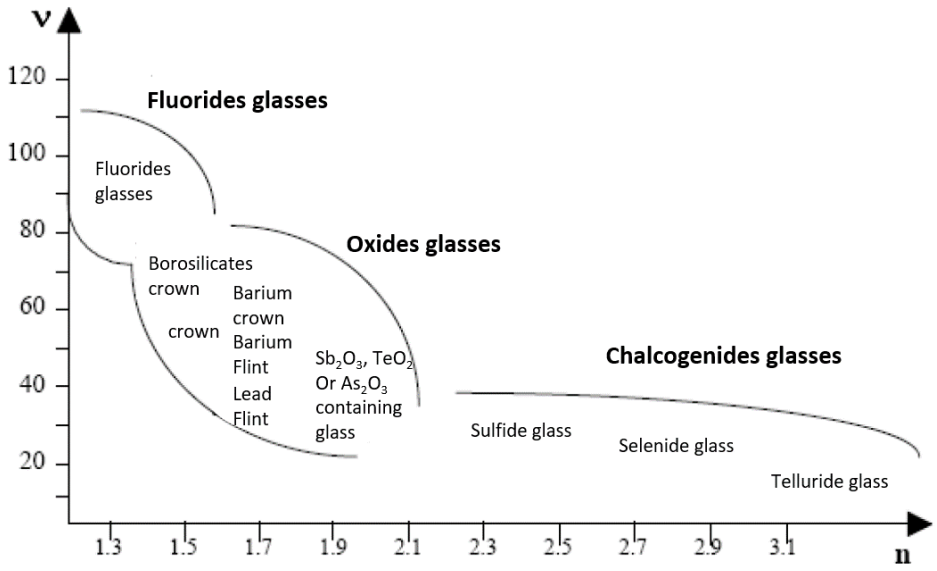

Figure 5. Evolution of the Abbe number as a function of the refractive index for various types of glasses.

1.2.4 Transmission window

As mentioned previously, glassy materials are divided in families depending on their compositions. This will intrinsically change their physico-chemical properties as well as their mechanical properties. The main three families of optical glasses are oxides, halides, and chalcogenides glasses. The transmission spectra of the three families are drastically different due to the different nature of the components making the glass network (Figure 6). Oxide glasses are the most produced glass family at an industrial scale. Indeed, it regroups silicates, soda-lime silicate, borate glasses as well as phosphates and heavy metal oxides. The composition of the silicates determines their transmission, generally from near UV up to 4-5 µm. Halide glasses are also transparent in visible but have an extended transmission up to 8 µm. The third family, chalcogenides (sulfides, selenides, and tellurides), have an outstanding transmission up to 24 µm for tellurides [16].

The transmission range of glasses is limited by two intrinsic phenomena of the materials: (i) the electronic absorption limiting at shorter wavelength and (ii) the multi-phonon absorption limiting the transmission at longer wavelength. Between those two, the transmission will also be limited by scattering and reflection as explained further.

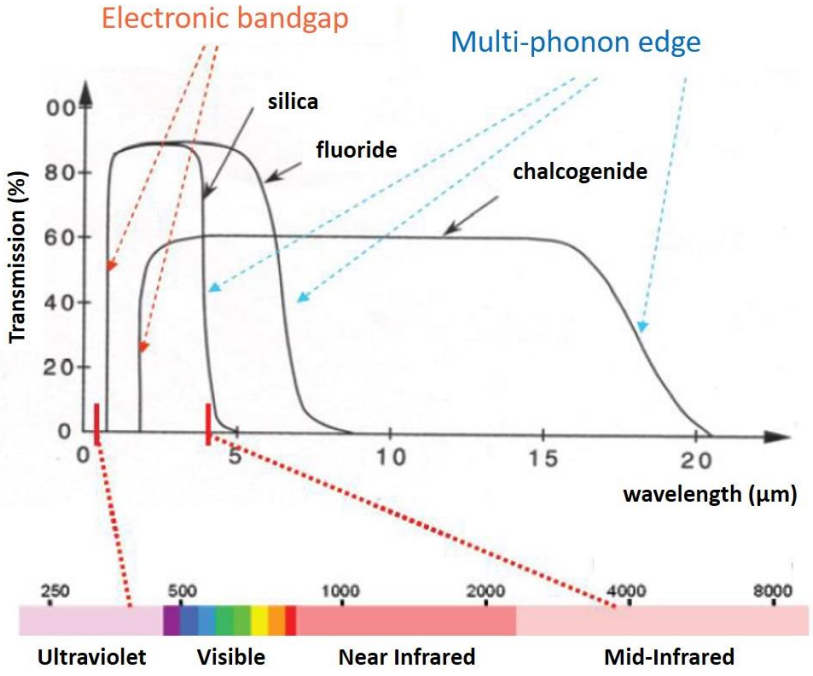

Figure 6. Transmission spectra of the three main families of glasses, limited by their electronic bandgap and their multi-phonon edges [16].

Glasses in Figure 6 are respectively quartz silica, fluoride glasses ZBLAN (53 ZrF_4–20 BaF_2–4LaF_3–3AlF_3–20 NaF), and a chalcogenide glasses with the composition ($Te_2Se_3As_4$-I) [12]

1.2.4.1 Electronic absorption (Urbach Tail)

The bandgap of the material is the difference of the energy between the conduction band and the valence band. The incident photons with an energy superior to or equal to this bandgap will be absorbed by the material due to electronic transitions. This absorption will limit the transmission at lower wavelength. We can calculate the bandgap energy such as:

$$E_g = \frac{hc}{\lambda_g} = \frac{1.24}{\lambda_g}$$

with E_g the bandgap (eV), h the Planck constant (6,58211899.10-16 eV.s), c the speed of light and λ_g the wavelength (µm).

The linear coefficient of absorption α of a glass can be calculated using Beer-Lambert law:

$$I = I_0 e^{-\alpha x} \quad or \quad \alpha = \frac{1}{x}\ln(\frac{I_0}{I})$$

with α the linear coefficient of absorption (cm^{-1}), I the transmitted intensity through the glass at a certain wavelength, I_0 the incident intensity and x the thickness of the sample.

1.2.4.2. Multiphonon absorption

Multiphonon absorption corresponds to the transparency limit of glasses in the infrared wavelengths. This multiphonon edge is due to the vibration of the glass network. This phenomenon arises from the interaction between electromagnetic waves and the chemical bonds constituting the glass, as well as its associated harmonics. The incident photon energy depends on the Planck constant and the frequency of the electromagnetic wave. We can schematize it as an oscillator simplified to two atoms with masses m_1 and m_2 respectively, the energy of the photon depending on the reduced mass µ and the force constant k of the bonds constituting the network such as:

$$E = h\nu \quad \text{with } \nu = \frac{1}{2\pi}\sqrt{\frac{k}{\mu}} \quad \text{and} \quad \frac{1}{\mu} = \frac{1}{m_1} + \frac{1}{m_2}$$

Therefore, a material transparency window will be shifted to longer wavelengths for composition with low k bonds force constant and heavy atoms, as previously shown on Figure 7. The multiphonon edge is situated at 5 µm for silicates, 8 µm for fluorides, 18 µm for selenides, and up to 24 µm for tellurides.

1.2.4.3. Reflection losses (Fresnel losses)

The percentage of the transmission spectra transmitted depends on the nature of the materials and the final refractive index resulting from the polarizability of the atoms constituting the glass network and its geometry. The reflection losses are linked to the different interfaces encountered by the incident electromagnetic wave. For a wave coming perpendicularly to the interface glass/air, the reflection can be estimated as follow:

$$R = \frac{(n-1)^2}{(n+1)^2}$$

As a first approximation, the transmission can be expressed in its simplified form such as:

$$T = 1 - R$$

If we consider a typical bulk glass and consider that the glass delimited by air/glass and glass/air interfaces is not absorbing, the transmitted intensity is given by:

$$I_t = \frac{(1-R)}{(1+R)}$$

The maximum transmission intensity varies depending on the glass family as shown in Figure 6. For low refractive index glass such as silicates (n=1.5), the transmission will be around 92%, while chalcogenides such as tellurides (n>3) will have a transmission around 55%.

1.3 Structural conditions of glass formation and composition

With time, various theories have been formulated to explain the formation of glasses. Indeed, the peculiar nature of amorphous inorganic material and their formation process is yet to be understood completely. The various mid-range network structures obtained through various glass families have shown to be difficult to understand. Typical silica glass structure compared to its crystalline form is shown on Figure 7.

1.3.1 Zachariasen criterium

In 1932, Zachariasen issued an ensemble of four structural conditions for a "M_xO_y" oxide to form a glass [17]:

- (1) No oxygen atom must be bonded to two cations M.
- (2) Coordinence polyhedrons can have a common apex but no edges and plan in common.
- (3) The number of oxygens bonded to the cation must be small (3 or 4).
- (4) The formation of a 3D network implies that at least three apexes must be linked to surroundings polyhedrons.

From these rules it is easy to see that MO and M_2O cannot form glasses. In fact, it has been shown later, that mostly rule 1 and 2 are essentials. Indeed, if the polyhedron is a tetrahedra, it can share an edge and two opposites apexes with surrounding neighbors. On the contrary, R_2O_3, RO_2, and R_2O_5 can easily form glasses. It is easily confirmed by the glass formation ability of B_2O_3, As_2O_3, SiO_2, GeO_2, V_2O_5 and P_2O_5.

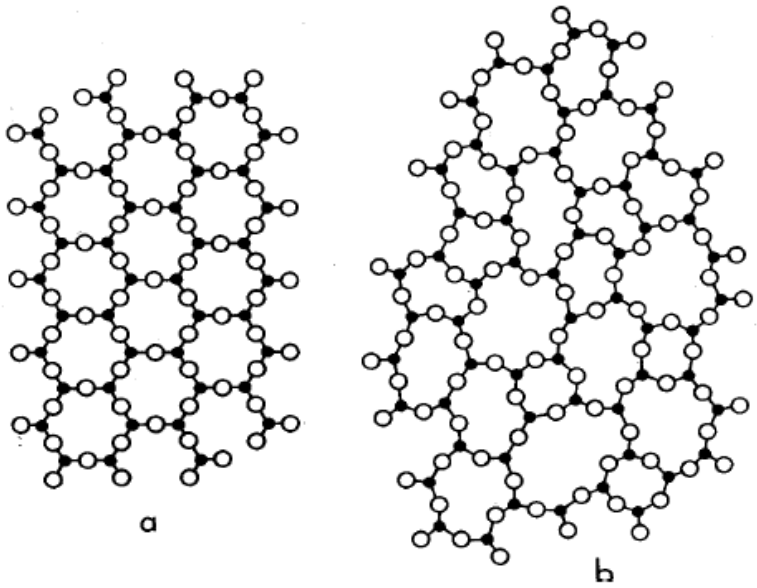

Figure 7 Bi-dimensional structure representation of (a) a crystalline silica network and (b) an amorphous silica network according to Zachariasen (●: Silicon, ○: Oxygen) [12].

1.3.2 Goldschmidt criterium (ionic radius)

According to Goldschmidt theory of glass formation in 1926 [15], known as one of the fathers of modern crystal chemistry stated that for simple oxides of formula M_nO_n (M=cation, O=Oxygen), glass formation is only possible when the ratio of atomic radii of the anion R_a over the radius of the cation R_g falls between 0.2 to 0.4, glass formation is possible such as:

$$R_g = \frac{R_c}{R_a}$$

This is to take with precaution, indeed for typical glasses we observe that:

-If R_g is high (superior to 0.40), the vitrification is difficult.

- If R_g is low (inferior to 0.40), the vitrification is easy (Table 1).

Table 1. Radius ratios for typical glass forming compounds [18].

Compound	Radius ratios (r_c:r_a)
SiO_2	r_{Si}:r_O = 0.39 Å:1.4 Å ≅ 0.28
B_2O_3	r_B:r_O = 0.20 Å:1.4 Å ≅ 0.15
P_2O_5	r_P:r_O = 0.34 Å:1.4 Å ≅ 0.25
GeO_2	r_{Ge}:r_O = 0.44 Å:1.4 Å ≅ 0.31
BeF_2	r_{Be}:r_F = 0.34 Å:1.36 Å ≅ 0.25

1.3.3 Dietzel criterium (Coulomb force)

Dietzel proposed in 1942 to classify the glass forming ability of cations with oxygen using the Coulomb law of attraction with oxygen ion when the distance between M-O is equal to the sum of ionic radii [19]. He quantifies it as the field intensity A such as:

$$A = \frac{Z_c}{(r_c + r_0)^2}$$

With Z_c the valence of the cation, r_c the ionic radius of the cation and r_0 the ionic radius of oxygen.

We can see that cations are network formers for A>1, network modifiers for A<0.35, and intermediates cations are in between, 0.35 < A < 1 (Table 2).

If this model is accurate for most oxides, it has limits. For example, PbO is experimentally known as an intermediate, alternately acting as a modifier in silicates, for concentration below 40% and starting to act as a network former for concentration above 40% in silicates.

Table 2. Field intensity of various cations

Cations	Valence Z_c	r_c (Å)	A (Å^{-2})	Type
P	5	0.31	1.71	Formers
V	5	0.49	1.4	
Si	4	0.4	1.235	
B	3	0.25	1.102	
Sb	5	0.74	1.092	
Ge	4	0.53	1.074	
Ti	4	0.74	0.873	Intermediates
Al	3	0.53	0.805	
Zr	4	0.86	0.783	
Be	2	0.41	0.61	
Mg	2	0.86	0.392	
Zn	2	0.88	0.385	
Ca	2	1.14	0.31	Modifiers
Pb	2	1.33	0.268	
Li	1	0.9	0.189	
Na	1	1.16	0.153	
K	1	1.52	0.117	

1.3.4 Sun criterium (bond strength)

Sun classified oxides by their single-bond strength to oxygen [20]. He established three types of oxides:

- Network formers forming single bond strength $E_{M\text{-}O}$ > 80 kcal/mol, forming a rigid network leading to high viscosity.

- Network modifiers forming weak bond to oxygen with a single-bond strength $E_{M-O} < 60$ kcal/mol, disrupting the glass network leading to a less rigid network and thus a lower viscosity.
- Intermediates, which cannot form a glass by themselves but can easily form a glass if combined with other oxides (tellurites for example). Their single-bond strength is situated in between such as 80 kcal/mol > E_{M-O} > 60 kcal/mol.

The basic idea behind this model is that, when a melt is quenched to form a glass, the stronger the M-O bonds, the more difficult are the structural rearrangements necessary for crystallization and, the easier is the glass formation (Table 3).

1.4 Classification of oxides

1.4.1 Glass network former oxides

Glass formers are oxides that can readily form glass by themselves. The most common formers are SiO_2, GeO_2, P_2O_5, As_2O_5, V_2O_5. The various theories mentioned earlier predict pretty well which oxides are network formers in contrary of intermediates and network modifiers where practically, we see some differences with the theories mentioned previously, depending on the composition and the number of components. Some other oxides could easily be attributed to network formers, but the high cooling rate necessary to readily form pure glasses makes it impossible to produce them in bulk. TeO_2 is one of the best examples. Few percent of oxides are necessary to form a tellurites glass under normal condition in a furnace by the classic melt-quenching method described in Chapter 4, while it can only form a pure TeO_2 glass with a high cooling rate such as on metallic plate or using flash DSCs with a high cooling rate. [21].

1.4.2 Network modifier oxides

Alkaline creates non bridging oxygen, opening the glass network by discontinuing the silica network as depicted in Figure 8 and thus decreasing the viscosity. Alkaline earth also plays the roles of modifiers, creating two non-bridging oxygen per alkaline earth ion. The decrease of viscosity is more moderate than alkalis since in a sense both NBOs created are still bonded by the divalent alkaline earth ions, thus creating stronger bonds.

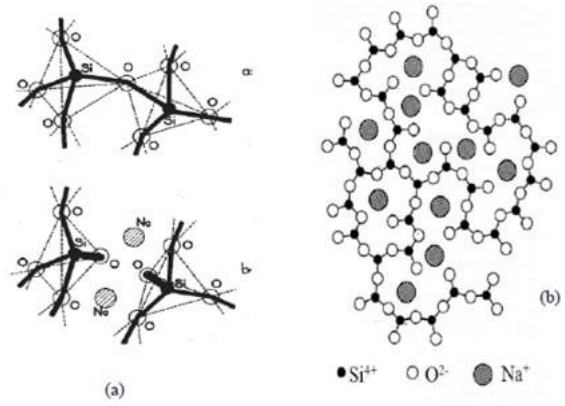

Figure 8 (a) Si-O-Si bond disruption by sodium cation, (b) Silica glass network modified by sodium ion. [12]

1.4.3 Intermediate oxides

Some oxides such as PbO, ZnO, TeO_2, Al_2O_3 cannot form a glass by themselves. However, depending on the glass composition, intermediates can either play the role of modifiers or glass formers depending on the components they are associated with; PbO and TeO_2 are some of the best examples.

Table 3. M-O bond strength of the cations for some glass formers, modifiers, and intermediates according to Sun [20]

M in M-O_x	Valence	Energy of dissociation E_d (kcal/mol)	Coordination number Z	Bond strength (kcal/mol) $E_{M-O} = E_d/Z$
Glass formers				
Si	4	424	4	106
B	3	356	4	89
P	5	442	4	111
V	5	449	4	112
As	5	349	4	87
Sb	5	339	4	85
Zr	4	485	6	81
Intermediates				
Ti	4	435	6	73
Al	3	317-402	6	53-67
Th	4	516	8	65
Be	2	250	4	63
Zr	4	485	8	61
Modifiers				
Sc	3	362	6	60
La	3	406	7	58
Y	3	399	8	50
Sn	4	278	6	46
Ga	3	267	6	45
In	3	259	6	43
Th	4	516	12	43
Mg	2	222	6	37
Li	1	144	4	36
Zn	2	144	4	36
Ba	2	260	8	33
Ca	2	257	8	32
Sr	2	256	87	32
Na	1	120	6	20
K	1	115	9	13
Rb	1	115	10	12
Cs	1	114	12	10

2. Families of glasses

Besides metallic glasses and organic glasses (polymers), we can distinguish three main families of inorganic glasses: oxide glasses, halide glasses and chalcogenide glasses.

2.1 Oxides glasses

2.1.1 Silicates

The most common glass, silica glass, is made of pure silica and is also named quartz silica, the network is exclusively made of SiO_2. Tetrahedron connected to each other with various O-Si-O angles α as well as variations of the torsional angles O-Si as shown on Figure 9.

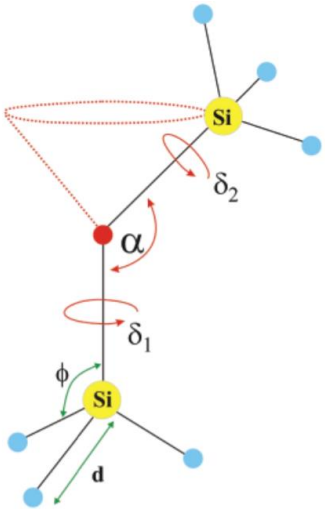

Figure 9. Network disorder occurs through variation in the inter-tetrahedral angle α and the two torsional angles δ_1 and δ_2. The tetrahedral angle φ and Si–O bond lengths remain unchanged.

The addition of oxides such as alkaline oxides, germanium oxide GeO_2 or lead oxide PbO have led to the development of a wide variety of glasses for various application from thermal resistant glass Pyrex [22] to mechanical glass such as Gorilla glass for phones [23] or optical Flint glasses for optic or GeO_2 doped silica fibers for telecommunication. The problem of silicate-based glasses for optic are their limited transmissions to 4 to 5 µm and their limited nonlinearity, as explained previously.

2.1.2 Heavy metal oxides glasses (HMOG)

Heavy metal oxides are glasses of strong interest for optic. Indeed, these glasses present a refractive index ranging from 1.8 to 2.2, a theoretical transmission up to 6 µm and a nonlinear refractive index up to 100 times silicas. Their acceptable mechanical properties as well as their decent chemical durability (compared to fluorides and chalcogenides) make them a good candidate for mid-IR applications such as the development of photonic crystal fiber or lenses [24]. The most used HMOG for mid-IR applications are tellurite glasses, due to the exceptional forming ability of TeO_2 when associated with other oxides. They

represent a good replacement to lead silicates glasses, thanks to their decreased toxicity and their slightly improved overall linear and non-linear optical properties. Their lower stability represents a challenge, especially compared to silica glasses. TeO_2 does not form a glass by itself in normal condition but associated with other oxides such as alkaline, zinc, lead or bismuth oxide, they easily form highly stable glasses, allowing to produce optical components [25].

Their transition temperature T_g is usually located between 260 and 330 degrees and their soft glasses nature make them particularly practical for the production of optical components.

Typically, tellurite glasses are based on TeO_4 double triangular bipyramids (tbp's) polyhedron resulting from one Te atom surrounded by four oxygen atoms, two oxygens being at equator position and the other two in axial position, TeO_3 bipyramids (bp's) _and TeO_{3+1} deformed double triangular pyramid units, forming the glass network [26]. Depending on the network modifiers used in the composition, the structure of tellurites can vary vastly compared to silica based HMOG with a much more opened network composed of the units presented in Figure 10, making them more prone to crystallization and mechanical failures. The main advantage of tellurites glasses is that they represent a nice trade-off between mechanical, chemical, and optical properties, making them particularly adapted to Mid-IR applications up to 6 µm.

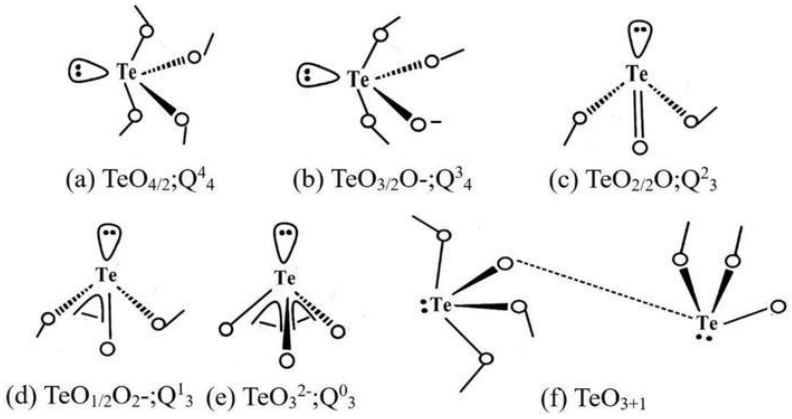

Figure 10 (a–e) Five basic structural units in alkali tellurite crystals. (f) Deformed bitriangular cone TeO_{3+1} [26].

2.1.3 Phosphates

Phosphate glasses are based on P_2O_5 oxide to form the glass network and are generally structured around Q^0, Q^1, Q^2 and Q^3 basic units (Figure 11a) crosslinked together as shown on Figure 12. Q_3 corresponds to PO_4 sub-unit with three bridging oxygen while Q_2, Q_1 and Q_0 respectively correspond to tetrahedrons with two, one and zero bridging oxygens as shown on Figure 11b.

Phosphate glasses have a relatively low T_g, low melting and softening temperatures, high electrical conductivity [27], large thermal expansion coefficients [28], biodegradable and a transmission window ranging from UV to near infrared [29]. These physico-chemical properties make phosphates glasses particularly interesting for high power lasers [30] and biomaterials [31-33]. However, they have a poor

chemical durability due to the hydrolysable nature of the P-O-P bond which is why phosphates are nowadays modified using other oxides such as Al_2O_3, Ga_2O_3, PbO, ZnO to increase the chemical durability by creating more covalent bonds [34].

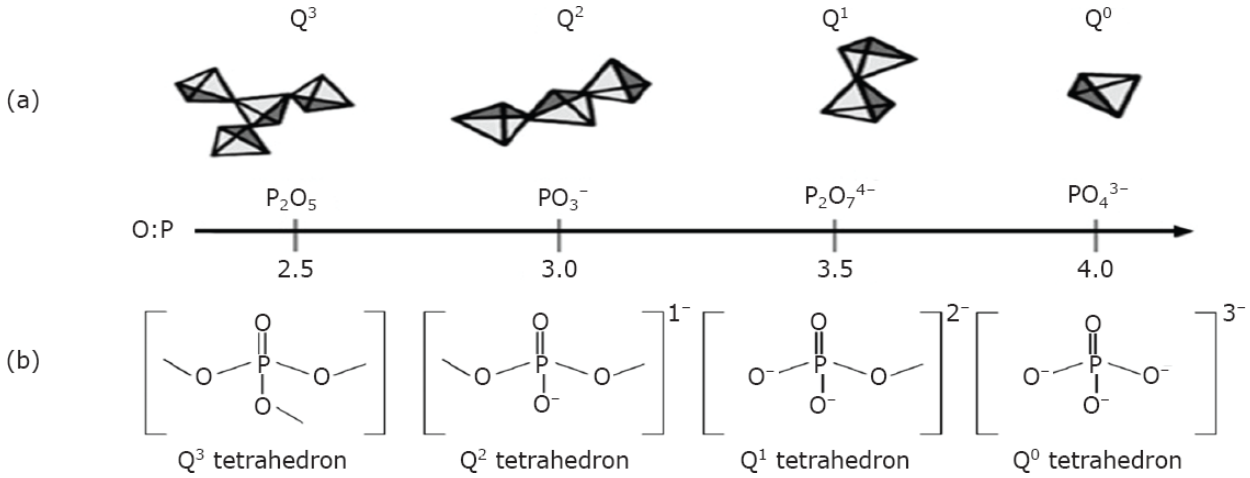

Figure 11 (a) Phosphate tetrahedral classifications used to define the structure of phosphate glasses (b) Q^n phosphate structural units forming the glass network [35].

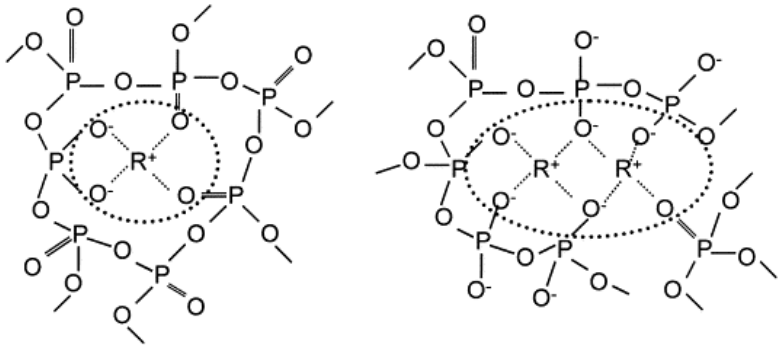

Figure 12. Typical phosphate glasses with Q^1, Q^2, Q^3 units forming the glass network with the modifier cation R^+ disrupting the network [36].

2.2 Halide glasses

The main halide glass sub-family is fluoride glass which can be divided into two categories: transition metal fluorides glasses (TMFG) and heavy metal fluoride glasses (HMFG).

2.2.1 Transition metal fluoride glasses (TMFG)

The first fluoride glasses were based on BeF_2, identified by W. M. Goldschmidt in 1927 [37], with similar structure to silica glasses, but their utility was limited considering their toxicity and their high hygroscopy. Their transition temperatures were mostly too low and their viscosity curves too deep to be usable.

In 1945, K. H. Sun [38] described new fluoride glasses based on aluminum fluoride, lead fluoride and alkaline earth such as NaF to reduce the chemical durability and toxicity. Their thermal stability was also improved.

2.2.2 Heavy metal fluoride glasses (HMFG)

This new type of glass was discovered by the Poulain brother in 1974 at the University of Rennes 1 in France, at the solid-state chemistry department, now named Glass and Ceramic department, while working on new fluoride complexes based on zirconium fluoride [39-40]. This led to a breakthrough in glass science and technology development such as optical fibers, supercontinuum sources and opened the prospect for ultra-low-loss optical fibers. Ultimately, they developed the famous ZBLAN glass (ZrF_4-BaF_2-LaF3-AlF_3-NaF, in mol%). The structure of halide glasses is vastly different than silicates, it is made of chain like structure with a strong ionic character as shown on Figure 13.

Heavy metal fluorides glasses, with their extremely broad transmission from ultraviolet to the mid-infrared, up to 8 µm, have a linear and nonlinear refractive index similar to silicates. Moreover, their high rare-earth solubility and their low attenuation allow fiber laser applications [41-42] and the generation of supercontinuum with ultrashort high-power pulses [43]. Their losses are theoretically around 0.01 dB/km at 2.55 µm (Figure 14) which represents a real breakthrough for telecommunication. Indeed, this extra low loss would allow repeaterless transoceanic telecommunications. Improvement in the synthesis process such as the purification and the synthesis conditions will be required to reach this theoretical limit. Indeed, ZBLAN glasses tend to crystallize due to various reasons such as the convection flow due to the heat treatment during the synthesis and the fiber drawing, and the gravity itself, causing inhomogeneities in the melt ultimately leading to the formation of microcrystals during fiber drawing [44]. NASA has proposed to make fluoride glasses synthesis in micro gravity condition in the International Space Station (ISS) during the 1990s to minimize the impact of gravity on the formation of crystals during fiber drawing. Since then, due to the increasing interest of what ZBLAN optical fibers could offer, companies such as 'Le Verre Fluore' are actively working to offer optical applications such as large band supercontinuum sources in collaboration with Selen Optics and LEUKOS [45].

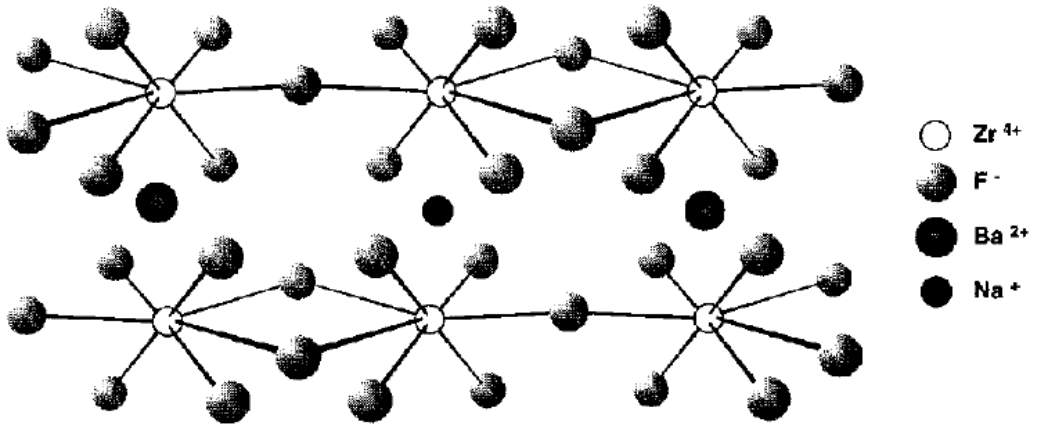

Figure 13. Chain-like skeleton in the structure of a ZBLAN6.6 glass (57.0 ZrF_4-28.1 BaF_2-3.3 LaF_3-5.0 AlF_3-6.6 NaF, in mol%) [46].

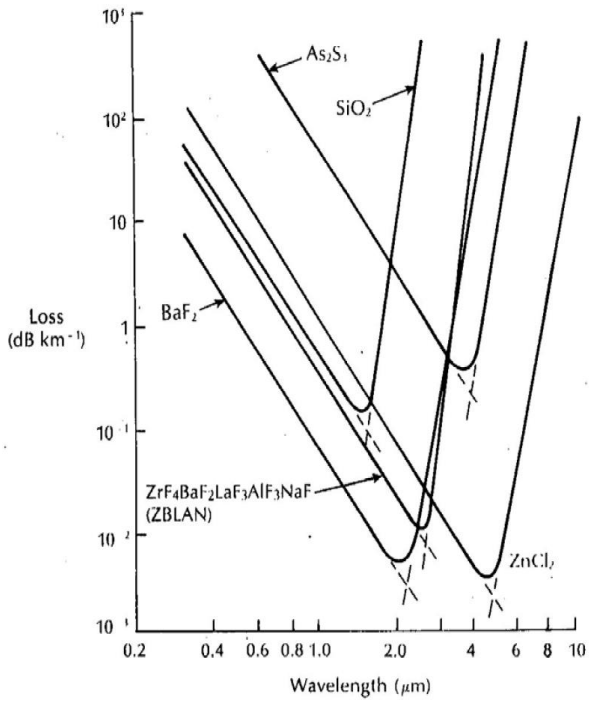

Figure 14. Theoretical and experimental losses of the three main families of glasses [47].

2.3 Chalcogenide glasses

Chalcogenide glasses are glasses which contain one or several chalcogen elements, S, Se or Te, associated with elements from group IV and V of the periodic table. Chalcogenide glasses offer a large transmission window in the infrared, high linear and non-linear refractive indices as well as a low phonon energy which makes them excellent host materials for amplifier and laser applications [48], despite their rather low rare earth solubility [49]. Their unique properties of high transmission window also make them appropriate for applications in IR optics (Fig. 15) such as thermal imaging [50], metrology [51], military defense systems, memory IT system or medicine [52].

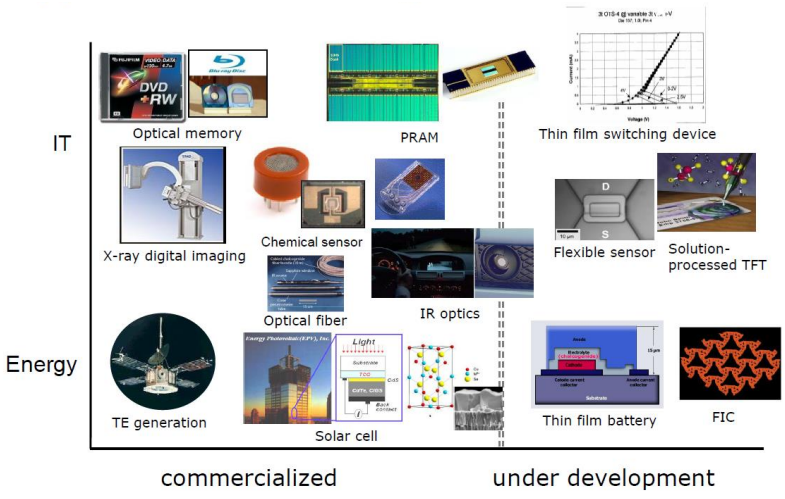

Figure 15 Various applications with chalcogenides glasses.

Sulfur and selenium-based glasses have a transparency up to 10 µm and 16 µm respectively [53]. Tellurium based glass, on the other hand, can exhibit a multiphonon cut-off wavelength up to over 24 µm (Figure 16) due to Te higher atomic weight [54]. However, due to the strong metallic character of tellurium, they have a tendency to crystallize during thermal processing. They also present low mechanical properties and are difficult and expensive to produce due to the additional purification processes of the components needed to attain a high purity. The synthesis method as well as the purification processes will extensively be explained in Chapter 4.

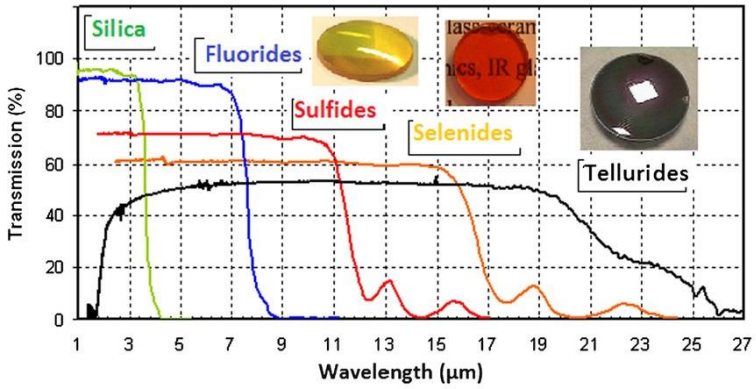

Figure 16 Window of transparency of S, Se, Te-based chalcogenide glasses. The presented glasses and spectras correspond to As_2S_3 for the sulfide, As_2Se_3 for the selenide and $Te_{20}As_{30}Se_{50}$ for the telluride glass. [55].

3. Fiber optics

3.1 Historic

Many scientific and industrial applications arose from the development of optical fiber in the last decades, in particular in telecommunication, enabling data transfers technology to the mass. Jean-Daniel Colladon first studied the propagation of sound through water, leading to his research on the propagation of light through water in 1841 [56-57]. Mostly used as decoration apparatus we can still find laminar water jet illuminated as art pieces (Figure 17).

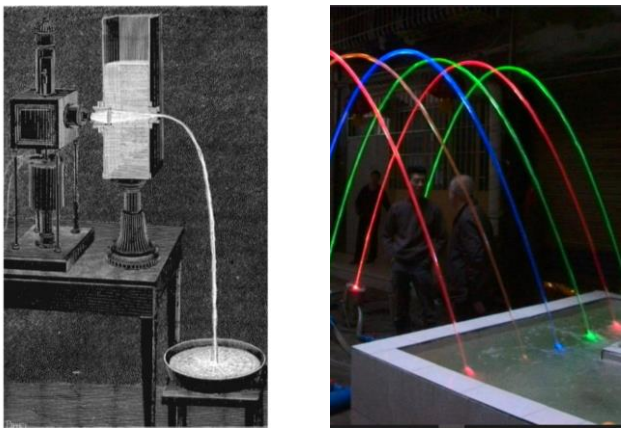

Figure 17 (a) Colladon's luminescent fountain (1841), (b) Laminar jet fountain with LED injection commercially available.

At the end of the nineteenth century, fiber optics started to find scientific applications. For example, Roth and Reuss used glass rods as a waveguide for medicine.

It is only in 1954 that the guiding of light properties of optical fibers were used with the invention of a flexible fiberscope by Van Heel et Hopkins, allowing the transmission of image through the optical fiber, despite the high losses, around 1000 dB/km [58]. The invention of the first laser in 1960 allowed the transmission of a signal over a large distance due to their inherent high power. In 1964, Charles Kao achieved the first fata transmission through an optical fiber [59].

In 1970, three researchers, Robert Maurer, Peter Schultz and Donald Keck, from the famous company Corning developed the first optical fiber with losses low enough to enable optical fiber telecommunication transmission (20 dB/km at 1550 nm) [60]. This fiber had a bandwidth 65000 superior to copper cable [61] leading to the vast superiority of silica based glassy optical fibers due to their rather low loss at the telecommunication wavelengths. In 1988, the losses attained 0.15 dB/km [62].

In 1996, Knight et al. from the optoelectronic group of the University of Bath fabricated the first photonic crystal fiber made of silica glass structuring the cladding with a periodic arrangement of air holes in order to manage the effective refractive index (Figure 18) [63]. This work opened the début of the development of photonic crystal fibers in the world using the various glasses families mentioned previously in this chapter.

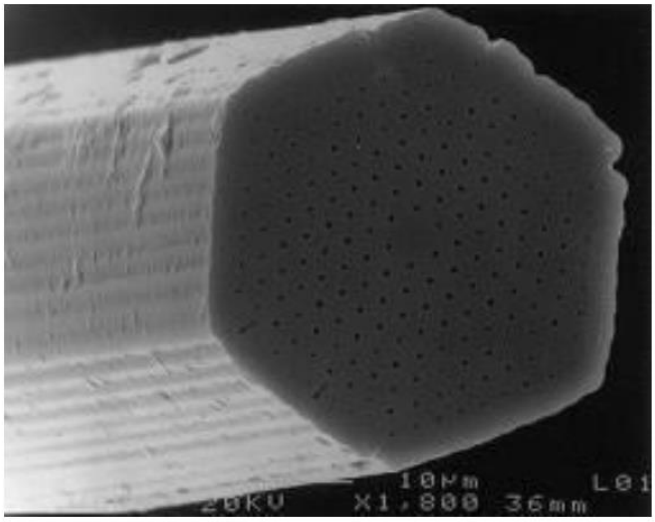

Figure 18. Scanning electron microscopy (SEM) of the first monomode silica PCF developed by J. C. Knight et al. in 1996 [63].

3.2 Propagation of light in conventional fiber optics

3.2.1 Total internal reflection

The propagation of an electromagnetic wave through a traditional optical fiber is based on the principle of total internal reflection (TIR). During the 17th century, the first mathematical explanation of the phenomenon was written by Snell (1621) and Descartes (1637).

According to Snell-Descartes law, when a beam of light goes through a lower index transparent material, the refracted beam angle > incident angle. This law is described by the equation:

$$n_1 . \sin\theta_1 = n_2 . \sin\theta_2$$

Where n_1 is the incident material refractive index, n_2 the refractive index of the refractive material, θ_1 the incident angle, θ_2 the refraction angle.

For a critical incident angle $\theta_i = \theta_c$, the refracted beam is perpendicular to the propagation axis z such as:

$$\sin\theta_c = \frac{n_2}{n_1}$$

When $\theta_i > \theta_c$, the beam is reflected instead of being refracted symmetrically to the normal, obeying TIR. In the case of light propagating into an optical fiber, part of the reflected beam energy is transmitted to the cladding as evanescent waves with its energy exponentially decreasing into the cladding.

If $\theta_i < \theta_c$, reflection occurs at the same time as refraction such as at normal angle, the coefficient of reflection R is given by:

$$R = \left(\frac{n_2 - n_1}{n_2 + n_1}\right)^2$$

The transmission coefficient can be calculated as T = 1- R if we neglect the absorption of the medium. The loss due to the reflection are called Fresnel losses, we can easily see that the higher the refractive index of the material, the higher the Fresnel losses are.

3.2.2 Structure of standard optical fiber

An optical fiber consists of a cylindrical waveguide in which light will be guided by TIR due to the different refractive index between the core and the cladding ($n_{cl} < n_{co}$). Fiber optics are generally coated with a protective layer to mechanically strengthen them due to their generally low mechanical properties.

A typical optical fiber is made of three different parts (Figure 19):

Core: TIR is the base principle of propagation into the core. Its refractive index n_{core}> to $n_{cladding}$ to satisfy Snell-Descartes law so the pulse is propagating along the optical fiber.

Cladding: To confine the pulses into the core, the refractive index of the cladding must be lower than the core's. For silica optical fibers, germanium is generally used to increase the refractive index of the core while boron and fluorides are used to reduce it.

Coating: Due to their brittle mechanical properties, optical fibers are generally coated with a polymer.

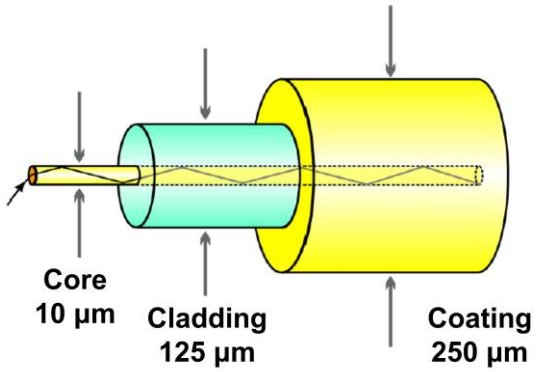

Figure 19. Typical structure of an optical fiber composed of a core, a cladding, and a protective coating.

3.2.3 Guiding mechanism in standard optical fibers

Depending on the incident angle, according to the total internal reflection principle, some rays, beyond a limit incident angle will not be guided. We can define the acceptance angle such as the angle at which the light is guided into the core by the total internal reflection as shown on Figure 20.

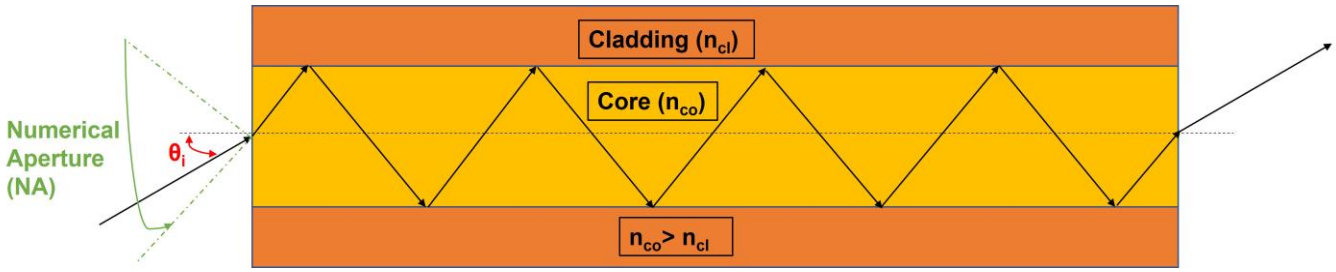

Figure 20. Propagation of the light according to TIR along an optical glass fiber with a core with refractive index n_{co} and n_{cl} for the cladding with $n_{co}>n_{cl}$.

We can define the limit of the sinus of the incident angle as the numerical aperture (NA), characteristic of optical fibers such as:

$$NA = \sin(\theta_i) = \sqrt{n_{co}^2 - n_{cl}^2}$$

with NA, the numerical aperture, θ_i the incident angle of the light, n_{co} the refractive index of the core and n_{cl} the refractive index of the cladding material.

We can calculate the number of modes in a step index fiber calculating the normalized frequency V such as:

$$V = \frac{2\pi a}{\lambda}\sqrt{n_{co}^2 - n_{cl}^2}$$

where V is the normalized frequency, a the radius of the core, λ the wavelength, n_{co} the refractive index of the core and n_{cl} the refractive index of the cladding.

If the normalized frequency V<2.405 at a certain wavelength, the optical fiber is monomode. The wavelength at which the fiber passes from monomode to multimode is called the cut off wavelength for V>2.405 (Figure 21). Therefore, we can define the lowest wavelength at which a given optical fiber is single mode, λ_c, called the cut-off wavelength V_C, such as:

$$\lambda_c = \frac{2\pi a}{V_c}\sqrt{n_{co}^2 - n_{cl}^2} \quad \text{with } V_c\text{=2.405 the cut-off V number}$$

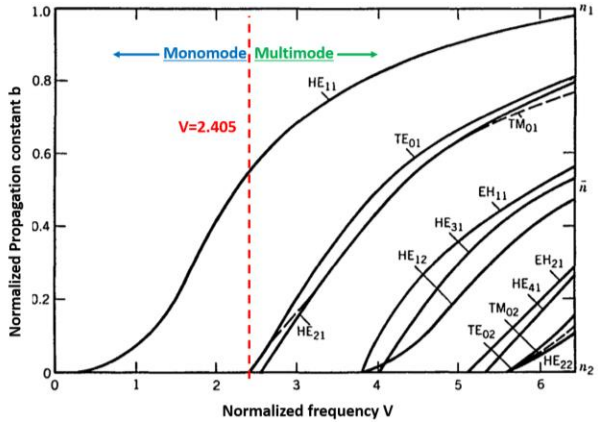

Figure 21. Normalized propagation constant b as a function of the normalized frequency V for few modes propagating in the optical fiber.

In the case of multimode optical fibers, the normalized frequency V gives information about the number of modes propagating through the fiber such as:

$$M = \frac{V^2}{2}$$

Where M is the number of modes and V the normalized frequency.

Three main types of optical fibers exist as shown on Figure 22, large core multimode step index fibers, small core step index monomode fibers and gradient index fibers generally produced by chemical vapor deposition (CVD)or ion exchange and more recently by the stack and draw method [64].

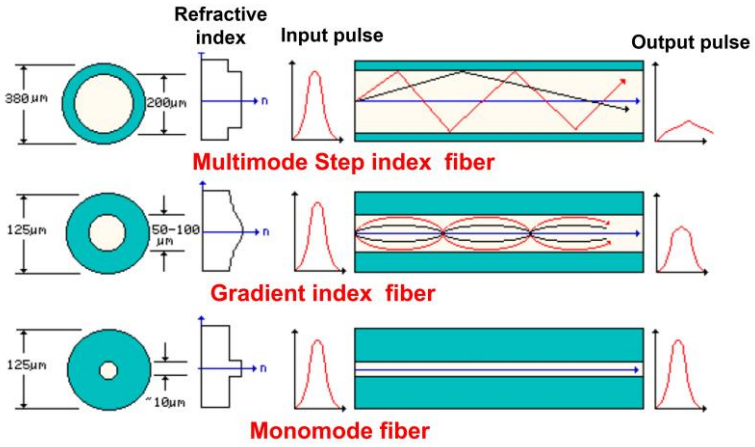

Figure 22. Representation of the propagation of a gaussian pulse through step index, gradient index and monomode fibers. The refractive index profile along the width of the optical fiber is also shown.

Graded index optical fibers were mostly developed for telecommunication to decrease the intermodal dispersion without affecting the numerical aperture NA, hence the signal energy. As explained in Chapter 4, the parabolic profile is due to a gradient refractive index through the core. Light has a sinusoidal trajectory, the lower refractive index wavelength having a longer optical path than lower refractive index. The cost of such fiber remains important which is why we assess this problem in this thesis developing gradient index fiber by the stack and draw method.

Small core step-index monomode optical fibers (r_{co} few microns) generally has a small core and a small refractive index difference Δn between the core and the cladding. Such fibers only allow the propagation of the fundamental mode (Figure 29). Unlike multimode fibers, these optical fibers intermodal dispersion is equal to zero, which explains their interest for long distance transmission.

3.3 Optical losses

3.3.1 Extrinsic absorption

Besides the intrinsic phenomena mentioned previously, extrinsic absorption also plays an important role in the transmission characteristics of the material. Indeed, impurities inserted into the glass network (e.g., H_2O, CO_2, 3d metals) lead to the apparition of bonds (e.g., -OH, H_2O, CO_2, S-H, Se-H), which is why the purification of the components is primordial to extend the transmission as close as the theoretical limits, as explained in depth in Chapter 4. In the case of chalcogenide glasses, 1 ppm of impurities can induce a loss of 1 to 10 dB/m depending on the chemical bonds involved [65]. Most common chemical bonds due to impurities can be found in Table 4 for chalcogenide glasses.

Table 4. Examples of bonds affecting the transmission of chalcogenides glasses [66-67].

Bonds	Wavelength (µm)
S-H	2.05/2.55/3.09/3.69/4.1
Se-H	2.3/3.45/3.55/4.3/4.5/15.9
H_2O	2.29/2.39/6.3/10.7
O-H	2.73/2.9
Ge-O	7.8/12.5/20
CO_2	4.26
Ge-H	4.92
As-O	8.9

3.3.2 Scattering

3.3.2.1 Elastic Scattering losses

3.3.2.1.1 Rayleigh *scattering*

Rayleigh scattering was discovered by the physicist John William Strutt, more famous under the name Lord Rayleigh in 1871 [68]. The fluctuation of the density of the amorphous material such as glasses at the

atomic level will cause the light to be scattered in all direction. This is the result of the micro-fluctuations of the glass refractive index giving rise to losses which can be expressed such as:

$$\alpha_{scat} = \frac{8\pi^3}{3\lambda^4} n^8 p^2 k T_f \beta$$

with n is the linear refractive index, p is the photo-elastic coefficient of the glass, k is the Boltzmann constant, and is the isothermal compressibility, T_f is a fictive temperature.

Rayleigh scattering also accounts to the scattering of centers much smaller than the wavelength of the incident light (Figure 23). The losses due to this phenomenon are proportional to $1/\lambda^4$, which is why short wavelengths are not used in telecommunication, due to the important losses at lower wavelengths. The intensity of the light scattered by those small scattering centers can be express such as:

$$I = I_0 \frac{1 + cos^2\theta}{2R^2} \left(\frac{2\pi}{\lambda}\right)^4 \left(\frac{n^2 - 1}{n^2 + 2}\right)^2 \left(\frac{d}{2}\right)^6$$

with I the light scattered by any of the small spheres of diameter d and refractive index n from a beam of unpolarized light of wavelength λ and incident intensity I_0, R the distance to the scattering center and θ the scattering angle.

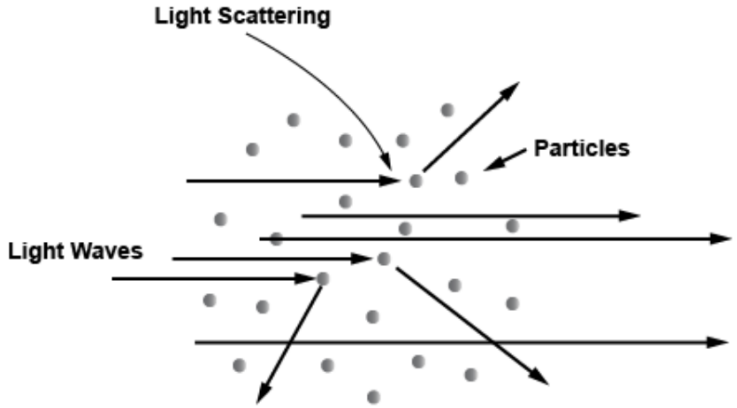

Figure 23. Schematic of light waves scattering on particles much smaller than the wavelength.

3.3.2.1.2 Mie scattering

Mie scattering, named after Gustav Mie, is another type of elastic scattering occurring in glasses. Impurities such as particles, crystals, bubble and other types of geometrical defects with a size comparable of the incident wavelength lead to scattering [69]. The scattered intensity is proportional to the inverse square of the wavelength such as: $I \sim 1/\lambda^2$.

3.3.2.2 Inelastic scattering losses

3.3.2.2.1 Brillouin *scattering*

Under the influence of temperature, the atoms constituting the glass network oscillate around their equilibrium positions due to the thermal agitation (Figure 24). The phonons created by the vibrations of

the network couple each other's locally modifying the refractive index of the medium, ultimately leading to the creation of low amplitude acoustic waves. When an electromagnetic wave propagates through a medium, it is scattered in all direction by those elastic waves. By Doppler effect, the acoustic wave itself propagating along the fiber, the scattered wave generation is frequency shifted compared to the incident wave. When the acoustic wave is moving in the same direction as the incident wave, the scattered wave, called Stokes, is shifted to lower frequency. The same way, where the scattered wave is moving backward the incident wave, it is called anti-Stokes.

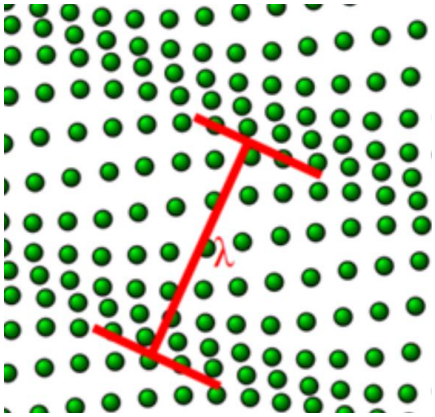

Figure 24. Representation of an acoustic wave propagating through an atomic network.

3.3.2.2.2 Raman Scattering

Raman scattering is the result of the interaction of an electromagnetic wave, called pump, and a variety of oscillators (molecules), in resonance at a certain frequency Ω_R, corresponding to an intramolecular vibration mode (optical phonon) of the molecule. In solids such as glasses, the phenomena can be explained by the energy transfer of the photons to the medium's phonons as shown on Figure 25.

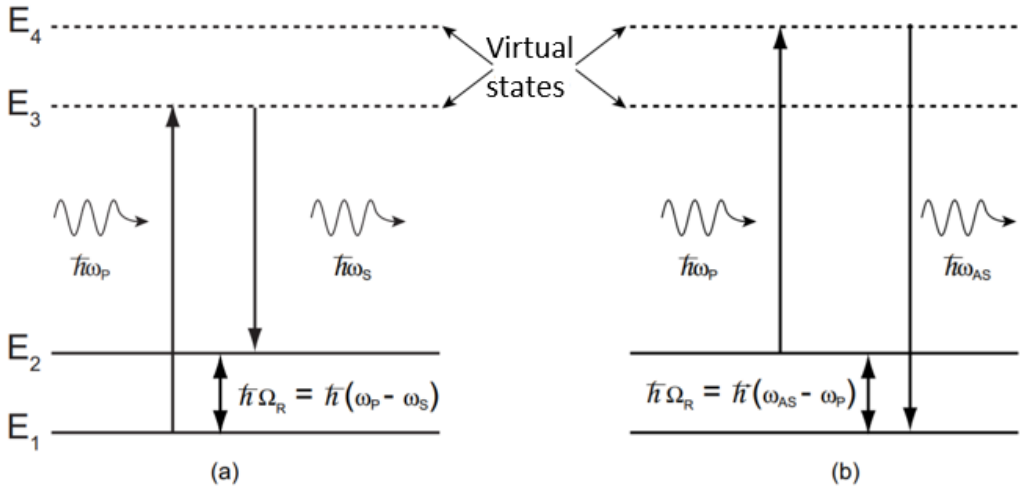

Figure 25. Energy diagram describing (a) stokes Raman scattering and (b) anti-stokes Raman scattering.

The overall intensity scattered through a medium is shown in Figure 26.

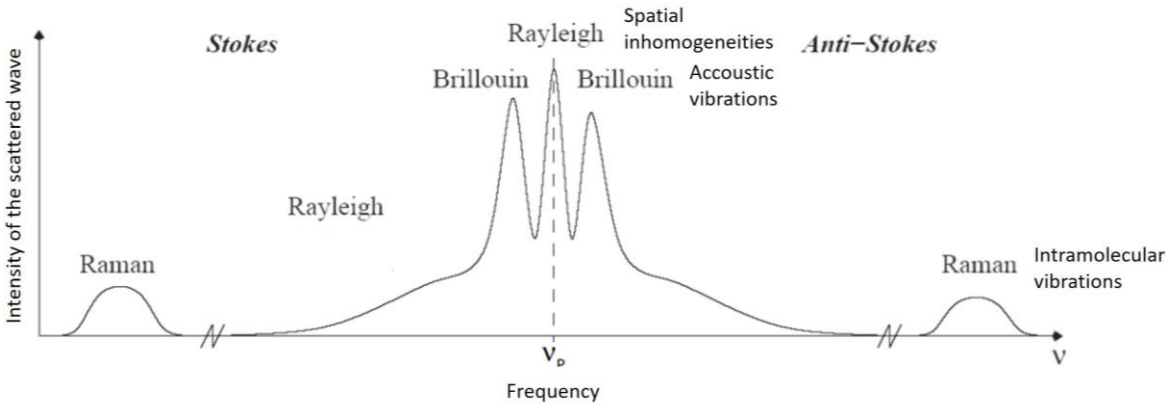

Figure 26. Schematic of a typical scattering spectra at a pump frequency v_p.

3.3.3 Bending losses

In optical fibers, due to bends or inhomogeneities at the core/cladding interface, the total internal reflection condition is not fulfilled leading to modes escaping the core. For monomode optical fibers, bending losses can account up to 0,005 dB/m for a bend radius of 30 mm [70].

3.3.4 Total attenuation

Along a fiber optic, all the effect previously mention lead to a loss of the signal, which can be expressed in dB/m or dB/km such as:

$$\alpha(\lambda) = \frac{10}{L}\log\frac{P}{P_0}$$

with α(λ) the attenuation in dB/km, L the distance travelled by the signal (km), P_0 the signal power injected in the optical fiber (W) and P the signal power after propagating along a distance L (W).

For a fiber optic made of silica, the typical attenuation spectrum is shown on Figure 27.

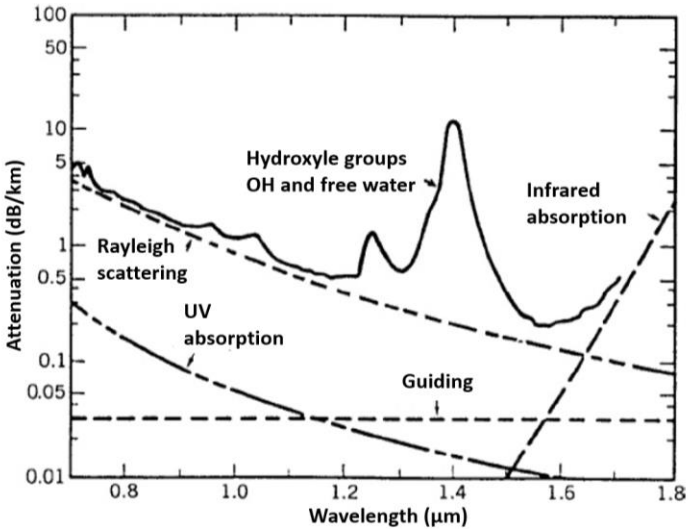

Figure 27. Attenuation of a silica mono-mode optical fiber [71].

3.4 Chromatic dispersion

Chromatic dispersion can be divided into two types: the material dispersion and the waveguide dispersion. A pulse is never purely monochromatic and the refractive index of the glass constituting the optical fiber depends on the wavelength. Considering the various wavelengths are propagating at different speed, it leads to a temporal broadening of the pulse. Chromatic dispersion is given by the contribution of the material dispersion and the waveguide dispersion. The material dispersion can be approximated by the Sellmeier equation [72]:

$$n^2(\omega) = 1 + \sum_{j=1}^{m} \frac{B_j \lambda_j^2}{\lambda_j^2 - \lambda^2}$$

With $\omega = \frac{2\pi}{\lambda} c$, the frequency of the pulse (with c the speed of light in vacuum), λ the considered wavelength in vacuum, λ_j the wavelength of the resonance in vacuum and B_j a constant associated with the resonance j.

Considering different wavelengths travel at different speeds, the initial pulse broadens as it propagates through the optical fiber. We generally use the propagation constant β(ω) expressed as a Taylor series around the frequency ω_0 to quantify the chromatic dispersion such as:

$$\beta(\omega) = n(\omega)\frac{\omega}{c} = \beta_0 + \beta_1(\omega - \omega_0) + \frac{1}{2}\beta_2(\omega - \omega_0)^2 + \cdots + \frac{1}{m!}\beta_m(\omega - \omega_0)^m$$

where:

$$\beta_m = \frac{d^m \beta}{d\omega^m}\Big|_{\omega=\omega_0} \quad with \quad (m = 0.\,1.\,2.\,3\ldots)$$

In this limited development, we can see higher order dispersive terms. The first dispersive order β_1 describes the group velocity of v_G mode while n_G is the group refractive index:

$$\beta_1 = \frac{1}{v_G} = \frac{n_G}{c} = \frac{1}{c}\left(n + \omega\frac{dn}{d\omega}\right)$$

The second dispersive order term 2 (β_2) corresponds to the group velocity dispersion (GVD) of the material such as:

$$\beta_2 = \frac{\partial \beta_1}{\partial \omega} = -\frac{1}{v_G^2}\frac{\partial v_G}{\partial \omega}$$

For the pulse propagation in optical fiber, another parameter is often used: the dispersion parameter D(λ) in $ps.nm^{-1}.km^{-1}$ [73].

$$D(\lambda) = -\frac{\lambda}{c}.\frac{d^2 n}{d\lambda^2} = \frac{-2\pi c}{\lambda^2}.10^6.\beta_2 \quad (ps.nm^{-1}\,km^{-1})$$

When D is negative, this is the normal dispersion regime ($\beta_2 > 0$), the longer wavelengths travel faster than shorter wavelengths whereas when D is positive, anomalous dispersion regime ($\beta_2 > 0$), longer wavelengths travel slower than shorter wavelengths.

The structure of the photonic crystal fiber allows to tailor its dispersion profile to control the position the ZDW (Figure 28), depending on the structure of the PCF (numbers and geometry of holes, nanostructuration of the core).

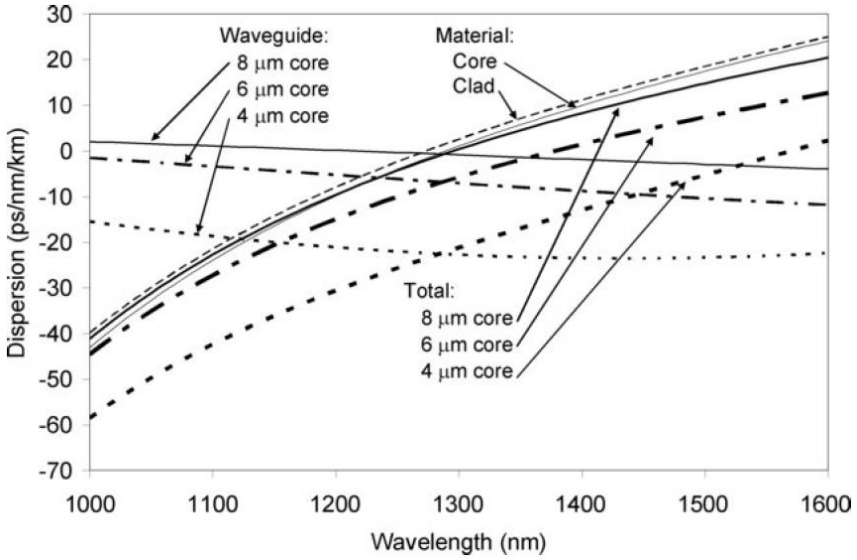

Figure 28. Material, waveguide dispersion, and total dispersion of step index fibers doped with GeO for three core diameters μm [74].

3.5 Photonic crystal fibers

In 1996, Knight et al. [63] developed the first photonic crystal fiber (PCF) making a breakthrough in optical fiber technology. PCF were characterized by holes into the cladding with a diameter d, each of which are separated by a distance Λ (called pitch) (Figure 29). Holes are periodically arranged as a network to obtain an effective refractive index in the cladding, allowing to tailor the dispersion profile of the optical fiber. More recently, a new method involving the nanostructuration of all-solid PCF by the stack and draw emerged, offering great versatility in the dispersion profile management.

3.5.1 Holey photonic crystal fibers

Figure 29 compares the structure of holey PCF with a typical step-index optical fiber. The inclusion of defects such as air holes modify the effective refractive index of the classing leading to the same propagation mechanism to step-index fiber, total internal reflection. The confinement if due to the refractive index difference of the core and the effective refractive index of the cladding Δn.

These holy PCFs are generally produced by extrusion [75] or more marginally by the stack and draw method [76-77].

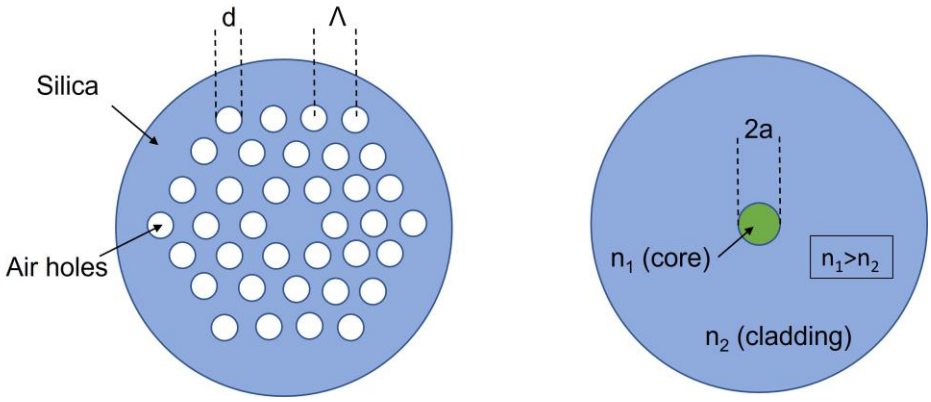

Figure 29. Comparison of a solid core PCF with a classical step-index optical fiber.

3.5.2 Hollow core Photonic Crystal Fibers

Photonic bandgap fibers (hollow core PCF) guide light in a lower refractive index hollow air core surrounded by a microstructured cladding (Figure 30). Hollow core PCFs exhibit extremely low nonlinearity, high damage threshold, zero dispersion at any design wavelength, and negligible interface reflection. The nonlinearity of air is really low and has an excellent transmission from UV to infrared. Hollow core PCFs transmit light by the photonic forbidden bandgap allowing to guide high energy signals due to the low absorption of air. Hollow core fibers also present the advantage of being easily modified by injecting a gas or a liquid in the hollow core in order to tweak their optical properties [78-79].

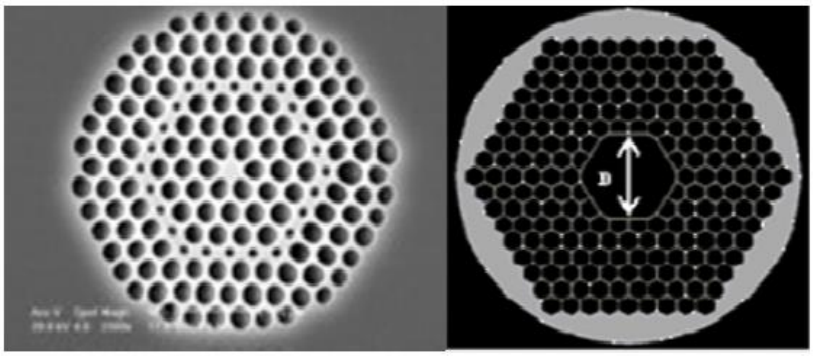

Figure 30. Example of photonic crystal fibers: (left) solid core holey fibers, (right) hollow core PCF [80].

3.5.3. All solid photonic crystal fibers

For the first time, Feng et al. present all-solid microstructured core optical fiber [81]. In this case, the air holes were replaced by a second glass with a slightly lower refractive index and comparable thermal properties (thermal expansion coefficients). For this first all-solid PCF (Figure 31), the losses were around 5 dB/m at 1550 nm. This type of fibers, made by the stack and draw method generally has a high refractive index difference Δn between the core and the cladding compared to classical step-index fibers.

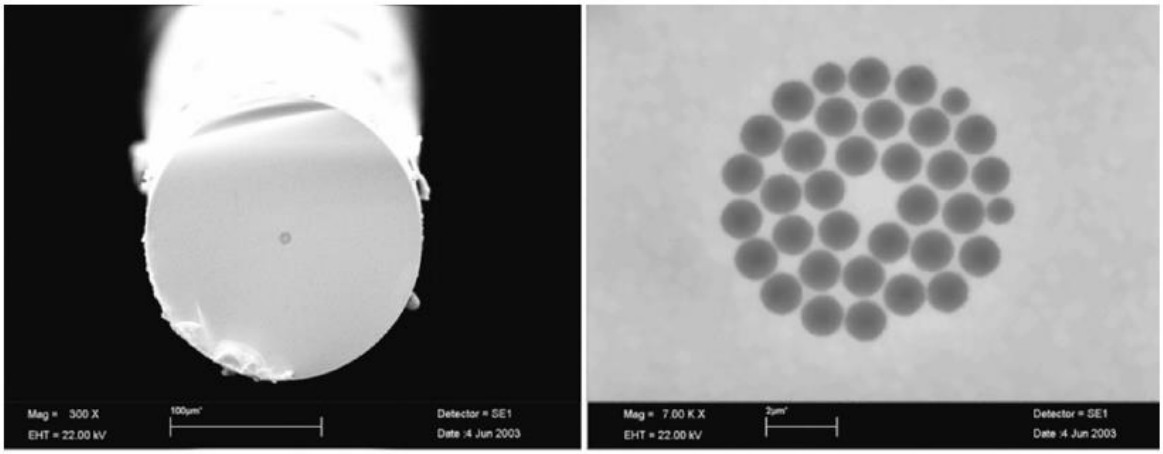

Figure 31. Scanning Electron Microscopy (SEM) of the first All-Solid Photonic Crystal Fiber (PCF) made by Feng [81].

4. Non-linear optical properties

Nonlinear optic applications have gathered a lot of attention these last decades due to the potential for a wide range of industries such as broadband light sources for spectroscopy and imagery. Depending on the nonlinear properties of the materials, the dispersion profile as well as the pulse regime used, various nonlinear effects arise.

4.1 Non-linear polarization

When a dielectric medium is subjected to an electric field, the medium will be polarized. When the electric field is strong enough this induces a non-linear response. The macroscopic total polarization can be written:

$$P = \varepsilon_0(\chi^{(1)}E + \chi^{(2)}EE + \chi^{(3)}EEE + ..)$$

with ε_0: vacuum permittivity, $\chi^{(i)}$: dielectric susceptibility or order i.

This polarization can be decomposed in two different terms, the linear response, and the non-linear response such as:

$$P = P_L + P_{NL} \text{ with } P_L = \varepsilon_0\chi^{(1)}E \text{ and } P_{NL} = \varepsilon_0(\chi^{(2)}EE + \chi^{(3)}EEE + ..).$$

Considering the isotropic nature of amorphous material such as glasses, the second order nonlinear susceptibility term $\chi^{(2)}$ is equal to zero.

4.2 Kerr effect

The Kerr effect has been discovered in 1875 by the physicist John Kerr. He noticed that the refractive index varies with the intensity of the incident electromagnetic wave such as:

$$n = n_0 + n_2.I$$

with n the refractive index, n_0 the linear refractive index, n_2 the non-linear refractive index and I the intensity of the incident electromagnetic wave.

The total refractive index is thus the sum of a linear component, linked to the first order susceptibility of the glass, and a non-linear component linked to the third order susceptibility of the glass. If the intensity is low, the non-linear contribution will be weak.

For silica, the non-linear refractive index equals $2.2.10^{-20}$ $m^2.W^{-1}$ at 1064 nm, $5.11.10^{-19}$ $m^2.W^{-1}$ at 1064 nm for tellurite [82] and $2.8.10^{-18}$ $m^2.W^{-1}$ for chalcogenides fibers ($Ge_{23}Sb_7S_{70}$) at 1064 nm [83]. For chalcogenide fibers it can go up to $2.4.10^{-17}$ $m^2.W^{-1}$ at 1550 nm which makes them the glassy material with the highest nonlinearity. Table 5 summarizes the linear and nonlinear properties of various glasses across the three main families.

Table 5. Linear and nonlinear refractive index of various glass across the 3 main glass families as well as their zero-dispersion wavelength (ZDW).

Type of glasses	**Main component**	**n_0**	**n_2 x 10^{20} (m^2/W)**	**ZDW (µm)**
Oxides				
Pure silica (SiO_2)	SiO_2	1.45 at 1.06 µm	2.7 at 1.06 µm	1.26
Lead Silicate (SF57)	SiO_2-PbO	1.81 at 1.06 µm	41 at 1.06 µm	2
Bismuth oxyde	Bi_2O_3	2.02 at 1.55 µm	32 at 1.55 µm	2.29
Tellurites (TZN)	TeO_2-ZnO-Na_2O	2.1 at 1.06 µm	51 at 1.06 µm	2.24
Fluorides				
Fluorozirconates (ZBLAN)	ZrF_4-BaF_2-NaF	1.50 at 1.06 µm	3.3 at 1.06 µm	1.62
Chalcogenides				
GeAsSe	GeAsSe	2.70 at 1.55 µm	2200 at 1.55 µm	~7
GLSO	Ga_2S_3-La_2O_3	2.25 at 1.55 µm	177 at 1.55 µm	4.64
As_2S_3	As_2S_3	2.44 at 1.55 µm	200 at 1.55 µm	4.81
As_2Se_3	As_2Se_3	2.81 at 1.55 µm [84]	1100-2400 at 1.55 µm [85]	~6

We notice that the linear refractive index n_0 varies from 1.45 to 2.1 for heavy metal oxides while chalcogenides vary from 2.2 to 3.3. The modification of the silica glass network with heavier atoms and modifiers creates non-bridging oxygens more polarizable, increasing the linear and nonlinear refractive indices n_0 and n_2. The non-linearity varies as a function of the polarizability of the cation and anion composing the glass network as explained before, in section 4. HMOG and chalcogenides glasses. Their nonlinear indices are 100 to 1000 times bigger respectively than silica glass (Figure 32), making them the best candidates for nonlinear optical fibers.

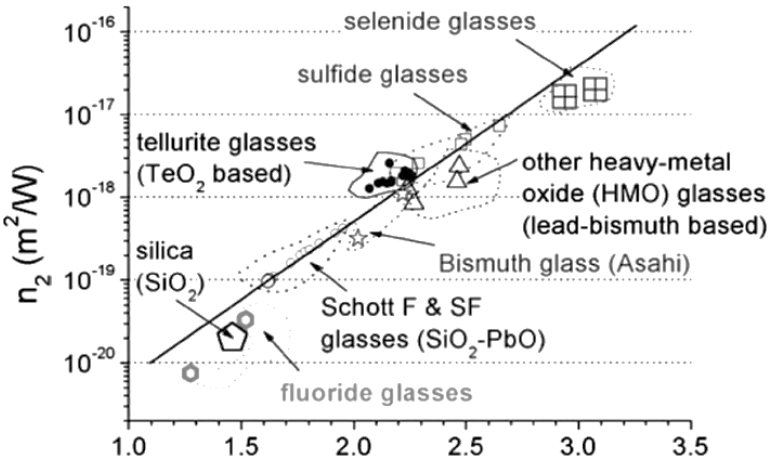

Figure 32. Nonlinear refractive index n_2 of various glass families as a function of their linear refractive index n_0 [86].

Fluorides and silica glasses are not good candidates for nonlinear mid-IR optic considering their low nonlinear refractive index, despite having a large transparency window concerning fluorides glasses. For chalcogenides, tellurides have a larger nonlinearity compared to selenides, higher than sulfides. Concerning heavy metal oxides, the modification of the glass network with heavy oxides such as Ti^{4+}, Nb^{5+}, Bi^{3+}, Te^{4+}, Pb^{+2} etc, allows to drastically increase the non-linearity as well as the transparency window of oxides glasses.

4.2.1 Non-linear Schrödinger equation (NLSE)

The non-linear Schrödinger equation (NLSE) governs the propagation of an electromagnetic (EM) wave in a fiber optic, independently of its nature, linear or nonlinear. NLSE takes into consideration the losses, the dispersion and the Kerr effect such as:

$$\frac{\partial A(z,t)}{\partial z} = -\frac{i\beta_2}{2}.\frac{\partial^2 A(z,t)}{\partial T^2} + i\gamma|A(z,t)|^2 A(z,t)$$

4.2.2 Self-phase modulation (SPM)

The first nonlinear effect in the context of short pulses supercontinuum (SC) generation in normal or anomalous regime is the self-phase modulation (SPM). This phenomenon leads to a spectral broadening of short optical pulses because of the intensity dependence of the refractive index n as explained previously, while preserving the temporal profile of the pulse. When a pulse travel along an optical fiber; this instantaneous and local change of the refractive index induces a phase shift of the electric field, leading to the decrease in frequency of the wavefront while it increases the frequency at the back of the wavefront (Figure 33).

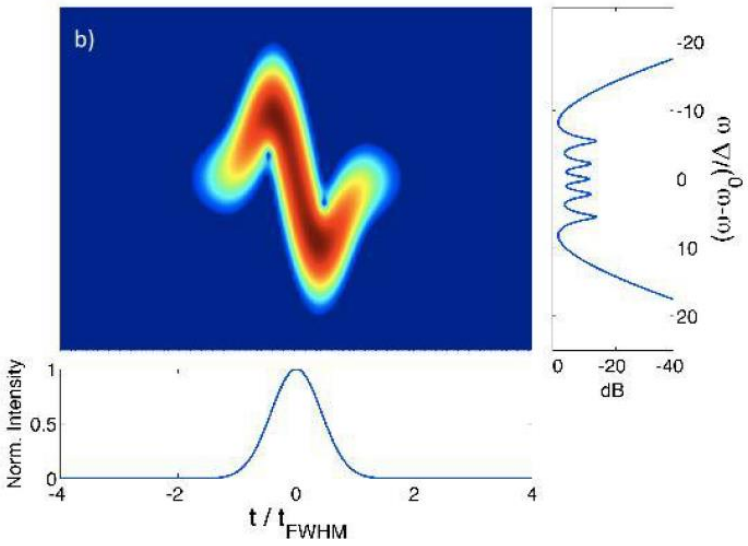

Figure 33. SPM induced spectral broadening for a Gaussian pulse shape and the corresponding nonlinear phase shift of the pulse with Φ_{NL}^{max} *= 5:5π [87].*

4.2.3 Four wave mixing

Four wave mixing (FWM) consists of the annihilation of two photons of frequency ω_1, ω_2 and the creation of two other frequency-detuned photons at ω_3 and ω_4. An interesting aspect of the FWM appears when strong pump waves have the same frequency ($\omega_1 = \omega_2 = \omega_P$) and create photon pair at frequencies ω_s and ω_i, which represent respectively a Stokes/signal and an anti-Stokes/idler wave. In such a case, it corresponds to degenerate FWM phenomena (Figure 34).

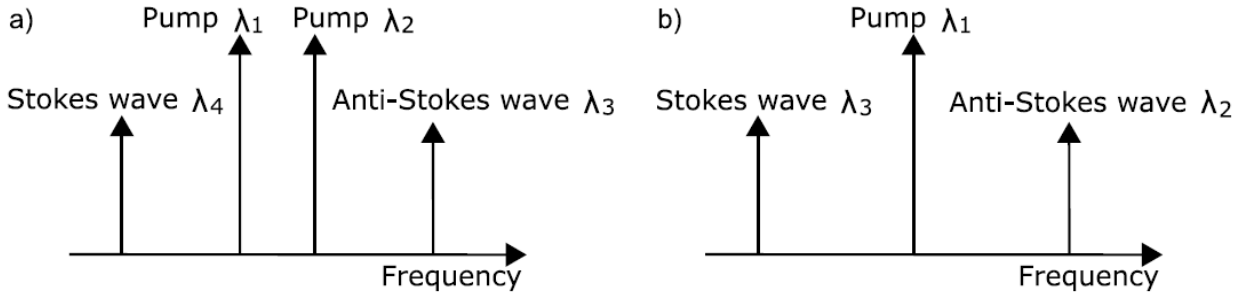

Figure 34. Schematic of four wave mixing for (a) 2 pump waves and (b) 1 pump wave (degenerated case).

4.2.4 Soliton

In the anomalous dispersion regime D>0 (β_2<0), there is a balance between SPM and dispersion which leads to the formation of solitons. Thus, a soliton is an optical pulse that preserves its spectral shape and duration width when propagating in a nonlinear optical fiber. Furthermore, solitons are solutions of the NLSE.

4.2.5 Dispersive wave

A specific aspect of the FWM is the phenomenon of dispersive wave generation. Indeed, an exchange of energy between the pump and a soliton (in the anomalous dispersion regime) is possible which leads to a creation of a pulse in the normal dispersion regime.

4.3 Supercontinuum generation

The first SCG was shown in a silica fiber in 1970 by Alfano and Shapiro [88]. In optics, a supercontinuum (SC) appears when a collection of nonlinear processes acts together upon a pump beam to induce a broadening of the initial pump spectrum [89]. The spectral broadening strongly depends on the pulse regime used, its intensity, the nonlinearity of the material, the length of the optical fiber as well as its attenuation characteristics. In the femtosecond regime, these nonlinear effects are mostly SPM, optical solitons and dispersive waves generation while picosecond, nanosecond pulses and continuous wave will favor modulation instability, FWM as well as stimulated Raman scattering.

Conclusion

As introduced in this chapter, various glass families of interest have various applications mechanics, medicine, bio-imagery or chemical sensing. In this chapter, we have presented the glassy state basic characteristics as well as optical fiber technology. The non-linear effects occurring in fiber optics were also briefly presented. The present thesis will focus on heavy metal oxides glasses development for the production of lenses by the hot embossing method as well as chalcogenides nanostructured core gradient index fibers made by the stack and draw method for supercontinuum generation and the production of optical components.

References

[1] M. H. Chopinet, J.D. Musgraves, J. Hu, L. Calvez (eds), "The History of Glass Springer Handbook of Glass.", Springer Handbooks. Springer, Cham. (2019). https://doi.org/10.1007/978-3-319-93728-1_1

[2] M. Smirniou and T. Rehren. "Direct evidence of primary glass production in late bronze age Amarna, Egypt.", Archaeometry, 53(1), pp58–80, (2010). https://doi.org/10.1111/j.1475-4754.2010.00521.x

[3] J. E.Ericson, E. Jonathon, A. Makishima, J. D. Mackenzie, R. Berger. "Chemical and physical properties of obsidian: a naturally occuring glass.", *Journal of Non-Crystalline Solids* 17, no. 1, pp129-142 (1975.)

[4] A. Velo-Gala, J. A. Garriguet Mata, J. A., "Roman window glass: an approach to its study through iconography. Lucentum, XXXVI.", pp159-176 (2017). http://dx.doi.org/10.14198/LVCENTVM2017.36.10

[5] S. Venck, F. St-Hilaire, L. Brilland, A. N. Ghosh, R. Chahal, C. Caillaud, M. Meneghetti, J. Troles, F. Joulain, S. Cozic, S. Poulain, G. Huss, M. Rochette, J. M. Dudley, T. Sylvestre, "2–10 µm Mid-Infrared Fiber-Based Supercontinuum Laser Source: Experiment and Simulation." *Laser & Photonics Reviews*, 14, pp2000011. (2020). https://doi.org/10.1002/lpor.202000011

[6] J. A. Harrington. "Infrared fibers and their applications." SPIE-International Society for Optical Engineering (2003).

[7] X. Liu, "Evolution of Fiber-Optic Transmission and Networking toward the 5G Era.", *iScience* vol. 22 pp489-506 (2019). doi:10.1016/j.isci.2019.11.026

[8] Ph.D. thesis, S. Maurugeon, « Fibres infrarouges pour l'optique spatiale », University of Rennes 1, UMR CNRS 6229, France.

[9] J. Zarzycki, « *Les verres et l'état vitreux »* Ed. Masson (1982).

[10] E. D. Zanotto and J. C. Mauro, "The glassy state of matter: Its definition and ultimate fate.", *Journal of Non-Crystalline Solids*, *471*, pp490-495 (2017). https://doi.org/10.1016/j.jnoncrysol.2017.05.019

[11] Ph.D. thesis, O. Gulbiten, "An Investigation of Dynamic Processes in Selenium Based Chalcogenide Glasses (arizona.edu).", University of Arizona, USA (2014).

[12] J. Barton, C. Guillemet, « *Le verre: Sciences et Technologies.»*, Ed. Broché (2005).

[13] Vogel, 1921; Flucher, 1925; Tammann, (1926).

[14] C.A. Angell, "Relaxation in liquids, polymers and plastic crystals — strong/fragile patterns and problems.", Journal of. Non-Crystalline. Solids. Vol. 131-133 Part 1, pp13-31 (1991).

[15] P. M. Woodward, P. Karen, J. S. O. Evans, T. Vogt, "Solid state material chemistry", Cambridge University Press,Chap 8, pp309-310 (2021).

[16] L. Calvez. "Chalcogenide glasses and glass-ceramics: Transparent materials in the infrared for dual applications.", Comptes Rendus Physique 18.5–6, pp314–322 (2017).

[17] W. H. Zachariasen, "The atomic arrangement in glass.", Journal of the American Society 54, pp3841-3851 (1932).

[18] W. Vogel, “Glass chemistry.”, Springer-Verlag 1 (1992).

[19] A. Dietzel. "The cation field strengths and their relationship to devitrification processes, compound formation and the melting points of silicates.", *Journal of Electrochemistry and Applied Physical Chemistry* 48, no. 1, pp9-23 (1942).

[20] K-H. Sun. "Fundamental condition of glass formation.", *Journal of the American Ceramic Society* 30, no. 9, pp277-281 (2006).

[21] A-M, Raschid, A. Zandona, and J. Deubener. "Kinetic fragility of pure TeO_2 glass.", *Journal of Non-Crystalline Solids* 554, 120595 (2021).

[22] M. M. Smedskjaer, R. E. Youngman, and J. C. Mauro. "Principles of Pyrex® glass chemistry: structure–property relationships.", *Applied Physics A* 116, no. 2, pp491-504 (2014).

[23] M. C. Onbaşlı, A. Tandia, and J. C. Mauro. "Mechanical and compositional design of high-strength Corning Gorilla® Glass.", *Handbook of Materials Modeling: Applications: Current and Emerging Materials*, pp1997-2019 (2020).

[24] X. Forestier, J. Cimek, I. Kujawa, R. Kasztelanic, D. Pysz, K. Orliński, R. Stępień, and R. Buczyński. "Study of SiO_2-PbO-CdO-Ga_2O_3 glass system for mid-infrared optical elements.", *Journal of Non-Crystalline Solids* 503, pp52-61 (2019).

[25] R. Stepien, D. Pysz, I. Kujawa, and R. Buczynski. "Development of silicate and germanate glasses based on lead, bismuth and gallium oxides for midIR microstructured fibers and microoptical elements.", *Optical Materials* 35, no. 8, pp1587-1594 (2013)

[26] Pengfei Wang, Shijie Jia, Xiaosong Lu, Yuxuan Jiang, Jibo Yu, Xing Wang, Shunbin Wang and Elfed Lewis, “Advanced functional materials”, Chapter 15 “Tellurite glass and its application in lasers, Tellurite Glasses-Synthesis, Charaterizaton and Applications.”, IntechOpen, (2020).

[27] N. M. Shash, F. E. Salman, M. K. El-Mansy, H. A. Ghodair. “Influence of lithium phosphate concentration and temperature on the electrical conduction of $(76V_2O_5–24P_2O_5)1 − X(Li_3PO_4)X$ glasses.”, J. Phys. Chem. Solids, 65, pp891-900 (2004). 10.1016/j.jpcs.2003.09.030

[28] J.A. Wilder, “Glasses and glass ceramics for sealing to aluminum alloys.”, J. Non-Cryst. Solids, 38 & 39, pp879-884 (1980). 10.1016/0022-3093(80)90548-7

[29] S. M. Hsu, S. W. Yung, R. K. Brow, W. L. Hsu, C. C. Lu, F. B. Wu, *et al., “*Effect of silver concentration on the silver-activated phosphate glass.”, Mater. Chem. Phys., 123, pp172-176 (2010). 10.1016/j.matchemphys.2010.03.078

[30] J. H. Campbell, T. I. Suratwala, “Nd-doped phosphate glasses for high-energy/high-peak-power lasers.”, J. Non-Cryst. Solids, 263-264, pp318-341 (2000). 10.1016/S0022-3093(99)00645-6

[31] T. Gilchrist, M.A. Glasby, D.M. Healy, G. Kelly, D.V. Lenihan, K.L. McDowall, *et al., “*In vitro nerve repair–in vivo. The reconstruction of peripheral nerves by entubulation with biodegradeable glass tubes–a preliminary report.”, Br. J. Plast. Surg., 51, pp231-237 (1998). 10.1054/bjps.1997.0243

[32] I. Ahmed, M. Lewis, I. Olsen, J. C. Knowles, “Phosphate glasses for tissue engineering: part 1. Processing and characterisation of a ternary-based P2O5–CaO–Na2O glass system.”, Biomaterials, 25, pp491-499 (2004). 10.1016/S0142-9612(03)00546-5

[33] M. Uo, M. Mizuno, Y. Kuboki, A. Makishima, F. Watari, “Properties and cytotoxicity of water soluble Na_2O-CaO-P_2O_5 glasses.”, Biomaterials, 19, pp. 2277-2284 (1998). 10.1016/S0142-9612(98)00136-7

[34] T. Minami, J.D. Mackenzie, “Thermal expansion and chemical durability of phosphate glasses.”, J. Am. Ceram. Soc., 60, pp232-235 (1977). 10.1111/j.1151-2916.1977.tb14113.x

[35] I. Ahmed, H. Ren and J. Booth, “Developing Unique Geometries of Phosphate-Based Glasses and their Prospective Biomedical Applications.”, *Johnson Matthey Technology Review* (2019).

[36] R.K. Brow, “Review: the structure of simple phosphate glasses.”, J. Non-Cryst. Solids, 263, pp1-28 (2000). 10.1016/S0022-3093(99)00620-1

[37] C.M. Baldwin, R.M. Almeida, J.D. Mackenzie, “Halide glasses.”, *Journal of Non-Crystalline Solids*, 43, pp309–344 (1981).

[38] K-H. Sun, “Fundamental Condition of Glass Formation.”, *Journal of the American Ceramic Society*, 30, pp277–281 (1947).

[39] M. Poulain, M. Poulain, J. Lucas, « Verres fluorés au tétrafluorure de zirconium propriétés optiques d’un verre dopé au Nd3+.», *Materials Research Bulletin*, 10, pp243–246 (1975).

[40] M. Poulain, J. Lucas, ”Une nouvelle classe de materiaux: les verres fluores au tetrafluorure de zirconium.”, Verres Réfract. 32, 4, pp505-513 (1978).

[41] M. Poulain, "Fluoride glass Fiber Optics.", Fluoride Glass composition and Processing, ed. I. Aggarwal and G. Lu, Acad. Press, Boston (1991).

[42] Y. Miyajima, T. Komukai, T. Sugawa, T. Yamamoto, ”Rare Earth-Doped Fluoride Fiber Amplifiers and Fiber Lasers.”, Optical Fiber Technology, 1, pp35–47 (1994).

[43] G. Qin, X. Yan, C. Kito, M. Liao, C. Chaudhari, T. Suzuki, and Y. Ohishi, "Ultrabroadband supercontinuum generation from ultraviolet to 6.28 μ m in a fluoride fiber.", *Applied Physics Letters* 95, no. 16, pp161103 (2009).

[44] D. S. Tucker and M. SanSoucie, "Production of ZBLAN Optical Fiber in Microgravity.", *Optical Fiber Sensors Conference 2020 Special Edition*, G. Cranch, A. Wang, M. Digonnet, and P. Dragic, eds., OSA Technical Digest, paper T2B.1 (2020).

[45] A. Lemière, F. Désévédavy, B. Kibler, P. Mathey, G. Gadret, J.-C. Jules, C. Aquilina, P. Béjot, F. Billard, O. Faucher, et al., “Mid-infrared two-octave spanning supercontinuum generation in a Ge–Se–Te glass suspended core fiber.”. In: Laser Physics Letters 16.7, pp075402 (2019).

[46] J. H. Simmons, C. J. Simmons, R. Ochoa, A. C. Wright, ”Fluoride glass fiber optics.”, Fluoride glass structure, ed. I. Aggarwal and G. Lu, Acad. Press, Boston (1991).

[47] J.A. Savage, ”Materials for infrared fiber optics.”, Mat. Sci. Rep., 2, pp99-138 (1987).

[48] L. Sojka, Z. Tang, H. Zhu, E. Bereś-Pawlik, D. Furniss, A. B. Seddon, T. M. Benson, S. Sujecki, “Study of mid-infrared laser action in chalcogenide rare earth doped glass with Dy3+ Pr3+ and Tb3+.”, Opt. Mater. Exp., volume 2(11), pp1632-1640 (2012).

[49] A. Zakery, S.R. Elliott, “Optical properties and applications of chalcogenide glasses: a review.”, J. Non-Cryst. Solids, volume 330, pp1-12 (2003).

[50] X.H. Zhang, Y. Guimond, Y. Bellec, “Production of complex chalcogenide glass optics by molding for thermal imaging.”, J. Non-Cryst. Solids, volume 326–327, pp519-523 (2003).

[51] F. Starecki, F. Charpentier, J.L. Doualan, L. Quetel, K. Michel, R. Chahal, J. Troles, B. Bureau, A. Braud, P. Camy, V. Moizan, V. Nazabal, “Mid-IR optical sensor for CO2 detection based on fluorescence absorbance of Dy3+:$Ga_5Ge_{20}Sb_{10}S_{65}$ fibers.”, Sensors Actuat. B, volume 207 , pp518-525 (2015).

[52] M.L. Anne, C. Le Lan, V. Monbet, C. Boussard-Pledel, M. Ropert, O. Sire, M. Pouchard, C. Jard, J. Lucas, J.L. Adam, P. Brissot, B. Bureau, O. Loréal, “Fiber evanescent wave spectroscopy using the mid-infrared provides useful fingerprints for metabolic profiling in humans.”, J. Biomed. Opt., volume 14, pp054033 (2009).

[53] P. Lucas, C. Boussard-Plédel, A. Wilhelm, S. Danto, X. H. Zhang, P. Houizot, S. Maurugeon, C. Conseil, B. Bureau, “The development of advanced optical fibers for long-wave infrared transmission.”, Fibers, volume 1, pp110-118 (2013).

[54] S. Cui, C. Boussard-Plédel, J. Lucas, and B. Bureau, “Te-based glass fiber for far-infrared biochemical sensing up to 16 µm.”, Opt. Express, volume 22, pp21253-21262 (2014).

[55] L. Calvez, “Chalcogenide glasses and glass-ceramics: Transparent materials in the infrared for dual applications.”. Comptes Rendus Physique (2017). 10.1016/j.crhy.2017.05.003.

[56] J.-D. Colladon, “Souvenirs et mémoires.”, Genève, (1893).

[57] J.-D. Colladon, “La fontaine lumineuse.”, La Nature, vol. 12, pp325 (1884).

[58] A. C. S., Van Heel, “A new method of transporting optical images without aberration.”, Nature 17, pp39, (1954).

[59] K.C. Kao, et G.A. Hockham, “Dielectric-fibre surface waveguides for optical frequencies.”, Proc.Inst. Elect. Eng., 113, pp1151-1158 (1966).

[60] D. B. Keck, P. C. Schultz, US Patent 3711262.

[61] R.D. Maurer, P. C. Schultz, US Patent 3659915.

[62] G. Tanaka, M Watanabe, et K Yano, “Characteristics of pure silica core single-mode fiber.”, Fiber and Integrated Optics. 7(1), pp47 (1988).

[63] J. C. Knight, T. A. Birks, P.S. J. Russell, et D.M. Atkin, “All-silica single-mode optical fiber with photonic crystal cladding.”, Opt. Lett., 21 (19), pp1547-1549 (1996).

[64] R. Buczynski, “Photonic crystal fibers.”, Acta Physica Polonica A 106 (2), pp141–168 (2004).

[65] J. S. Sanghera and I. D. Aggarwal. “Development of chalcogenide glass fiber optics at NRL.”, Journal of non-crystalline solids 213, pp63–67 (1997).

[66] J.-L. Adam and X. Zhang. “Chalcogenide glasses: preparation, properties and applications”. Woodhead publishing (2014).

[67] F. Charpentier, J. Troles, Q. Coulombier, L. Brilland, P. Houizot, F. Smektala, C. Boussard-Plédel, V. Nazabal, N Thibaud, K. Le Pierres, et al. “CO2 detection using microstructured chalcogenide fibers.”, Sensor Letters 7.5, pp745–749 (2009).

[68] A. T. Young, "Rayleigh scattering", Appl. Opt. 20, pp533-535 (1981).

[69] W. C. Mundy, J. A. Roux, and A. M. Smith, "Mie scattering by spheres in an absorbing medium*.", J. Opt. Soc. Am. 64, pp1593-1597 (1974).

[70] O. Audouin, “Fibre optique monomode à dispersion décalée”. Patent EP0749024 A2.

[71] T. Miya, Y. Terunuma, T. Hosaka, et T. Miyoshita, “Ultimate low-loss single-mode fibre at 1,55 µm”, Electron. Lett., 15, pp106-108 (1979).

[72] Handbook of optics, Volume II, Part 5, chp 38&39 (1995).

[73] D. Mogilevtsev, T. A. Birks et P. St J. Russell, “Group velocity dispersion in photonic crystal fibers”, OpticsLetters, 23 (21), pp1662–1664 (1998).

[74] Ming-Jun Li and D. A. Nolan. “Optical transmission fiber design evolution”. Journal of Lightwave Technology 26.9 (2008).

[75] S.A. Cerqueira Jr, "Recent progress and novel applications of photonic crystal fibers.", *Reports on progress in physics* 73, no. 2, pp024401 (2010).

[76] F. Poli, A Cucinotta, and S. Selleri, ”*Photonic crystal fibers: properties and applications*.”, Vol. 102. Springer Science & Business Media (2007).

[77] P. Russell, Photonic crystal fibres,”Optical *Fiber Communication Conference.”*, Optical Society of America (2009).

[78] V. T. Hoang, R. Kasztelanic, G. Stępniewski, K. D. Xuan, V. C. Long, M. Trippenbach, M. Klimczak, R. Buczyński, and J. Pniewski, "Femtosecond supercontinuum generation around 1560 nm in hollow-core photonic crystal fibers filled with carbon tetrachloride," Appl. Opt. 59, pp3720-3725 (2020).

[79] A. I. Adamu, Y. Wang, R. Amezcua-Correa, O. Bang, and C. Markos, "Noble and Raman-active Gas-Filled Hollow-Core Fiber Lasers.", *OSA Advanced Photonics Congress (AP) 2020 (IPR, NP, NOMA, Networks, PVLED, PSC, SPPCom, SOF)*, L. Caspani, A. Tauke-Pedretti, F. Leo, and B. Yang, eds., OSA Technical Digest (Optica Publishing Group, 2020), paper SoW1H.6.

[80] B. Debord, A. Foued, V. Luca, G. Frédéric, and B. Fetah, "Hollow-Core Fiber Technology: The Rising of “Gas Photonics”.", *Fibers*7, no.2, pp16. 10.3390/fib7020016

[81] Feng, Xian, T. M. Monro, P. Petropoulos, V. Finazzi and D. W. Hewak. “Solid microstructured optical fiber.", *Optics express* 11 18, pp2225-2230 (2003).

[82] J. Cimek, N. Liaros, S. Couris, R. Stępień, M. Klimczak, and R. Buczyński, "Experimental investigation of the nonlinear refractive index of various soft glasses dedicated for development of nonlinear photonic crystal fibers.", *Optical Materials Express* 7, no. 10, pp3471-3483 (2017).

[83] J. Choi, Z. Han, BU. Sohn, *et al.*, "Nonlinear characterization of GeSbS chalcogenide glass waveguides.", *Sci Rep* 6, pp39234 (2016). https://doi.org/10.1038/srep39234

[84] R. E. Slusher, G. Lenz, J. Hodelin, J. Sanghera, L. B. Shaw, et I. D. Aggarwal, "Large Raman gain and nonlinear phase shifts in high-purity As2Se3 chalcogenide fibers.", J. Opt. Soc. Am., B 21, pp1146- 1155 (2004).

[85] X. Feng, A. K. Mairaj, D. W. Hewak, et T. M. Monro, "Nonsilica Glasses for Holey Fibers.", J. Lightwave Technol., 23, pp2046 (2005).

[86] J. H. V. Price et al., "Non-silica microstructured optical fibers for Mid-IR supercontinuum generation from 2 µm-5 µm.", Proceedings of SPIE 6102, 61020A (2006).

[87] Ph.D. Thesis, A. Heidt, "Novel coherent supercontinuum light sources based on all-normal dispersion fibers.", (1981).

[88] J. M. Dudley and J. R. Taylor, eds., "Supercontinuum Generation in Optical Fibers.", Cambridge, England: Cambridge University Press (2010).

[89] R. R. Alfano and S. L. Shapiro, Phys. Rev. Lett., Vol. 24, Issue 12, pp584–587 and pp592-594, Issue 22, pp1219-1222 (1970).

Chapter 2: Methods of characterization of glassy materials

In this chapter, the various measurements methods used for the characterization of the thermal and optical properties of the glasses used in this manuscript will be presented. The determination of glass properties such as the transition temperature, the glass stability criterion ΔT or the viscosity is primordial for glass science applications. The mechanical properties as well as the optical or thermal properties need to be compatible with the application. The most important criterions to produce lenses and optical fibers are first the thermal properties, allowing us to effectively draw fibers or produce micro-lenses without any presence of crystallization due to the various heat treatments involved in the process. And in a second time, it is crucial to obtain the optical properties desired such as the refractive index, the nonlinearity of the glass as well as the transmission range appropriate for the aimed application.

1. Thermal properties

The determination of the thermal properties of the glass plays a key role in the ability to produce an optical element [1-2]. Indeed, the process to fabricate optical fibers for example, involves several heat treatments as explained in Chapter 1. If the glass has a poor thermal stability, it will lead to the crystallization of the glass, changing the optical properties drastically due the crystalline phase of the glass. The viscosity of the glass also plays an important role, especially for the fabrication process. Either it is lenses by the hot-embossing technique [3] or the fabrication of optical fiber by the extrusion method [4] as well as by the stack and draw method [5], the working temperature of those processes requires a control over the viscosity of the material used. If the optical component is composed of multiple glassy materials, they must be compatible if they are fabricated during the same heat treatment, which is why DSC/DTA and dilatometry are fundamental for glass science. The determination of the viscosity of each glass allows us to assess the compatibility between each other as well as determining the temperature needed for the optical element forming. Various models, as explained in chapter one, have been built to estimate the viscosity of glasses. Here, we focus on three types of combined measurements: differential scanning calorimetry (DSC), dilatometry and hot stage microscopy (HSM).

1.1 Differential scanning calorimetry

The differential scanning calorimetry (DSC) technique was developed by E. S. Watson and M. J. O'Neill in 1962 [6]. The first adiabatic differential scanning calorimeter was used in biochemistry, developed by Privalov and Monaselidze in 1964 at Institute of Physics in Tbilisi, Georgia [7]. The transition temperature T_g and the crystallization temperature T_x in this work have been determined using a differential scanning calorimetry technique (DSC). This measurement also gives information on the viscosity, knowing that at the transition temperature T_g, the viscosity is close to $10^{-13.4}$ Poise.

We first grind a dozen milligrams of the glass before inserting it in a platinum crucible. An empty crucible used as a reference is inserted with the samples. We then heat up the sealed crucible with a heating rate

of 10 C/min to follow the evolution of the heat transfer difference from the sample crucible compared to the reference empty crucible. It allows us to determine crucial temperature characteristics as explained above, and to assess the glass network connectivity compared to another composition. Indeed, the highest the connectivity and bond strength, the higher will be the transition temperature.

1.2 Hot stage microscopy

Hot stage microscopy (HSM) is a combination of thermal analysis and microscopy allowing to observe changes in shape of a glass sample, as a function of the temperature [8]. The device consists of a halogen lamp light source, a tubular furnace cooled by water and a camera registering the evolution of the sample shape as a function of the temperature. Those three elements are mounted on a bench to keep a stable alignment (Figure 1). The evolution of the sample morphology is observed through the camera and is represented by:

(i) its surface area,

(ii) its angle with the substrate with the base and the top of the sample,

(iii) its shape factor, corresponding to the difference of the observed shape and a perfect half circle.

Figure 1. Hot stage microscope used for the measurements.

Characteristic temperatures depending on the measurement parameter, such as the heating rate, are defined as follow (Figure 2):

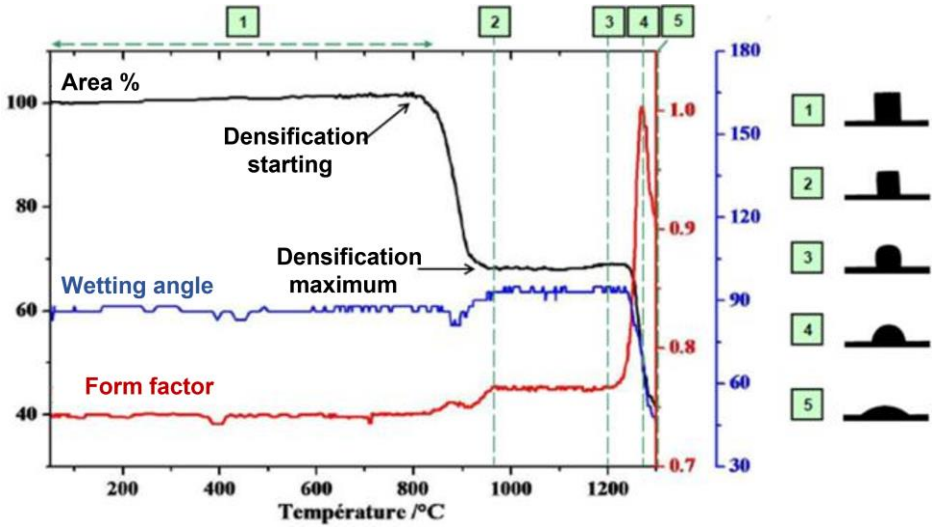

Figure 2. Typical HSM measurement describing the evolution of the sample with temperature.

- Initial shape of the measured sample (Fig. 2-1)
- The curvature temperature corresponds to the temperature at which the form factor varied 1.5% and when the upper corner of the sample varied 10% (Fig.2-2).
- The sphere creation temperature T_{sph} is the temperature at which the upper corner are rounds and at which the height equals the width (Fig.2-3).
- The hemisphere temperature T_{hs} corresponds to the temperature at which the form factor is superior or equal to 0.98, and the height inferior or equal to half of the width (Fig.2-4).
- The spreading temperature T_{spr} corresponds to the temperature at which the height is inferior or equal to the third of its height at the hemisphere temperature T_{hs} (Fig.2-5).

The viscosity can be estimated for those four characteristics temperature such as, for the curvature temperature's viscosity is about 10^9 Poises, at the sphere creation temperature T_{sph}, we estimate the viscosity of the glass to be 10^6 Poises, while the hemisphere temperature T_{hs} corresponds to viscosity of 10^4 poises and spreading temperature T_{spr} to a viscosity of 10^2 poises [9].

1.3 Thermomechanical analysis

Thermomechanical analysis (TMA) measures the variation of the dimension of a material with temperature [10-11]. This technique is used to characterize the linear expansion coefficient (CTE), the glass transition temperature T_g along with the dilatometric softening temperature T_{dst}. It consists in a tubular furnace and a holder and a thermal sensor. The sample is elongated and the deformation along the z axis is recorded by the computer. Here, we use a Bahr Analysis GmbH Dil801 dilatometer (Figure 3 and 4). The glass sample is cut in a rectangular shape with a length of 30 mm and a cross-section of 4x4 mm.

It is then introduced with the help of the holder inside the oven enceinte, with the thermal detector being located at the top of the central part of the sample. The expansion coefficient is given by the slope of the curve such as:

$$\frac{\Delta L}{L_0} = \alpha . \Delta T$$

with ΔL the length variation, L_0 the initial length of the sample, ΔT the variation of temperature in Kelvin and, the linear expansion coefficient in K^{-1}.

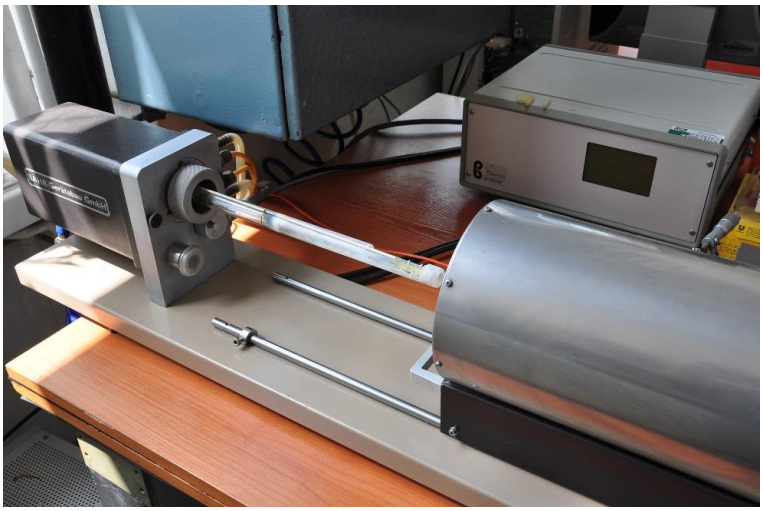

Figure 3. Bahr Thermoanalyse GmbH Dil801 dilatometer used for this study.

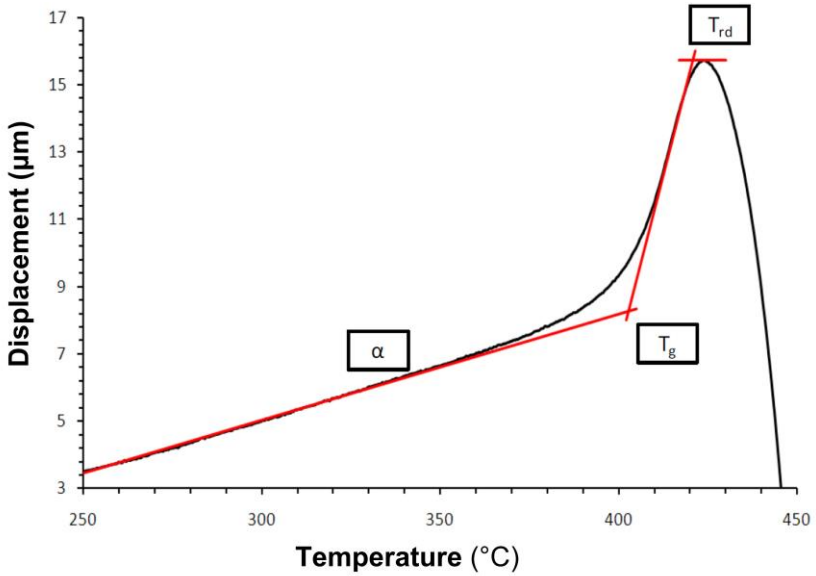

Figure 4. Example of thermomechanical analysis.

1.4 Thermal expansion coefficient

Thermal expansion coefficient (CTE) $\alpha_{\Delta T}$ represents the material dilatation under the influence of temperature such as:

$$\alpha_{\Delta T} = \frac{1}{l_0} \times \frac{\Delta l}{\Delta T} \qquad \text{or} \qquad \beta_{\Delta T} = \frac{1}{v_0} \times \frac{\Delta v}{\Delta T}$$

$\alpha_{\Delta T}$ and $\beta_{\Delta T}$ are respectively the linear and volumetric thermal expansion coefficient. L_0 and v_0 represents the initial length and initial volume while Δl and Δv represents their variation, and T the temperature. The interatomic distance varies with the temperature of the sample as shown on the Codon-Morse potential curve (Figure 5).

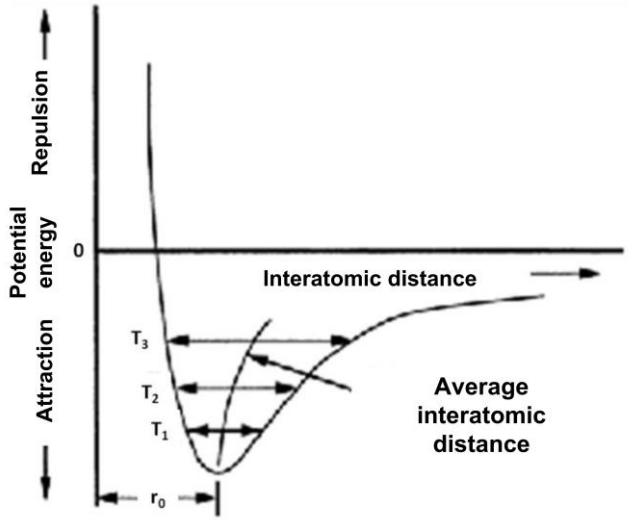

Figure 5. Condon-Morse potential curve illustrating the thermal expansion of chemical bonds [12].

This curve is the result of the interactions of the repulsive and attractive forces involved in the interatomic bonds of the atomic network such E_v.

$$E_v = -\frac{A}{R^n} + \frac{B}{R^m}$$

with A, B, n and m being constants and R the interatomic distance.

If the potential energy was symmetric, the average interatomic distance would be independent of the temperature. Considering that, in reality, the potential is asymmetric, we observe a variation of the interatomic distance with the temperature. We measured it using the dilatometer DIL801 mentioned previously.

1.5 Density

The density of the glass is measured multiple times using the well-known Archimedes method. Using distilled water as immersion liquid, at room temperature. It can be calculated taking into consideration the volumic mass ρ of water at the considered temperature such as:

$$d = \frac{m_{air} \cdot \rho_{water}}{m_{air} - m_{water}}$$

From the density and the average molar weight of the glass, the molar volume V_m can be calculated, as shown in chapter 3.

2. Optical properties

The determination of the optical properties of our glass and optical component is also primordial to the elaboration of fiber optic or lenses. As previously explained, the choice of the glass determines the physico-chemical properties of the final product. Here, we focused on the most important properties which are: the transmission characteristic as well as the refractive index and the dispersion.

2.1 Transmission

An electromagnetic wave propagating in a medium is partially reflected, absorbed, scattered, and diffracted as explained in chapter 1 leading to the attenuation of the incident EM, proportional to the length of propagation d as shown on Figure 6.

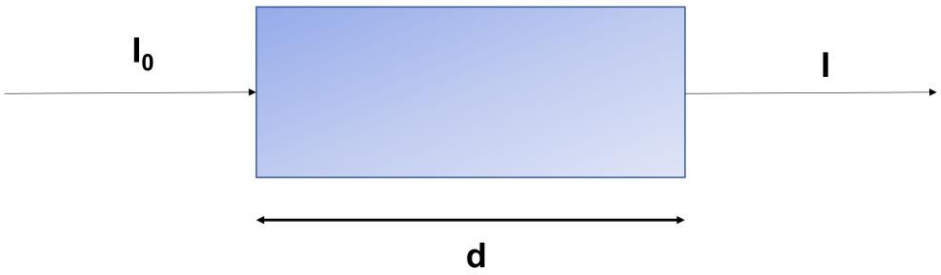

Figure 6. Attenuation of incident light propagating through a medium with a length d.

Transmittance T and absorbance A in a medium are defined such as:

$$A(\lambda) = \ln\left(\frac{I_0(\lambda)}{I(\lambda)}\right) = -\ln T$$

The transmittance T is defined as the intensity over the incident light to the output intensity while the absorbance A corresponds to the e base logarithm over the transmittance T. Absorbance and transmittance have no unit and depend on the nature of the medium, the incident wavelength as well as the concentration of molecules for liquid for example and their faculty to absorb certain wavelengths, called absorption constant σ. According to Beer-Lambert law, we can express A such as:

$$A(\lambda) = \sigma(\lambda).d.C$$

With σ(λ) the absorption coefficient at a certain wavelength λ, A a constant without unit, C the concentration and d the length of the medium.

The polishing procedure is essential to get faces as parallel as possible in order to get proper measurements. To measure the transmission spectra, samples of 1 mm and 10 mm are cut with a diamond saw and then polished with various polishing plates made of silicon carbide (SiC) using water as lubricant. The first plate is used to parallelize the faces of the sample with a fairly high grain size. Then, lower grain size grinding plates are used to reduce the roughness of the sample until we obtain optical grade quality which corresponds to 1 µm grinding polishing plates. A solution made of diamond particles is used in addition to the 1 µm plate to get an optical polishing grade sample of various thicknesses.

The two different thicknesses allow to calculate the attenuation of the bulk material as well as the optical fibers taking the difference of intensity and the thicknesses of the two samples ΔL into consideration such as:

$$\alpha(\lambda) = \frac{10}{\Delta L}.\log\frac{P}{P_0} \quad (dB/m)$$

with α(λ) in dB/m, ΔL in meters and P the intensity output and P_0 the intensity input in Watts. In our case, 10 mm and 1 mm samples were used to make the calculation in the case of bulk materials, whereas multiple cutbacks were made and an average of the various measurements' calculation of the chalcogenide fibers attenuation.

2.2 Refractive index

2.2.1 Michelson interferometer

The group refractive index has been measured using the Michelson interferometry technique with a Thorlabs CCS220 spectrometer from 200 nm to 1000 nm and an Avantes AvaSpec-NIR256-1.7 spectrometer from 1 µm to 1.7 µm as detectors. The white light source used in our setup (Fig. 7) is a compact broadband light source. A beam splitter redirects around 50 percent into the sample arm (static), while the other half is redirected to a movable arm. By equalizing the optical path difference (OPD) between the arm containing the additional OPD induced by the glass sample and the movable arm, we obtain interferences allowing us, for each wavelength, to calculate the group refractive index from 200 to 1700 nm to plot it (in the range of detection of our spectrometer and our light sources). The systematic error calculated for the group refractive index measurement is ± 4.10^{-4}. The phase refractive indices were determined from the Sellmeier coefficients, retrieved by fitting the first derivative of the Sellmeier equation to the measured group refractive indices as explained in chapter 3 in detail [13]. The uncertainty of the measure has been estimated to +/-0.01.

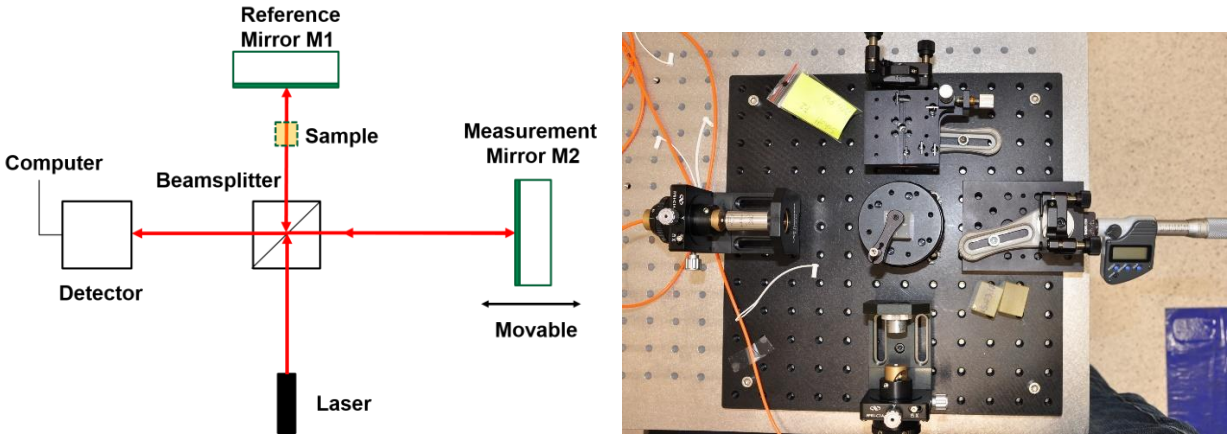

Figure 7. (left) Schematic of a typical Michelson interferometer setup, (right) Setup used for the measurements.

2.2.2 Prism coupling technique

The prism coupling technique consists of a prism topped by a slice of the sample to measure. A laser beam is refracted by the prism to either lead to a reflection at the surface of the sample to measure with detectors, if total internal reflection occurs, (due to incident angle superior to the critical angle θ_c) or lead to the beam being refracted due to its incidence angle inferior to θ_c. This allows us to measure the refractive index of the sample using the Snell-Descartes law.

For the measurement of the chalcogenides glasses presented chapter 4, a Metricon (2010) prism coupler system was used. It consists of a controller and an optical module. The optical module includes a prism, a rotation stage, pneumatic actuated coupling mechanism, 0.633 µm HeNe laser, germanium photodetector for sample measurement, silicon photodetector for establishing a rotation reference angle, and several mirrors. To study the thermal dependance of the refractive index, the prism coupler is also upgraded with thermal management systems. The optical setup layout is simplified in Figure 8, where the Metricon optical module is simplified to show the basic principle of the prism coupling technique.

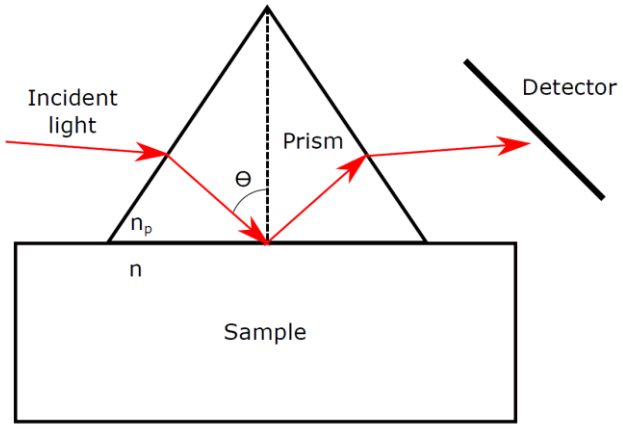

Figure 8. Schematics of the prism coupling setup for the determination of refractive index.

2.3 Dispersion

For the measurement of the dispersion such as the chalcogenides nanostructured core fibers developed in Chapter 4, we used a Mach-Zehnder setup Figure 9) comprised of a supercontinuum light source from LEUKOS, spanning from 200 nm to 2400 nm. The OPD introduced by the fiber in the signal arm is then measured as a function of the equalization wavelength from 1200 to 2400 nm, using a Yokogawa optical spectrum analyzer (OSA). The spectra are then analyzed to obtain the dispersion characteristics of the fiber as explained thoroughly in chapter 4.

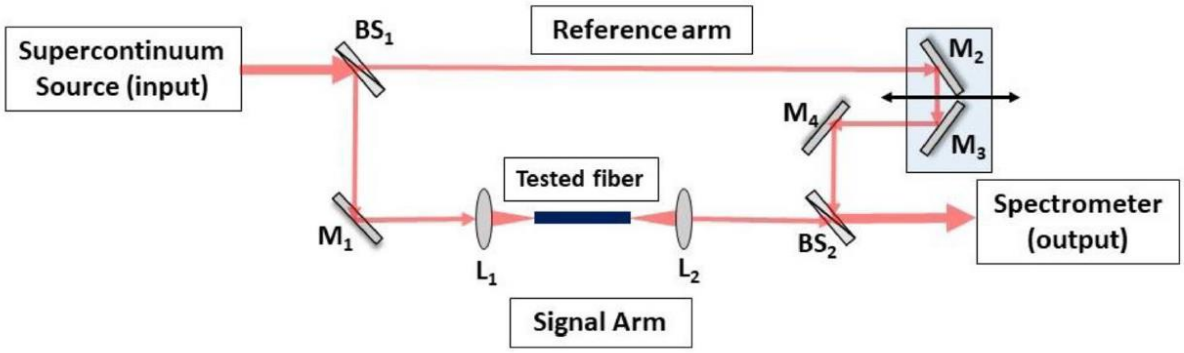

Figure 9. Mach Zenhder interferometer setup used to make the dispersion measurements. With BS: beamsplitter, M: mirror and L: lens.

2.4 Electronic Microscopy

The principle of the electronic microscopy technique relies on the detection of secondary or back-scattered electrons emitted when we shoot a sample with an electron beam produced by a heated tungsten source. The emitted electrons are focused through an electronic apparatus in a cylinder shape, made of elements allowing to control the beam under vacuum (capacitors, tracking coils and scanning devices). The primary beam, focused on the sample, induces elastic and non-elastic interactions in the material, provoking the emission of various radiation that we can exploit to study the material in various fashions (Figure 10).

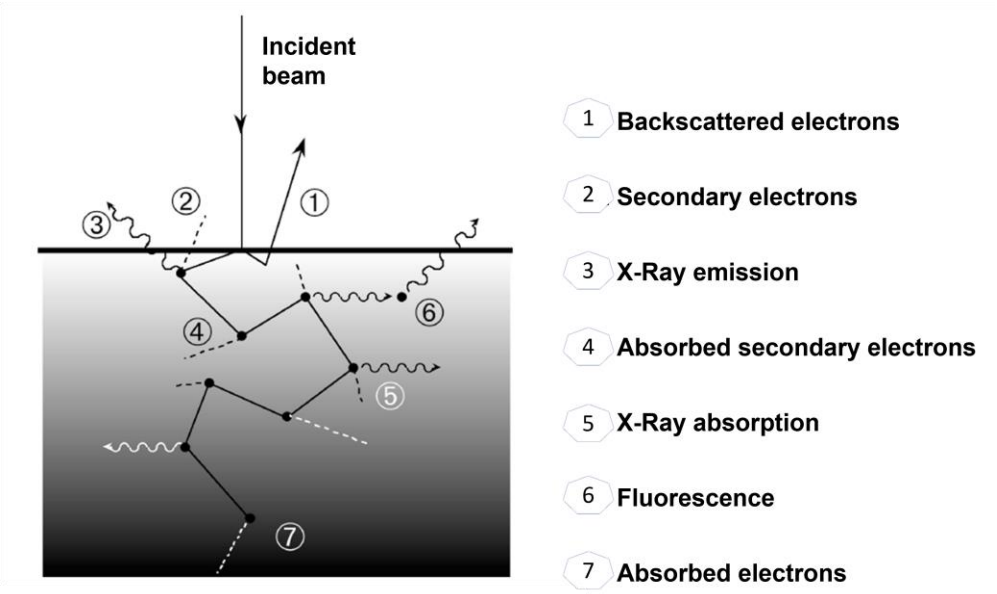

Figure 10. Schematic of the interaction of an electronic beam with matter [14].

The interaction volume in a typical material is schematized by an interaction volume representing the various interaction of an electron beam with the material for different energy and different depth. The analyzing depth depends on the nature of the material as well as the accelerating voltage of the primary electron beam used, as shown on Figure 11. The emissions produced are collected by various detectors allowing us to reconstruct an image of the surface of the sample as well as allowing us to analyze its composition. Depending on the type of electrons emitted (secondary electrons (SE), back-scattered electrons (BSE), Auger and X-photons), various contrasts can be observed. Information on the surface geometry such as the roughness can be obtained via low kinetic energy secondary electron (SE) due to their high sensitivity to the topography of the sample. Backscattered electron emission (BSE) has a high kinetic energy and a weak penetration depth. The chemical contrast offered by BSE is an advantage to determine the composition of the sample studied.

The interaction of the X-Ray emitted because of the interaction with the primary electrons with the sample allows us to analyze the chemical elements constituting the sample. Microanalysis X is generally done in two different ways: using an energy dispersive spectrometry (EDS) detector or using a wavelength dispersive spectrometry (WDS) detector. WDS Spectrometry has a higher spectral resolution as well as a better peak to background ratio compared to EDS, making it more sensitive. Indeed, the limit of detection of WDS is spanning from 10 ppm to 100 ppm for element with an atomic number $Z > 11$ when EDS only offers a resolution of 1000 nm. However, EDS allows to measure the whole spectrum in a short manner, making it complementary to WDS, despite its lower sensitivity. It also allows us to study the composition profile of the material.

Figure 11 represents the interaction sphere of the electron emitted by a sample impacted by a primary source, called interaction volume.

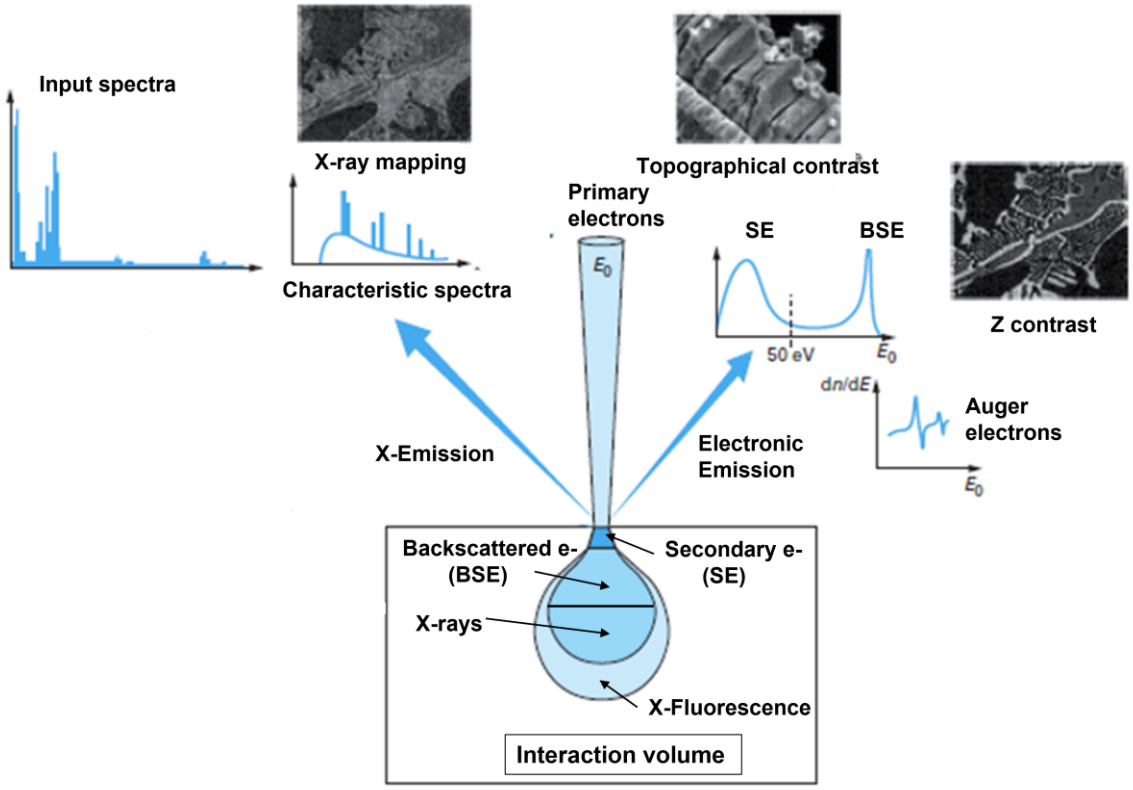

Figure 11. Interaction volume of the electron emitted by a sample shot with a primary source of electrons [15].

Conclusion

This chapter presented the basic measurements methods the most used for glasses in optics in the context of this thesis. The thermal and optical properties are of first importance to develop optical components such as lenses or optical fibers. We mostly used the basic thermal properties measurement such as dilatometry or DSC as well HSM or density measurements. The optical properties used a wide variety of methods due to the drastically different properties of the two main families studied in this thesis, chalcogenides, and oxides glasses.

References

[1] R. Stepien, R. Buczynski, D. Pysz, I. Kujawa, M. Mirkowska. “Tellurite glasses for microstructured optical fibers manufacturing”. Photonics Letters of Poland 2 (2010). 10.4302/plp.2010.1.06.

[2] R. Stepein, J. Cimek, D. Pysz, I. Kujawa, M. Klimczak, R. Buczynski, "Soft glasses for photonic crystal fibers and microstructured optical components," Opt. Eng. 53(7) pp071815 (2014). https://doi.org/10.1117/1.OE.53.7.071815

[3] I. Kujawa, R. Kasztelanic, R. Stępień, M. Klimczak, J. Cimek, A.J. Waddie, M.R. Taghizadeh, R. Buczyński, “Optimization of hot embossing method for development of soft glass microcomponents for infrared optics”, Opt. Laser Technol., volume 55, pp11-17 (2014).

[4] T. M. Monro, and H. Ebendorff-Heidepriem, *”Progress in microstructured optical fibers”.* Annu. Rev. Mater. Res, *36*, pp467-495 (2006).

[5] D. Pysz, I. Kujawa, R. Stępień, M. Klimczak, A. Filipkowski, M. Franczyk, L. Kociszewski, J. Buzniak, K. Harasny, R. Buczyński, “Stack and draw fabrication of soft glass microstructured fiber optics”, Bull. Pol. Acad. Sci. Tech. Sci., volume 62(4), pp667-682 (2014).

[6] C. Schick, *“Differential Scanning Calorimeter (dsc) with temperature-controlled furnace”,* U.S. Patent 3,263,484.

[7] B. Wunderlich. *”Thermal Analysis”*. New York: Academic Press. pp137–140 (1990).

[8] M. Pascual, A. Duran, M. Prado, ”A New Method for Determining Fixed Viscosity Points of Glasses.”, European Journal of Glass Science and Technology Part B Physics and Chemistry of Glasses. 46. pp512-520 (2005).

[9] F.M. Stábile, M. Piccico, M.F. Serra, M. Rafti, G. Súarez, N.M. Rendtorff, ”Viscosity and Thermal Evolution of Density and Wetting Angle of a Commercial Glaze by Means of Hot Stage Microscopy”, Procedia Materials Science, Volume 9, pp563-570 (2015).

[10] RJ. Seyler, ed. “*Assignment of the Glass Transition*.”, ASTM International, (1994). http://dx.doi.org/10.1520/stp1249-eb

[11] L. Yang, J. K. Thomason, ”The thermal behaviour of glass fibre investigated by thermomechanical analysis.”, *J Mater Sci* 48, pp5768–5775 (2013). https://doi.org/10.1007/s10853-013-7369-7

[12] J.E. Shelby, ”Introduction to Glass Science and Technology”, Ed. RSC (2005).

[13] P. Hlubina, “White-light spectral interferometry with the uncompensated Michelson interferometer and the group refractive index dispersion in fused silica”, Opt. Commun., volume 193, pp1-7 (2001).

[14] N. Menguy, *"Microscopies Electroniques: Interaction rayonnement-Matière"*, Institut de Minéralogie et Physique des Milieux Condensés.

[15] H. Paqueton, J. Ruste, ”Microscopie électronique à balayage - Principe et équipement”, Techniques de l'ingénieur 1080 (2006).

Chapter 3: Heavy Metal Oxide Glasses for Mid-IR optics

Heavy metal oxides glasses (HMOG) have a limited transmission in the mid-IR up to 6 µm and a refractive index ranging from 1.8 to over 2.2 but have the advantage to have a good transparency starting in the visible and good mechanical properties [1]. They offer a good compromise between optical properties, cost and are relatively easy to synthesize. Lead-gallium glass system, lacking typical glass formers, exhibits a low thermal stability. Previous studies have shown that the introduction of SiO_2 in lead-gallium glasses increases the crystallization resistance, due to the stabilizing role of [SiO_4] tetrahedra in the glass network, while keeping the transmission over 4.5 µm [2]. In addition, gallium oxide dramatically improves the thermal stability of heavy metal oxides glasses against devitrification [3]. Incorporating Ga_2O_3 into glass compositions additionally increases the linear and nonlinear index of refraction [4-7]. Lead oxide is known to increase the refractive index due to its high optical density and large molecular weight. It also decreases the viscosity and the characteristic temperature due to the creation of non-bridging oxygen in silicate glasses, below 30% content. Above 30%, PbO starts to act as a glass former and enter the glass network with PbO_x polyhedron, further decreasing the transition temperature [8-9]. Such multicomponent system allows to easily tune the thermomechanical and optical properties by modifying the concentration of the components [10-12]. One of the most studied HMOG last few decades are tellurites glasses due to their high nonlinearity and their overall good chemical durability as well as a good transparency window ranging from visible up to 6 µm, with a nonlinearity 100 times larger than silica glass. Classic tellurite PCFs are usually produced by the extrusion method due to their limited stability and present important absorption peaks from 3 µm to 4.2 µm due to water, limiting their transmission for meter long fibers, which is crucial for SCG.

The goal of the present chapter is to develop glasses with the appropriate rheological properties for the fabrication of optical elements such as micro-lenses and fiber optics with high transmittance in mid-infrared. We have chosen to study two types of glasses: HMOG with silica and tellurite glasses. In the first part, we synthetized for the first time the glass system containing SiO_2-PbO-CdO-Ga_2O_3 (named SPCG) that was not considered before. In this aim, we studied in the proposed SiO_2-PbO-CdO-Ga_2O_3 system, the impact of the substitution of silica by gallium oxide on the thermal and optical properties for different lead oxide and cadmium oxide contents. We considered the most stable glasses against crystallization for the fabrication of optical fibers by the stack and draw method as well as lenses by the hot embossing method. In a second time, we considered a well-known tellurite glass, TZN, within the TeO_2-ZnO-Na_2O glass system, to extend its transmission to 5.5 µm using halides compounds and various other dehydrating techniques. We synthetized TZN glass modified with fluorides and chlorides in a glove box to decrease the water content and then tried to produce preforms to produce optical fibers by the stack and draw method.

1. Heavy metal oxides glasses with silica

1.1 Synthesis

1.1.1 Glass compositions

Various glass compositions were investigated into the SiO_2-PbO-CdO-ZnO-Ga_2O_3 glass system (SPCZG) first. The composition synthetized can be found Table 1.

Table 1. Compositions of SPCZG glasses synthetized in mol%.

Glass composition	SiO_2	PbO	CdO	ZnO	Ga_2O_3
SPCZG0	35	40	20	5	0
SPCZG1	32	40	20	5	3
SPCZG2	29	40	20	5	6

For the first composition, named SPCZG0, we could observe long filaments in the bulk glass attributed to two glass phases competing, leading to phase separation. For the second composition, named SPCZG1, we decided to introduce gallium oxide, known to increase the thermal stability of glasses.

Despite the change of composition, we could still observe phase separation and even some undissolved particles in the melt glass. We went further into substituting silica oxide with gallium oxide with SPCZG2 but both glasses, SPCZG1 and SPCZG2, ultimately crystallized after the quenching, showing a low thermal stability of those compositions, which is why we decided to get rid of ZnO, and decided to investigate SiO_2-PbO-CdO-Ga_2O_3 glass system. The compositions can be found in Table 2.

Table 2: Chemical composition (in mol%) of SPCG B, C and D series of glasses.

Composition of SPCG glasses (mol%)																		
Oxide	(40-x)SiO_2-40PbO-20CdO-xGa_2O_3						(40-x)SiO_2-45PbO-15CdO-xGa_2O_3						(40-x)SiO_2-35PbO-25CdO-xGa_2O_3					
	0B	1B	2B	3B	4B	5B	0C	1C	2C	3C	4C	5C	0D	1D	2D	3D	4D	5D
SiO_2	40	37	34	31	28	25	40	37	34	31	28	25	40	37	34	31	28	25
PbO	40	40	40	40	40	40	45	45	45	45	45	45	35	35	35	35	35	35
CdO	20	20	20	20	20	20	15	15	15	15	15	15	25	25	25	25	25	25
Ga_2O_3	-	3	6	9	12	15	-	3	6	9	12	15	-	3	6	9	12	15

1.1.2. Batch preparation

The glasses were prepared by the conventional melt-quenching technique using analytical grade substrates SiO_2, CdO, Ga_2O_3, PbO, $Pb(NO_3)_2$ and As_2O_3 as fining agent [13]. $Pb(NO_3)_2$ is used in order to get oxidizing condition during the synthesis as well as promoting the release of gases contained in the melt by aggregation of bubbles. Indeed, $Pb(NO_3)_2$ decomposes at 470°C:

$$2\ Pb(NO_3)_2 \rightarrow 2\ PbO + 4\ NO_2 + O_2$$

Fining agents are used to obtain glasses with high optical quality. As_2O_3 is used in combination with oxidants, lead nitrate in this case, to convert As_2O_3 to As_2O_5, following the reaction:

$$As_2O_3 + O_2 \rightarrow As_2O_5$$

During the fining, at higher temperature, pentavalent arsenic will release O_2 in the melt, promoting gas removal from the molten glass, increasing the homogeneity. The substrates were weighed and ground with a mortar to obtain homogenous powder followed by drying at 150°C for twelve hours, to evacuate

the free water contained in the raw materials. The batch was then introduced in a platinum crucible for synthesis. The purity of the raw materials can be found in Table 3.

Table 3. Purity of the various chemicals used for glass synthesis.

Raw Material	Purity
SiO_2	99.9%
PbO	99.8%
$Pb(NO_3)_2$	99.50%
CdO	99.5%
Ga_2O_3	99.99%
As_2O_3	99.5%
ZnO	99%

1.1.3 Glass melting

Batches were melted in a platinum crucible for 2 hours in air, at a temperature ranging from 1000°C to 1100°C, depending on the composition, in a resistance furnace. Melts have been mechanically stirred several times to obtain a good homogeneity and have then been poured into a preheated graphite mold before being annealed, from 460°C to the room temperature, at a rate of 0.5°C/min. In order to investigate the influence of the composition on the properties and to develop thermally stable glasses for mid-infrared optical elements, three series of glasses have been synthesized: series D, with the general composition $(40\text{-}x)SiO_2\text{-}35PbO\text{-}25CdO\text{-}xGa_2O_3$, series B, $(40\text{-}x)SiO_2\text{-}40PbO\text{-}20CdO\text{-}xGa_2O_3$ and series C, $(40\text{-}x)SiO_2\text{-}45PbO\text{-}15CdO\text{-}xGa_2O_3$, with x=0, 3, 6, 9, 12 and 15%mol (Fig. 1).

Figure 1. SPCG B, C and D series bulk glasses.

1.2 Measurements of SiO_2-PbO-CdO-Ga_2O_3

1.2.1 Thermal properties

1.2.1.1 Differential scanning calorimetry

Glass transition temperatures T_g, as well as the crystallization onset temperature T_x, were determined by differential scanning calorimetry (DSC) using STA 449 F1 Jupiter (NETZSCH) equipped with a platinum furnace. Samples of 60 mg were heated in alumina crucibles with 10 K/min heating rate under the flow of a mixture comprising argon (72 mL/min) and oxygen (18 mL/min), in the range 30-800°C. The thermal stability of the glasses can be evaluated by the difference $\Delta T = T_x - T_g$ introduced by Dietzel [14]. A glass is stable enough for fiber drawing if ΔT is above 100°C and if it has a good crystallization resistance over a wide range of temperature. Indeed, the various heat treatments involved in the production of optical elements can lead to the devitrification of the glass.

The DSC measurement results for the 3 series of glass are presented in Figure 2. The transformation temperature T_g, crystallization onset temperature T_x and the difference $\Delta T = T_x - T_g$ are summarized in Table 4.

Table 4. Characteristic temperatures of SPCG glasses determined by DSC.

Serie B	T_g (°C)	T_x (°C)	$\Delta T=T_x-T_g$	**Serie C**	T_g (°C)	T_x (°C)	$\Delta T=T_x-T_g$	**Serie D**	T_g (°C)	T_x (°C)	$\Delta T=T_x-T_g$
SPCG0B	455.3	613.5	158.2	**SPCG0C**	439.5	575	135.5	**SPCG0D**	459.5	581.7	122.2
SPCG1B	454.0	691.4	237.4	**SPCG1C**	443.5	596	152.5	**SPCG1D**	467.8	613.2	145.4
SPCG2B	460.3	660.9	200.6	**SPCG2C**	451.7	649.7	198.0	**SPCG2D**	474.0	617.9	143.9
SPCG3B	465.6	670.7	205.1	**SPCG3C**	460	652.7	192.7	**SPCG3D**	478.8	619	140.2
SPCG4B	468.1	670.5	202.4	**SPCG4C**	460.8	654.2	193.4	**SPCG4D**	480.3	677.5	197.2
SPCG5B	468.0	655.3	187.3	**SPCG5C**	464.5	652	187.5	**SPCG5D**	480.8	679.2	198.4

*Accuracy of the measurement was evaluated comparing the melting point of different pure metals in the range of measurement (100 - 900°C). The accuracy is ±0.3°C due to varying heat transfer conditions such as the position of the crucible in the heating chamber, the mass of the sample and the heating rate.

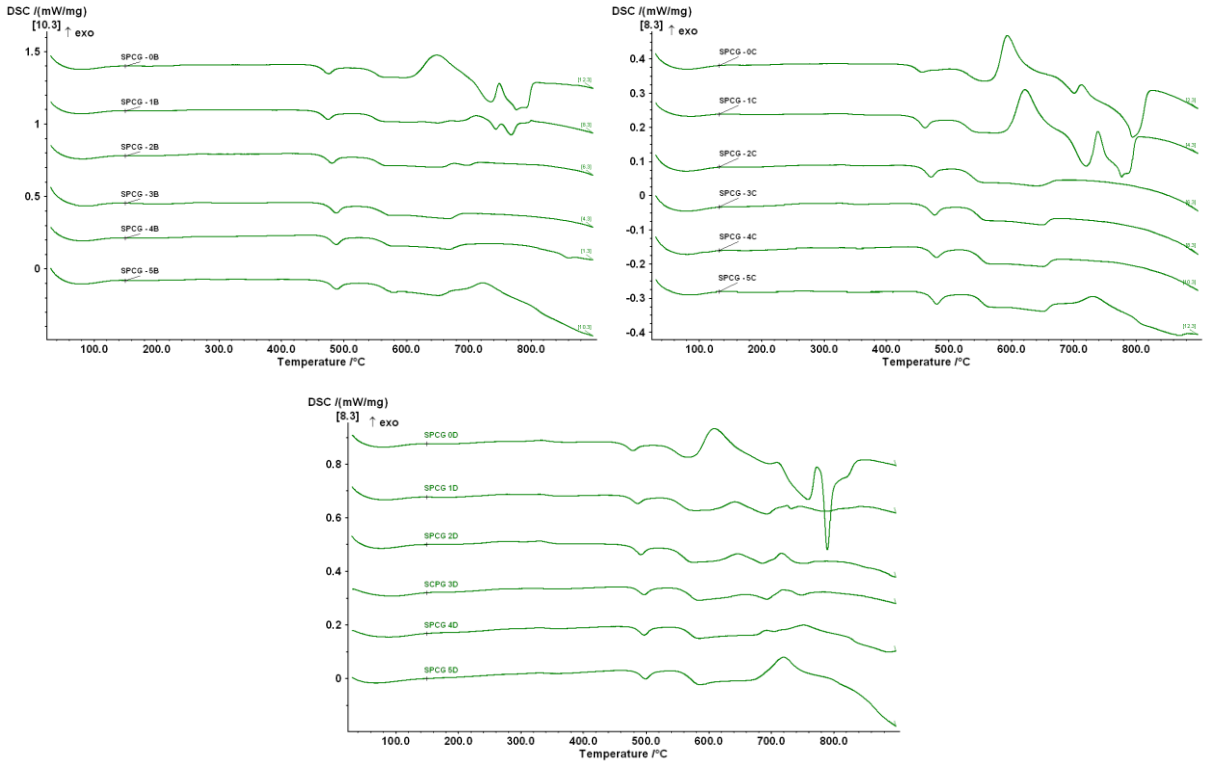

Figure 2. DSC curves for SPCG B series (left), SPCG C series (right) glasses and SPCG D series (bottom).

Glasses with 0 % and 3 % gallium in all series present multiple sharp crystallization peaks, characteristic of a high tendency to crystallize and point to the presence of multiple crystalline phases. The most stable glasses with 6 % to 15 % Ga_2O_3 are characterized by a very low intensity crystallization peak and a good nonisothermal crystallization resistance with ΔT ranging from 150 °C to 205 °C. Additional endothermal reactions of unknown nature are observed in the ΔT region. The thermal stability of all series increases with the substitution of SiO_2 with Ga_2O_3, as well as the glass transition temperature (Fig 3), ranging from 439°C to 480°C. We also observe that replacing cadmium oxide with lead oxide leads to a diminution of the characteristic temperatures. Indeed, an increase of PbO concentration instead of CdO, decreases the glass transition temperature.

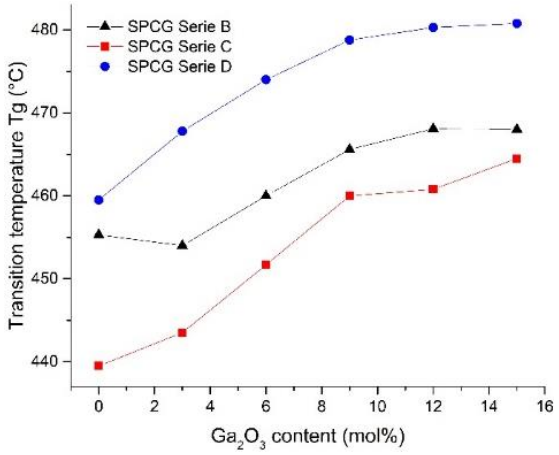

Figure 3. Evolution of the glass transition temperature with the gallium oxide content.

1.2.1.2 Dilatometry

The linear coefficients of thermal expansions along with the dilatometric softening temperatures ($\eta = 10^{11}$ P), T_{dsp}, have been determined with a Bahr Thermoanalyse GmbH Dil801 dilatometer with 5°C/min heating rate, under air (see chapter 2). The accuracy of the linear expansion coefficient is $\pm 0.03.10^{-6}$ K^{-1}, whereas the accuracy on the temperature measurement is ±1°C. Measurements were performed on rods with the dimension 4 x 4 x 30 mm. The coefficient of thermal expansion (CTE) decreases with the substitution of SiO_2 by Ga_2O_3. We can also note that it decreases when we replace CdO with PbO. The results are summarized in Table 5.

1.2.1.3 Hot stage microscopy and viscosity

The viscosities were determined by a combination of hot stage microscopy (HSM), dilatometry ($\eta = 10^{11}$ P) and differential scanning calorimetry ($\eta = 10^{13.4}$ P). Those measurement methods have been explained in chapter 2. HSM consists of a cubic sample (dimension 4 x 4 x 4 mm) heated in a furnace with a 10°C/min heating rate and observed with an objective. As explained in chapter 1, the viscosities have been determined depending on the evolution of the shape of the samples. When the corners of the cube round out, the viscosity $\eta = 10^9$ P. As the temperature increases, the sample goes from a spherical shape at T_{sph} ($\eta = 10^6$ P) to a hemispherical shape at T_{hs} ($\eta = 10^4$ P) to finally spread at lower viscosity ($\eta = 10^2$ P) [15-16]. Characteristic temperatures (T_c, T_{hs}, T_{sph}, T_{spr}) were determined by the observation of the sample shape through the objective. Several measurements were performed and show an accuracy of ±5°C.

The evolution of the temperature dependence of the viscosity is presented in Figure 3. The glasses containing 0 and 3% Ga_2O_3 concentration have shown a high tendency to devitrify, therefore, the viscosities at high temperature could not be obtained by hot stage microscopy due to the crystallization of the sample between the curvature and the sphere temperatures. Further increase of Ga_2O_3 concentration leads to a monotonic augmentation of the viscosity. Substituting PbO with CdO leads to an increase of viscosity as well. Series D (35% PbO/25% CdO) presents the highest viscosities among all series of glass whereas series C (45% PbO/15% CdO) has the lowest. The viscosity increases with an increasing Ga_2O_3 and CdO content, which is consistent with previous studies [17] showing that an increasing lead oxide molar percentage decreases the viscosity of lead silicate glasses. The measured viscosity characteristics of glasses shows that they are technologically short, which makes fabrication of fibers by the stack and draw technique delicate.

If we consider the glass processing viscosity between $\eta=10^4$ and 10^8 Poises for the production of optical elements, the working temperature range is comprised between 525°C and 615°C (Fig.4). Due to the different nature of the measurements involved, the viscosity curves, logarithmically fitted with the Levenberg-Marquardt algorithm, is added as a guide for the eyes to get the general trend of the different glass compositions.

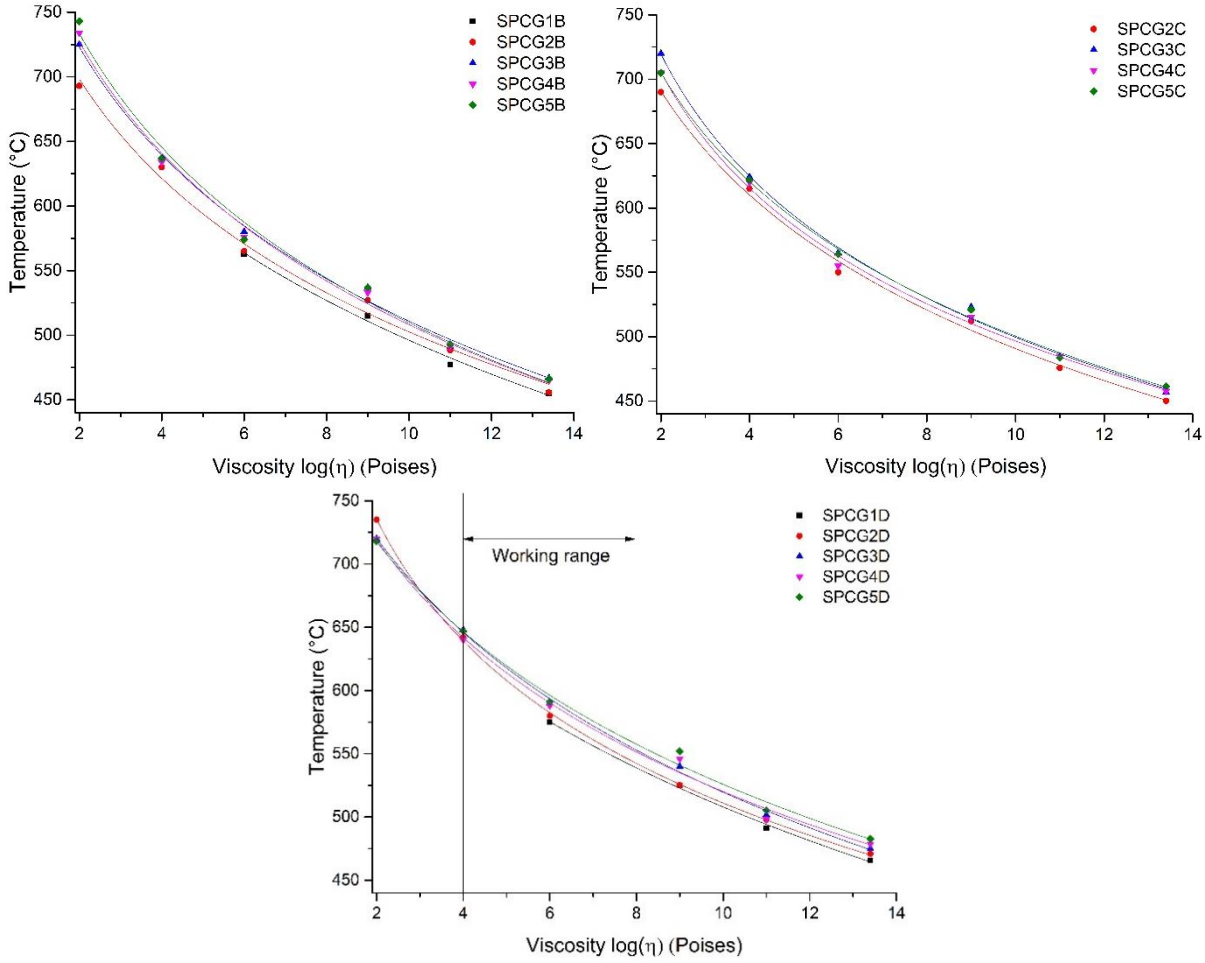

Figure 4. Viscosity-Temperature relationship of SPCG glasses for B, C and D series.

1.2.1.4 Crystallization test

Additional crystallization tests have been carried out with an isothermal heat treatment in a furnace with a dry atmosphere, 20°C higher than the sphere creation temperature T_{sph} (log η~4-5 P), for 2 hours and then cooled down to room temperature. Samples were then observed under microscope with a polarizing attachment to detect eventual crystals growth due to the heat treatment (Figure 5).

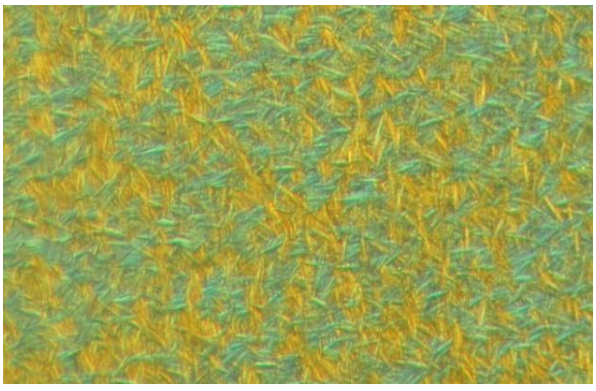

Figure 5. Example of crystallization observed in SPCG glasses (SPCG2C here), after 2 hours of heat treatment at 570 °C.

The isothermal crystallization test confirmed that SPCG 3, 4 and 5 of each series are the most suitable to make optical elements and have been selected for further tests for hot embossing and fiber drawing applications. In these cases, no crystallites were observed under the polarizing microscope after 2 hours of heat treatment at T_{sph} +20 K, in contrast with SPCG 0, 1 and 2 of each series, for which complete or partial crystallization was observed. We conclude that increasing Ga_2O_3 content with simultaneous reduction of SiO_2 leads to a large augmentation of the thermal stability of the glass, as shown in Table 4 and 5.

Table 5. Thermal properties of SPCG glasses.

Glass	CTE α_{300}^{20} ($10^{-6}K^{-1}$) ±0.03	T_{dsp} (˚C) ±1	Characteristics temperatures in Hot Stage Microscopy (˚C) ±5˚C				Cristallization
			Curvature T_c	Sphere T_s	Hemisphere T_{hs}	Spreading T_{spr}	
SPCG0B	9.15	477.8	510	Xsed	Xsed	Xsed	yes
SPCG1B	8.95	477.3	515	563	Xsed	Xsed	yes
SPCG2B	8.53	488.4	527	565	630	693	yes
SPCG3B	8.26	491.4	537	580	637	725	no
SPCG4B	8.15	491	533	576	634	734	no
SPCG5B	8.2	493	537	574	637	743	no
SPCG0C	9.06	462.4	Xsed	Xsed	Xsed	Xsed	yes
SPCG1C	8.73	466.2	500	Xsed	Xsed	Xsed	yes
SPCG2C	8.59	475.8	512	550	615	690	yes
SPCG3C	8.4	484.8	523	565	624	720	yes
SPCG4C	8.26	484.4	515	555	620	705	no
SPCG5C	8.42	483.6	521	564	622	705	no
SPCG0D	9.27	483.6	545	Xsed	Xsed	Xsed	yes
SPCG1D	8.54	491.2	525	575	Xsed	Xsed	yes
SPCG2D	8.26	497.8	530	581	642	730	yes
SPCG3D	8.18	501.7	540	590	648	720	no
SPCG4D	8.51	498.3	546	588	640	720	no
SPCG5D	8.37	505.1	552	591	647	718	no

1.2.1.5 Density and molar volume

The density of the glasses has been determined at room temperature by the conventional Archimedes method, using distilled water as immersion liquid, at room temperature.

From the density and the average molar weight of the glass, the molar volume has been calculated using the following formula:

$$V_m = \sum_{i=1}^{n} x_i . M_i/\rho \quad (cm^3.mol^{-1})$$

where x_i is the molar fraction and M_i is the molecular weight of the i^{th} component and ρ the glass density in g.cm^{-3}.

The density increases with the increase of gallium oxide content (Table 6 and Figure 6a). This is related to the substitution of lighter atoms of Si with heavier atoms of Ga in the network which leads to an increase in the average molecular weight of the glass. The density anomaly observed at 9% content of Ga_2O_3 disappears if we calculate the molar volume. Indeed, the molar volume is more sensitive to structural changes than is density because it is normalized for atomic weights of different glass components. We observe an augmentation of the molar volume with an increasing Ga_2O_3 molar percentage (Figure 6b). In general, density and molar volume vary in opposite way, this atypical behavior between density and molar volume has been previously reported also for other glass systems [18-19]. In the present case, this may be attributed to the molecular weight of the glass increasing more rapidly than the density. The density of series B is much higher than the two other series leading to the lowest molar volume among the three series, which may point to a structural change at 40% PbO.

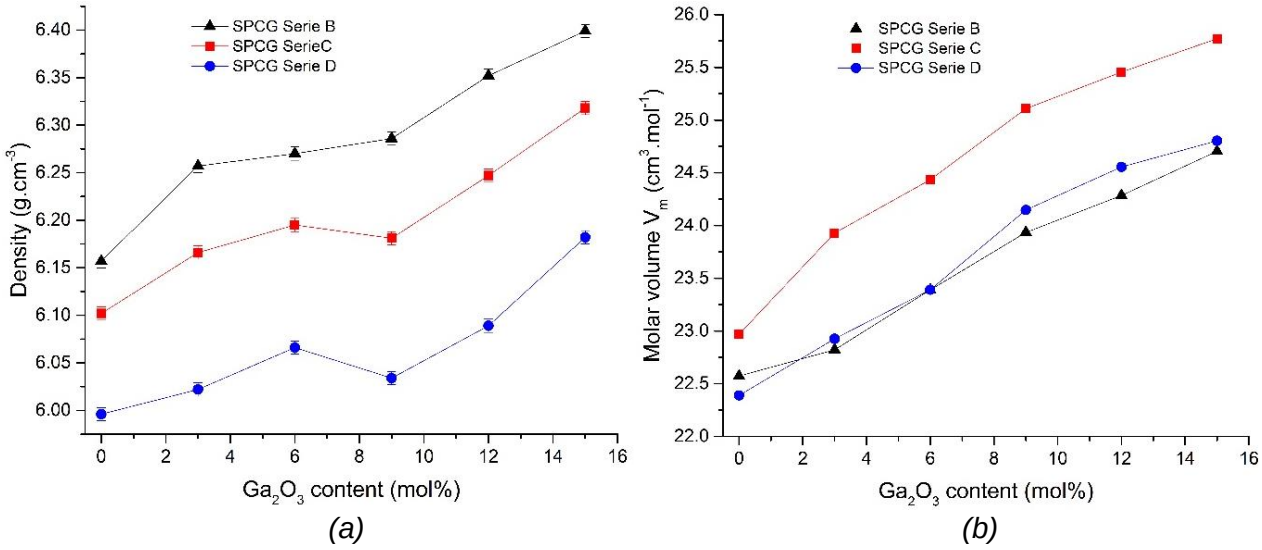

Figure 6. Evolution of the density (a) and molar volume (b) of SPCG glasses with Ga_2O_3 content.

Table 6. Density and molar volume of SPCG glass series.

Glass	Density ρ (g/cm^3) ±0.007	Molar Volume (cm^3/mol) ±7.10-4
SPCG0B	6.157	22.573
SPCG1B	6.257	22.822
SPCG2B	6.27	23.389
SPCG3B	6.286	23.934
SPCG4B	6.352	24.285
SPCG5B	6.399	24.705
SPCG0C	6.141	22.969
SPCG1C	6.166	23.929
SPCG2C	6.195	24.435
SPCG3C	6.181	25.108
SPCG4C	6.247	25.455
SPCG5C	6.318	25.771
SPCG0D	5.996	22.389
SPCG1D	6.022	22.926
SPCG2D	6.066	23.391
SPCG3D	6.034	24.147
SPCG4D	6.089	24.556
SPCG5D	6.182	24.804

1.2.2 Optical properties

1.2.2.1 Transmission

Glass transmittance measurements have been conducted with a spectrophotometer Bruker IFS 113V from 2 µm to 6 µm with 2 mm thickness polished samples. The transmission measurements are presented in Figure 7. All series of developed glasses show a broad spectral window in the mid-infrared, up to 5.0 µm. Increasing the gallium oxide content leads to shifting the multiphonon edge towards longer wavelengths, whereas the substitution of lead oxide by cadmium oxide let the transmission in infrared almost unchanged. The intensity of the characteristic absorption peaks related to the presence of hydroxyl ions OH^-, as well as the transmission cut-off wavelength, increase with the gallium content. We also noticed that the absorption peak intensity around 3 µm decreases with the substitution of PbO with CdO. This shows that lead oxide tends to retain more water than cadmium oxide. The strong water absorption is

mostly due to the synthesis without protective atmosphere as well as the water contained in the initial components.

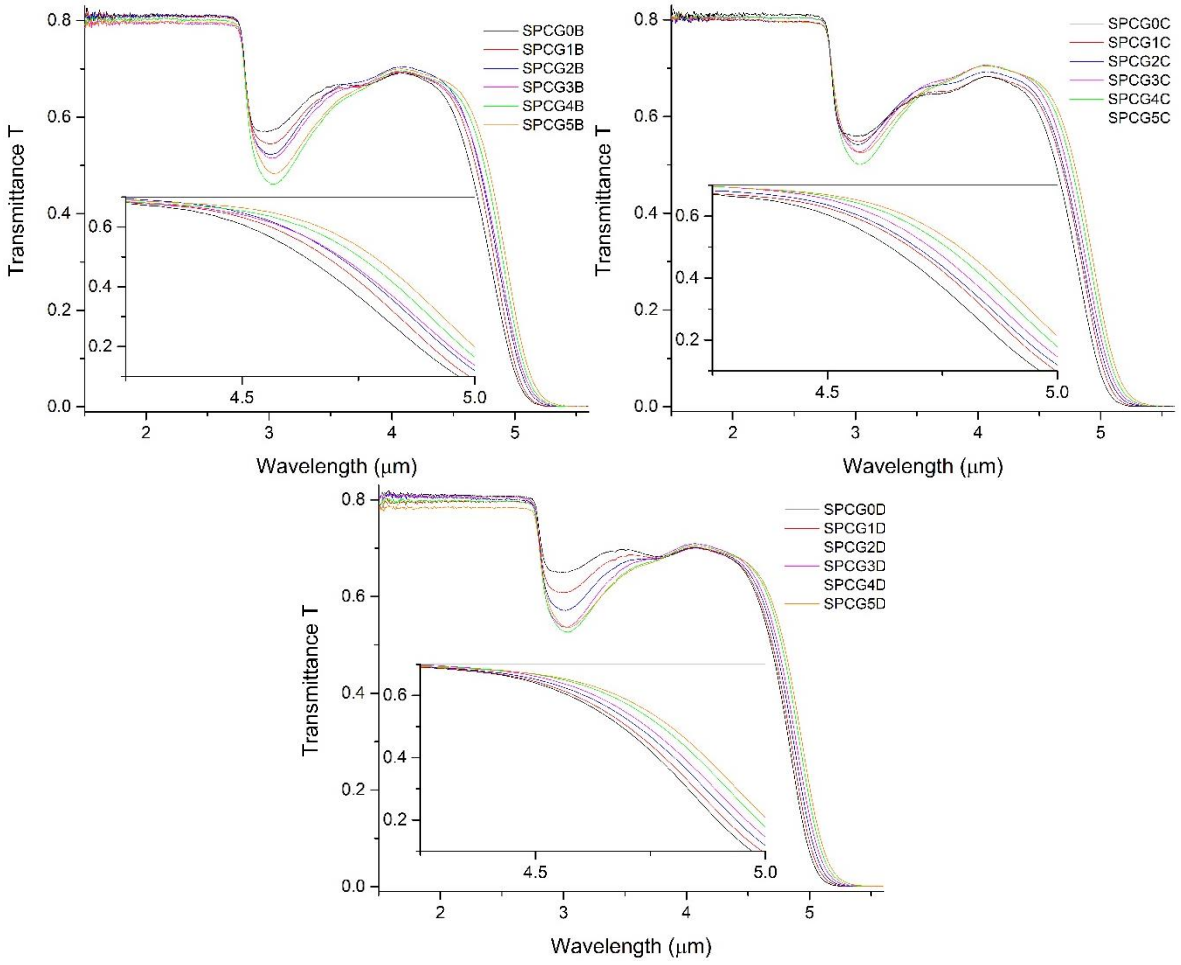

Figure 7. Transmittance of SPCG glasses in the range 2 to 6 µm.

1.2.2.2 Refractive index and dispersion

As explained in chapter 2, the group refractive index has been measured from 200 nm to 1.7 µm using the Michelson interferometry technique. The systematic error calculated for the group refractive index measurements is ± 4.10^{-4}. The phase refractive indices (2) were determined from the Sellmeier coefficients (Annex 1), retrieved by fitting the first derivative of the Sellmeier equation (3) to the measured group refractive indices [20].

$$n(\lambda) = \sqrt{1 + \frac{B_1\lambda^2}{\lambda^2 - C_1} + \frac{B_2\lambda^2}{\lambda^2 - C_2} + \frac{B_3\lambda^2}{\lambda^2 - C_3}}$$

Where n is the phase refractive index at wavelength λ in µm, B_1, B_2, B_3 and C_1, C_2, C_3 are constants determined by the fitting process.

$$N(\lambda) = \mathrm{n}(\lambda) - \lambda.\frac{dn(\lambda)}{d\lambda} = n(\lambda) + \frac{\lambda^2}{n(\lambda)}.\sum_{i=1}^{n}\frac{B_i.C_i}{(\lambda^2 - C_i)^2}$$

where N(λ) is the group refractive index, n(λ) the phase refractive index, λ the wavelength in µm, B_i and C_i are constants determined by the fitting process.

From the refractive index n at a chosen wavelength, we can estimate the Fresnel losses such as:

$$R_L = \frac{(n-1)^2}{(n+1)^2}$$

For isotropic materials such as glasses, the molar refractivity R_m (cm^3), corresponding to the average polarizability of a mole of glass, was calculated using the Volf and Lorentz-Lorenz formula ignoring the temperature and pressure impact such as:

$$R_m = \frac{(n^2-1)}{(n^2+2)} \times V_m \quad (cm^3) \quad with\, V_m = \frac{M_t}{d}$$

with n, the refractive index at the considered wavelength, V_m the molar volume of the glass, M_t defined as the total molar mass and d the density of the glass.

The molar electronic polarizability, α_m, can be calculated introducing the Avogadro number such as:

$$\alpha_m = \left(\frac{3}{4\pi N_a}\right) \times R_m \qquad (\text{Å}^3)$$

with N_a the Avogadro number and R_m the molar refractivity.

According to Duffy [21], we can estimate the energy gap E_{opt} such as:

$$E_{opt} = 20 \times (1 - \frac{R_m}{V_m})^2 \qquad (Ev)$$

The optical dispersion of the glasses has been evaluated from their respective Abbe V-number calculated from:

$$v_D = \frac{n_D - 1}{n_F - n_C}$$

with n_D, n_F, and n_C respectively the indices of refraction for the sodium D line (589.3 nm), the hydrogen F line (486.1 nm) and the hydrogen C line (656.3 nm).

The material dispersion of the bulk glasses has then been calculated from the second derivative of the Sellmeier equation such as:

$$D(\lambda) = -\frac{\lambda}{c}.\frac{dn^2}{d^2\lambda}$$

The refractive indices have been calculated from the group refractive index, measured with a Michelson interferometer from 500 to 1700 nm. The sodium D line (589.3 nm) has been used to compare the glasses and are ranging from 1.940 to 1.998 among the three series. The substitution of silica by gallium, as well as an increasing lead oxide content, lead to an augmentation of the refractive index and logically increases the molar refractivity considering the molar volume follows the same trend due to the reasons mentioned in section 1.2.1.5. As shown in Figure 8, the highest refractive index is obtained for Series C with 45 %mol PbO (n_D=1.998) and the lowest for series D with 35 %mol PbO (n_D=1.940). The material dispersion D, calculated from the second derivative of the Sellmeier equation, follows the exact same trend (Figure 9). The evolution of the phase refractive index, Fresnel losses, the molar refractivity, the energy gap as well as the reciprocal relative dispersion, and Abbe V-numbers, with the composition is summarized in Table 7. The optical dispersion is high for all glasses and increases with the gallium percentage.

Table 7. refractive index at 589.3 nm, Fresnel losses R_L, molar refractivity R_m, the electronic polarizability α_m, optical energy gap E_{opt} and Abbe number for SPCG glasses.

Glass	n	R_L	R_m	α_m	E_{opt}	V
SPCG0B	-	-	-	-	-	-
SPCG1B	1.945	0.1030	10.9829	4.3583	5.3822	20
SPCG2B	1.957	0.1047	11.3532	4.5052	5.2961	18.5
SPCG3B	1.975	0.1074	11.7655	4.6688	5.1698	19.7
SPCG4B	1.982	0.1084	11.9957	4.7602	5.1216	19.4
SPCG5B	1.991	0.1098	12.2781	4.8723	5.0604	18.6
SPCG0C	1.965	0.1059	11.2126	4.4494	5.2396	20.5
SPCG1C	1.97	0.1067	11.7222	4.6517	5.2046	19.6
SPCG2C	-	-	-	-	-	-
SPCG3C	1.98	0.1081	12.3852	4.9148	5.1354	19.1
SPCG4C	1.992	0.1099	12.6594	5.0236	5.0537	18.6
SPCG5C	1.998	0.1108	12.8683	5.1065	5.0134	17.8
SPCG0D	1.94	0.1022	10.7353	4.2601	5.4186	21.4
SPCG1D	1.944	0.1028	11.0249	4.3750	5.3895	21.2
SPCG2D	1.948	0.1034	11.2811	4.4766	5.3606	20.4
SPCG3D	1.956	0.1046	11.7128	4.6479	5.3032	20.2
SPCG4D	1.97	0.1067	12.0293	4.7735	5.2046	19.5
SPCG5D	1.98	0.1081	12.2353	4.8553	5.1354	19.3

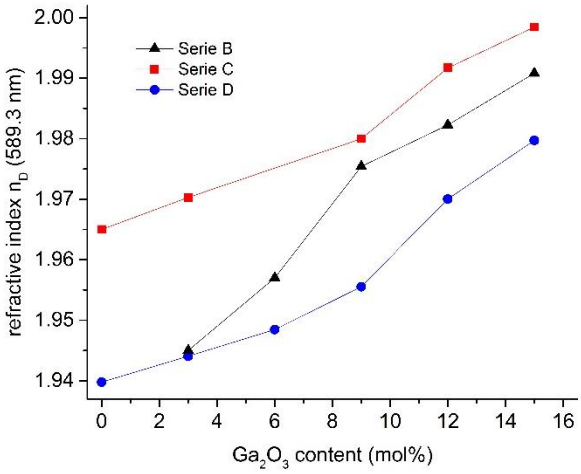

Figure 8. Evolution of the refractive index at 589.3 nm as a function of Ga_2O_3 content.

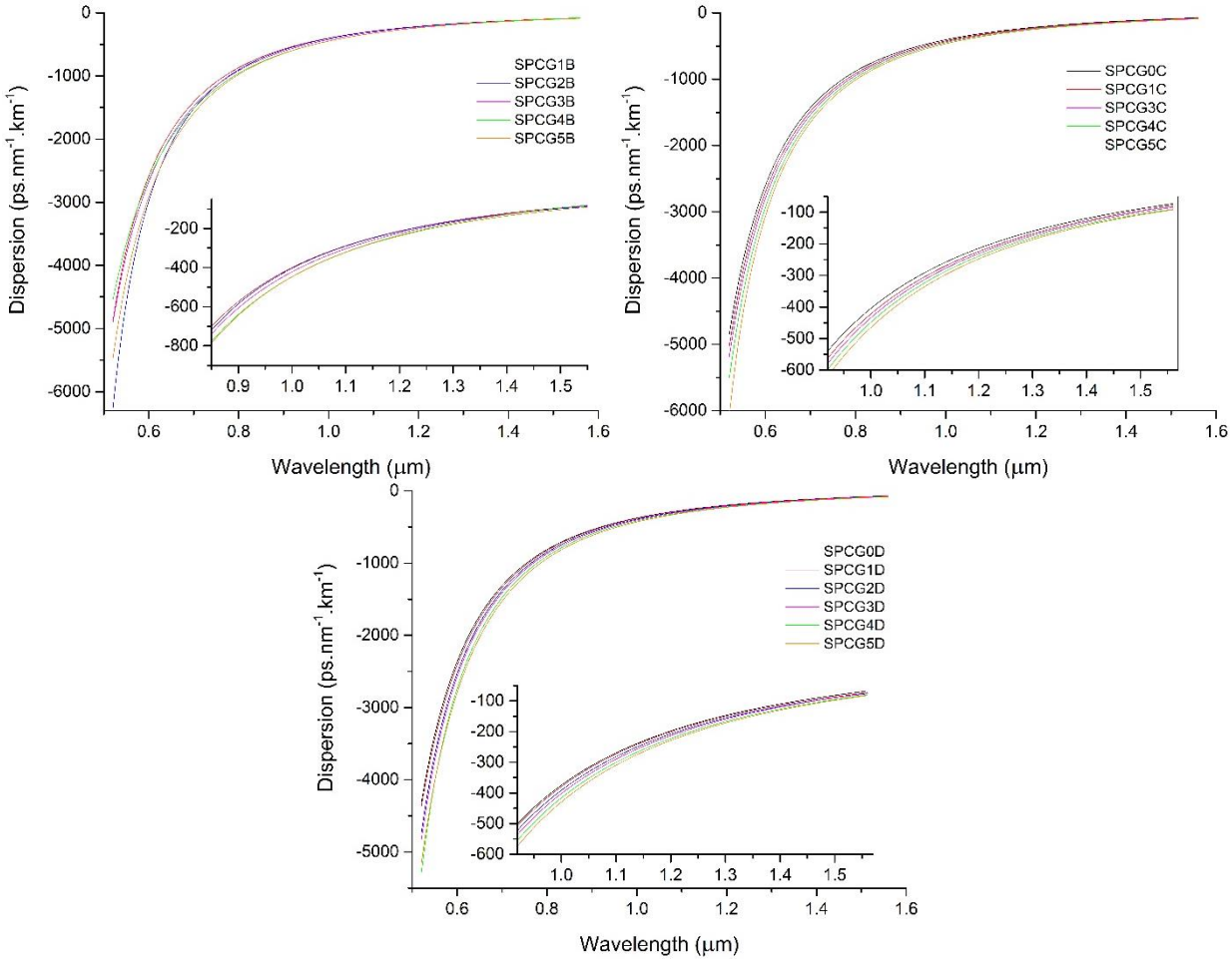

Figure 9. Dispersion parameter D as function of the wavelength for the 3 series of glasses.

1.3 Development of lenses by the hot embossing method

1.3.1 Hot embossing method

Hot-embossing process presents the advantage to be one of the lowest-cost methods for the fabrication of optical elements. It consists of an upper and lower stamp heated to the desired temperature [22], as shown on Figure 10b. When the optimal temperature of the glass is attained, the desired shape is finally transferred by pressure of the molding stamps before being cooled (Fig. 10a and 10b). One of the most important steps to make lenses by the hot embossing technique is the choice of the mold material. Indeed, the coefficient of thermal expansion (CTE) of the glass must match the chosen mold to avoid cracking during the process. In addition, the glass must not adhere to the mold and must be crystallization resistant. We have selected brass and cemented carbide for their very close CTE. These materials were successfully used as molds for hot embossing with heavy metal oxide glasses previously [23].

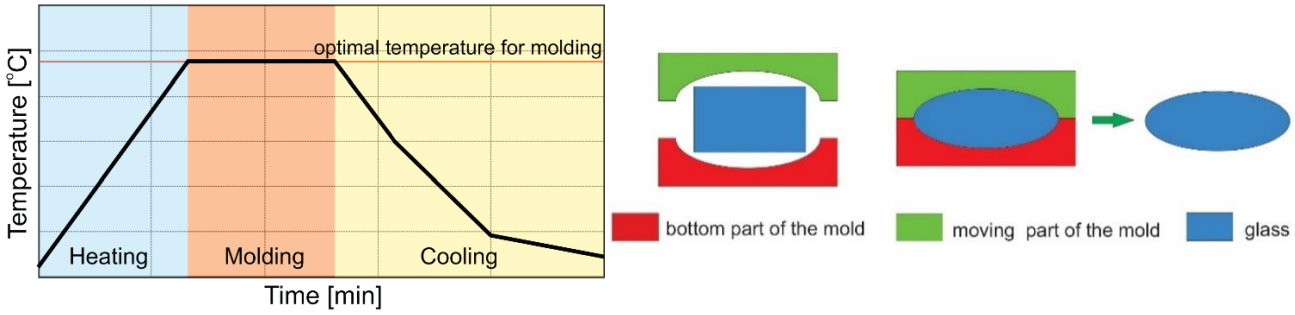

Figure 10. Different phases involved in the hot embossing technique; (b) schematic of the molding process.

1.3.2 Production of the lenses

We have selected the glasses with the largest ΔT criterion (SPCG 3, 4, 5 of each series) which resisted to the isothermal crystallization test (according to section 1.2.1.4) and have conducted preliminary embossing tests. SPCG4C glass was synthetized at increased volume without any changes of the optical and thermal properties which proves a good repeatability of the experiments. Different molding parameters have been tested until the obtention of a lens. Such parameters, besides the choice of the mold, are the molding temperature, the force applied and the molding duration. Based on the quality of the lens and the eventual presence of cracks or irregularities of the surface of the different lenses developed from the three series, we have finally chosen SPCG4C glass for its good thermal stability and its capacity to form good quality lenses. Indeed, other glasses could not be molded properly or showed cracks. The optimal parameters used for this composition were a temperature of 602°C, the pressure force of the piston was 194 N for a duration of 10 seconds.

1.3.3 Characterization

The quality of the lens has been evaluated with a white light interferometer Veeco Wyko NT2000. The images of the surfaces are shown in Figure 11a and 11b. Figure 11c shows the profile of the center of the surface of the lens of the convex side, whereas Figure 11d shows the flat side of the lens. The curvature of the lens is too pronounced to measure beyond the central part of the lens using a white light interferometer. The average roughness calculated from the profile is around 0.05 µm for the spherical surface whereas the roughness of the flat surface is 0.09 µm which is acceptable for applications in the mid-infrared. The standard error of this measurement SE=0.02 µm.

The focal length of the lens has been determined using a fiber coupled laser source from Thorlabs at 1550 nm with a power set at 0.05 mW and an infrared camera. The focus in our experiment is at a distance of 15.2 mm from the last surface of the lens. The back focal length, BFL = 11.71 mm which allows to state that the effective focal length, EFL = 11.72 mm. Errors in the horizontal and vertical direction are ±1 µm, and ±0.5 µm respectively (Figure. 12).

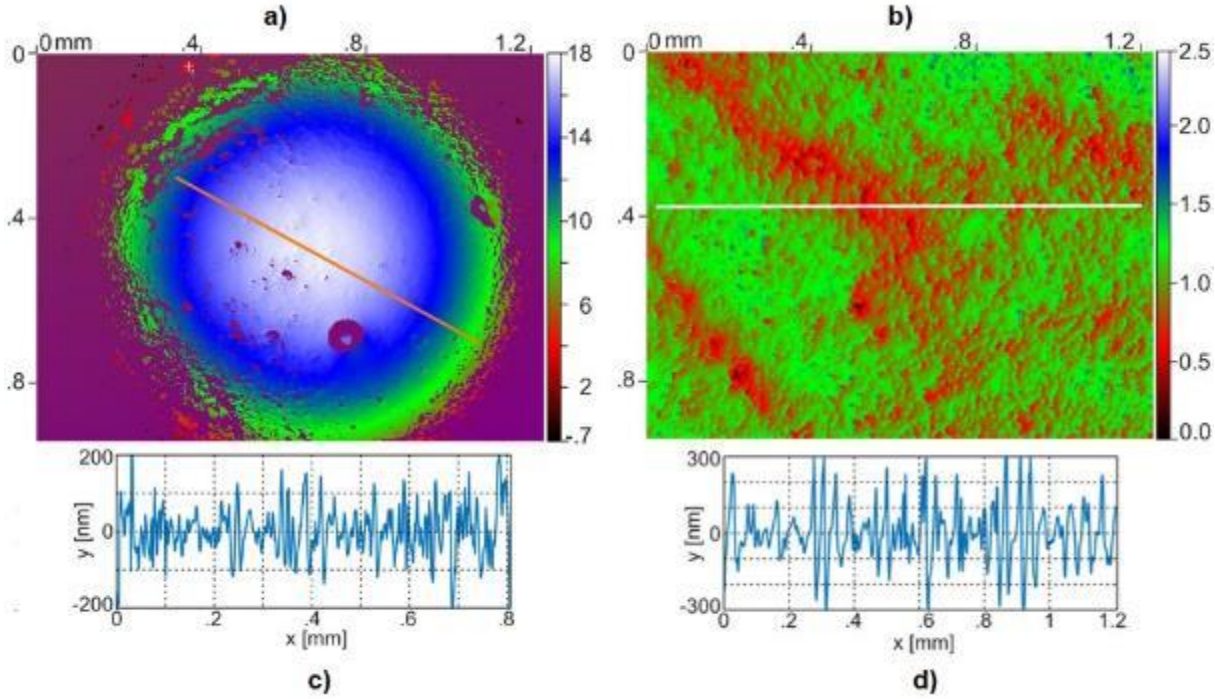

Figure 11. Surface quality measurements of the developed lens obtained using a white light interferometry method. a) and b) are respectively the scan of the spherical surface and of the flat side of the lens, while c) and d) are the respective surface roughness profiles along the line represented on the scans.

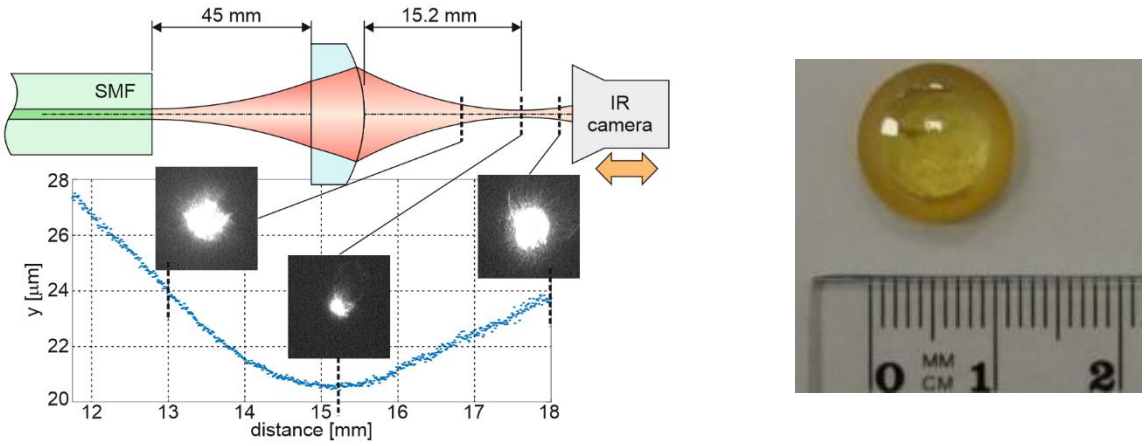

Figure 12. (left) Experimental setup for the measurement of the effective focal length of the lens, (right) fabricated lens based on SPCG4C glass.

We also verified the possibility to use the selected glass (SPCG4C) for the development of optical fibers by a classic fiber drawing technique considering its high thermal stability. The preform is fed into a furnace that heats it up to decrease its viscosity, in order to be drawn. Glass fiber is pulled by capstan while the preform is constantly fed into the furnace with constant speed. During the drawing process, fiber is coated by polymer (acrylate) which is UV cured. For this purpose, we first prepared a rod with the dimension 20 x 20 x 200 mm. The rod has then been rounded and polished to make a cylindrical preform (dimension 17.8Ø x 200 mm). The fabricated optical fiber is composed of a glass core made of SPCG4C while the cladding is made of polyacrylates with a lower refractive index (1.54). The drawing parameters were set as follows: feeding speed 0.24 mm/min, drawing speed 4 – 6 m/min, temperature 540 – 550°C. Fibers with core diameter d = 125 µm and 150 µm have been drawn successfully, the overall fiber diameter with the cladding was respectively 225 µm and 250 µm respectively (Fig. 13). We have experimentally proved that this glass could be used as waveguide for future development of optical fibers.

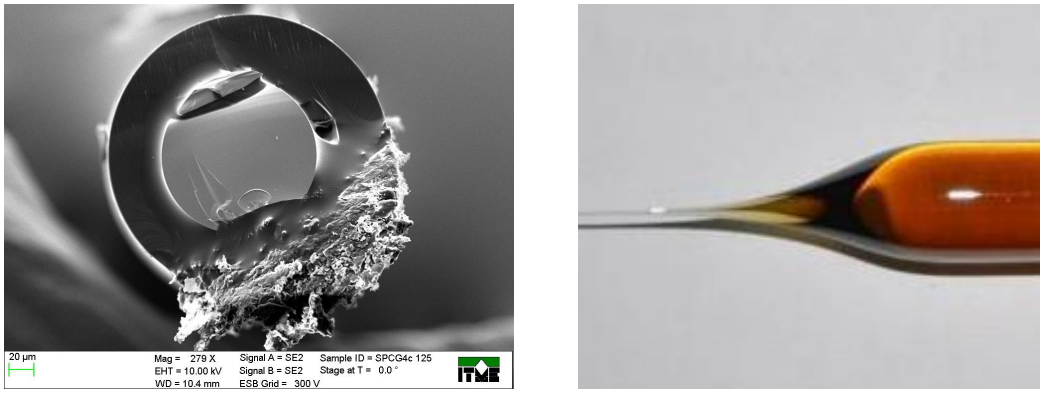

Figure 13. (Left) SEM photo of the fiber made of 125 µm SPCG4C glass core and the polyacrylate cladding. (Right) end of preform of the glass core used to develop the fiber.

2 Low OH tellurite glasses for mid-infrared applications

To extend the transmission capabilities of optical elements based on heavy metal oxides (HMO) with silica glasses as presented in the first part, another sub-family of HMO glasses, tellurites, was investigated. Indeed, they are known to have a larger linear and nonlinear refractive index while the possibility to transmit up to 5.5 µm is unachievable with silica-based HMO glasses. However, the transmission is generally limited to 3.2 µm for long length optical fibers due to the attenuation induced by the presence of impurities inside the glass network. Typically, for oxide glasses, the absorption bands of interest are due to the presence of water introduced in the batch. For this reason, we investigated the possibility to purify tellurites glasses via various means explained in the next section to increase the transmission of such fiber up to 5.5 µm by dehydrating the glass, thus, eliminating the absorption bands due to water and hydroxyl groups contained in the glass network. For this reason, we investigated the use of fluorides and chlorides solid compounds in order to dehydrate our glass as well as used a glove box with a protected atmosphere to limit the water content of the produced material.

2.1 Methods of purification of tellurite glasses

Water contained in the atmosphere as well as in the raw material is detrimental to the transmission and attenuation characteristics of tellurites glasses, limiting applications beyond 3 µm. Water hydrolyses the glass network following the reaction [24-25]:

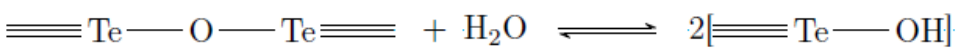

Zhmyreva et al. demonstrated this process by replacing hydrogen atoms from hydroxyl groups with deuterium (D) atoms for glasses into the composition 80 TeO_2-20 Na_2O [26]. They have achieved this by wading heavy water into the glass melt during their synthesis. Consequently, the absorption bands, normally attributed to hydroxyl groups OH were shifted to lower frequency. Indeed, deuterium having a higher atomic mass than hydrogen, the vibration modes of OD have resonance frequency lower than the modes associated with OH groups. This isotope substitution has shown that the absorption bands observed between 3 and 4 µm were, indeed, due to the presence of OH groups into the glass network. It can clearly be observed on a classical transmission or absorption spectra of a typical TZN glasses synthetized in presence of water. Due to the variety of units composing the glass network, such as [TeO_4] and [TeO_{3+1}] and [TeO_3] units making the network and taking into consideration that the flexibility of the network compared to silica glass is much more important, the variety of the absorption bands is complex making the absorption wider compared to silica and difficult to solve [27]. To simplify, we can consider that there are three large absorption bands (made of a multitude of other bands in reality): a large band due to strongly bonded hydroxyl group OH around 2260 cm^{-1}, a band due to weakly bonded OH group around 2920 cm^{-1} and the last one associated to the free water (H_2O) contained in the glass around 3260 cm^{-1} (Figure 14).

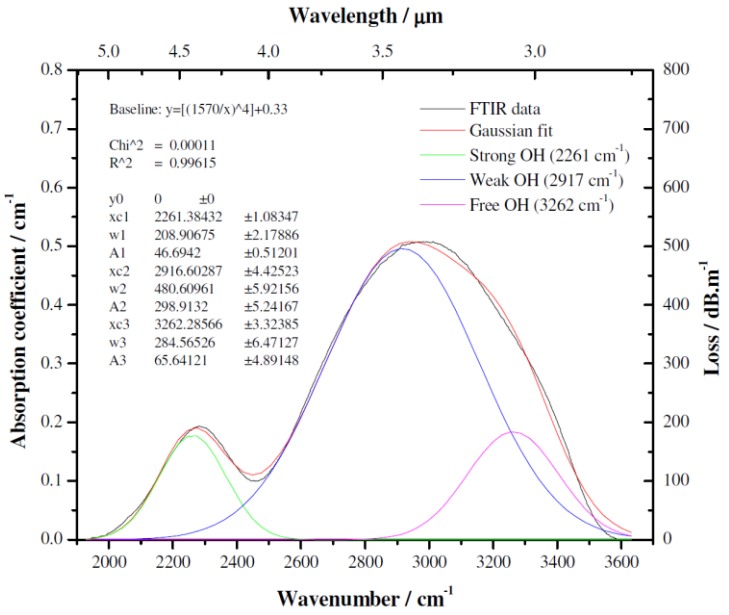

Figure 14. Example of deconvolution of the large absorption bands observed on the absorption spectra of a TZN glass.

To reduce the water content, three solutions are possible, which can eventually be combined:

• Make the synthesis under dry and oxidizing or protected atmosphere to limit the reduction of tellurium oxide and the concentration of hydroxyl groups.

• Make the synthesis using reactive atmosphere processing (RAP) such as CCl_4 or Cl_2.

• Make the synthesis using solid-state dehydrating agents. In this case, replacing part of the oxides with their chlorides or fluorides.

2.1.1 Preliminary step before the purification: pre-drying

Pre-drying of powders was performed as a first step to decrease the water content of the glass, indeed, water tends to be contained in the precursors. Drying is generally performed at around 200°C either under dry oxygen flux or under vacuum for few hours. The pre-dried powders are then introduced in the glove box for the synthesis.

2.1.2 Controlled atmosphere and Reactive Atmosphere Processing

To prevent the absorption of water in the glass melt from the atmosphere, the use of a glove box with a dry atmosphere is needed. The reduction of H_2O and hydroxyl groups OH^- content in the glass melt can be achieved bubbling extra dry O_2 containing less than 1 ppm water (by reaching the equilibrium with gaseous water in the melt). Similarly to fluoride glasses synthesis, reactive atmosphere processing (RAP) is an interesting method to dehydrate the melt [28]. Bubbling reactive gases such as chlorine (Cl_2) or carbon tetrachloride (CCl_4) leads to a decrease of the water content by reaction with the free water and hydroxyl

groups bonded to the glass network. However, the toxicity and reactivity of those gases make the synthesis delicate. The use of a reactive atmosphere will not be investigated due to the reasons mentioned above.

2.1.3 Solid-states dehydrating agent

2.1.3.1 Chloride of the metal

Chloride compounds of the metals will react with the water contained in the batch as well as with the hydroxyl groups bonded to the glass network (absorbed during melting), liberating hydrogen chloride and producing the oxides of the metal, thus, dehydrating the final product obtained in order to optimize the transmission above 3.4 µm. For tellurites-based glasses, the logical choice is $TeCl_4$. Indeed, chloride reacts with water as follow:

$$TeCl_4 + 2H_2O \rightleftharpoons TeO_2 + 4HCl$$

$$TeCl_4 + 4[\equiv Te-OH] \rightleftharpoons 2[\equiv Te-O-Te\equiv] + TeO_2 + 4HCl$$

For Na_2O and PbO containing heavy metal oxides glasses, NaCl and $PbCl_2$ might as well be used (NaCl seems much less effective though).

2.1.3.2 Fluoride of the metal

The same way, we can replace part of a metal oxide by its fluoride, which reacts with water as follow, liberating hydroxyfluoride HF gas and producing the oxide of the metal:

$$ZnF_2 + H_2O \rightleftharpoons ZnO + 2HF$$

$$2[\equiv Te-OH] + ZnF_2 \rightleftharpoons \equiv Te-O-Te\equiv + ZnO + 2HF$$

For Na_2O and PbO containing heavy metal oxides glasses, NaF and PbF_2 might as well be used.

Using chlorides and fluorides is especially effective if it is associated with a pre-drying step of precursors and the use of a dry atmosphere. However, it has the inconvenience of decreasing the crystallization resistance of the glass if the molar percentage of halides is too high in the composition, making the fiber drawing very difficult, due to the diminution of stability. Chlorides and fluorides compounds also present the disadvantage of modifying the optical properties of tellurites glasses, reducing their transmission in mid-infrared and their refractive index.

2.1.4 Synthesis condition and composition used into the TZN system

2.1.4.1 Synthesis condition

The preparation and the synthesis of 60 g samples introduced in a gold crucible were conducted in a homemade glove box (Figure 15) with a controlled atmosphere of dry air (H_2O content < 3ppm) at a

temperature ranging from 700 to 760 °C. Indeed, the use of a platinum crucible leads to a shouldering of the transmission intensity in the lower end of the spectra due to the etching of the platinum crucible which is why we have made the choice to use a gold crucible to optimize the transmission in the visible [29-30]. Tellurite glasses require the synthesis to be made under oxidizing conditions to prevent the reduction of the tellurium oxide TeO_2 into metallic tellurium.

Synthesis was done under a dry air atmosphere with a tube immersed in the melt bubbling extra dry oxygen with a water content inferior to 1 ppm. Finally, the melt was quenched in a preheated form in a second furnace, at the temperature of 250 ºC to avoid cracking due to thermal shock. The glass was then transferred to an annealing furnace close to T_g temperature overnight with a ramp down of 1 degree per minute (T_g=293 +/- 5 degrees for these compositions, decreasing slightly proportionally to the halides contents), as explained in the first section of Chapter 3. This synthesis method led to a clear glass with good optical quality.

Figure 15. Glove box used for the synthesis of tellurite glasses under a protected atmosphere.

In order to investigate the impact of the solid dehydrating agent on the water content, we investigated different compositions, replacing TeO_2 by $TeCl_4$, and ZnO by ZnF_2. Synthesis conditions were slightly changed depending on the composition. The studied compositions are summarized Table 8. $TeCl_4$ concentration of 2.5, 5, and 10 %mol were studied as well as TZN glasses with 5 and 10 %mol ZnF_2.

Table 8: Composition of the TZN glasses synthetized in mol%.

Composition	TeO_2	ZnO	Na_20	ZnF_2	$TeCl_4$
TZN	80	10	10		
TZN-F5	80	5	10	5	
TZN-F10	80		10	10	
TZN-Cl2.5	77.5	10	10		2.5
TZN-Cl5	75	10	10		5
TZN-Cl10	70	10	10		10

The measurements of the transition temperature could not be obtained due to the inherent nature of halo-tellurite glasses. Indeed, our apparatus did not allow us to use sealed platinum crucible for the measurements, making the measurement potentially damaging for the DSC equipment. Halides tend to evaporate at this temperature leading to the quick corrosion of most metals and ceramics. For this reason, we considered literature to have the thermal properties of these glasses.

2.2 Measurements of the optical properties of TZN and TZNF glasses

2.2.1 Transmission

We notice that the absorption bands intensity due to weakly bonded and free water around 3 µm decreases when we increase the concentration of dehydrating agent (Figure 16a and 16b). We also notice that at equal concentration, ZnF_2 is more efficient than $TeCl_4$. It is important to note that the synthesis with tellurium tetrachloride was much harder than with zinc fluoride. Indeed, it seemed to be much more prone to crystallization, even at temperature as high as 750°C (probably due to the formation of chlorides crystalline phases in the crucible). We also note that the synthesis involving TZNCl10 managed to massively decrease the strongly bonded hydroxyl content of the glass, located at 4.5 µm while the composition with 10% fluorides still had strongly bonded OH groups absorption as we can see on the pink curve around 4.5 µm. We can also clearly see that the chlorides absorption total band located between 3 and 3.5 µm (band made of free water and weakly bonded hydroxyl) tends to be shifted to the left with chlorides, which indicates that the absorption bands due to the weakly bonded hydroxyl groups located at 3.5 µm (as shown Figure 14) decreases more importantly with chlorides.

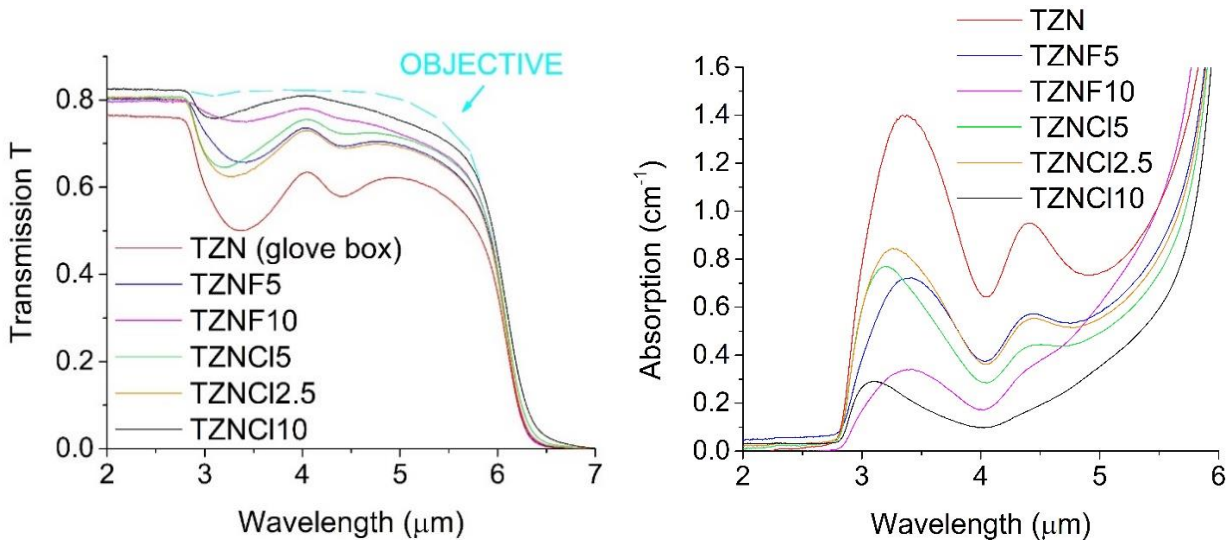

Figure 16 (left) Transmission spectra of the investigated glasses (sample thickness=2 mm). (right) absorption on bulk material in cm^{-1}.

2.2.2 Refractive index and dispersion

The refractive index and the dispersion were measured using a Michelson interferometer from 500 nm to 1700 nm. As expected, the refractive index and dispersion decrease with the amount of halide introduced in the tellurite (Table 8 and Figures 17 and 18). We can also note that this effect is more pronounced for fluoro-tellurites than chloro-tellurites as 5% of ZnF_2 achieves the same refractive index than the composition with 10% $TeCl_4$. The logical explanation is that fluor ion F^-depolymerizes the glass network more effectively than Chloride ion Cl^-. This is strongly mitigated because of the atomic mass of fluor being heavier compared to chloride, ultimately leading to a higher refractive index.

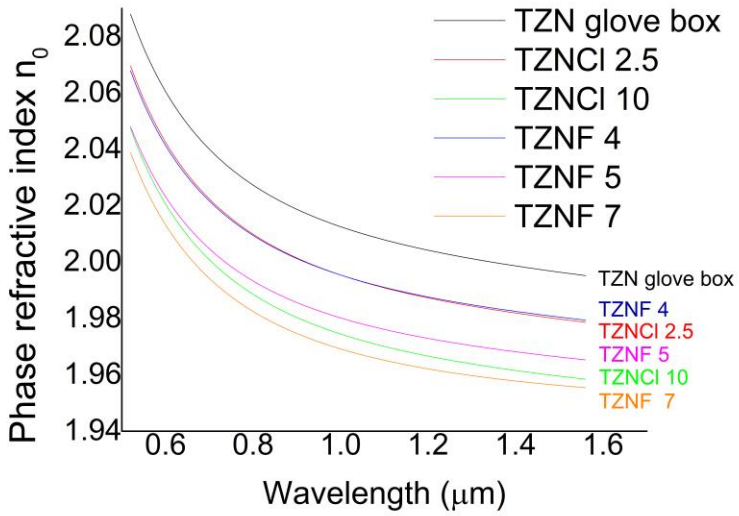

Figure 17. Phase refractive index n_0 of the TZN synthetized in various condition, from 500 to 1600 nm.

Table 8. Refractive index at 700 nm and 1550 nm for the various halo-tellurites synthetized.

Composition	n @700nm	n at 1550 nm
TZN	2.04	1.99
TZNF5	2.0	1.96
TZNCL2.5	2.02	1.98
TZNCl 10	2.0	1.96

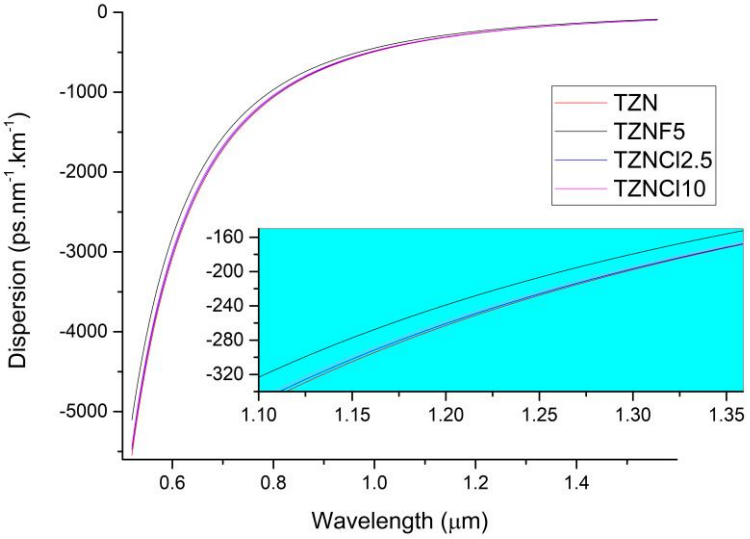

Figure 18. (a) Dispersion of TZN, TZNF and TZNCl glasses from 500 nm to 1700 nm.

2.3 Fiber drawing attempts

It has been shown that increasing the content of fluorides decreases the stability of the glass. For this reason, we have selected a composition representing a good compromise between dehydration and stability with the composition 80 TeO_2 – 6 ZnO – 10 Na_2O – 4 ZnF_2 (TZNF4), and synthetized tubes as well as rods with a 11.5cm length to draw the optical fiber rods for the future preform (Figure 19).

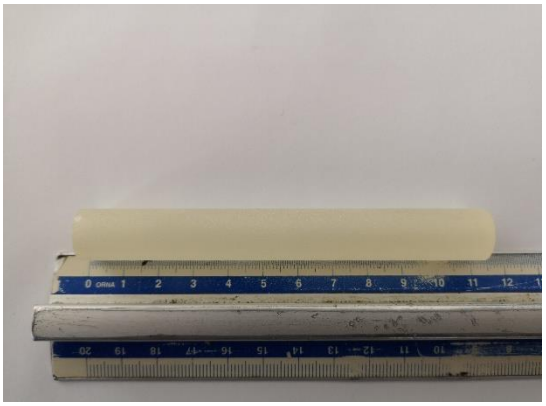

Figure 19. Rod synthetized based on TZNF4 tellurite glass for fiber drawing attempts.

We attempted to draw this glass multiple times, but some crystals could be observed at the surface. The first drawing attempt failed, due to a too high temperature. The second attempt was much better as some large parts of the rod didn't present any crystallization, but it seems clear that even if this glass can support one heat treatment, the preform would inevitably crystallize with a second one. This shows the incompatibility of the synthesis of low-water content TZN glass with the stack and draw methods involving at least two heat treatments due to the production process i.e., drawing the rods for the preform plus drawing the stacked preform to obtain the optical fiber. We see that the stability of tellurite glasses purified with fluorides compounds tends to decrease the stability of the glass due the incorporation of F^- anion in the glass network. F^- anions disrupt the Te based network breaking Te-O-Te bonds producing (TeO_3,F) or (TeO_{3+1},F) units causing a more opened structured by the creation of non-bridging oxygen [31]. It makes it more prone to crystallization due to the higher mobility of atoms in the glass network and to the strength of the F-O bond being lower than the initial Te-O—Te bonds. The structural units composing the network for alkali containing tellurites glasses are shown in Chapter 1.

Conclusion

The SiO_2-PbO-CdO-Ga_2O_3 oxides system has been studied for the first time as a candidate for crystallization resistant glass for multiple thermal processing. Increasing the gallium oxide content instead of silica tends to increase the thermal stability of the glass against devitrification (as well as increasing the refractive index and the transmission towards mid-infrared). We showed that this system is suitable for the production of optical elements such as lenses and optical fibers due to its high thermal stability. Glass with the composition 28SiO_2-45PbO-15CdO-12Ga_2O_3 has been selected to develop optical components for its high crystalization resistance and its capacity to be molded. The optimized glass has a transmission up to 5 µm with a refractive index n_D = 1.992. The glass transition temperature T_g=460.8°C and the softening temperature T_{sp} = 550°C, respectively. The thermal stability criterion ΔT=193°C.

We have successfully fabricated lens by the hot embossing technique with an average roughness comprised between 40 nm and 90 nm. As a proof of glass feasibility for fiber technology, plastic-clad glass fibers were drawn with diameters of 225 µm and 250 µm and a core diameter of 125 µm and 150 µm.

To extend the transmission bandwidth of optical elements up to 5.5 µm, we investigated purified tellurites glasses to produce photonic crystal fibers for applications in the mid infrared. For this purpose, I investigated various halides compounds to dehydrate tellurites glasses in order to extend their transmission from 3 µm to 5.5 µm. Solid-state agents have proven to be an effective way to reduce the absorption between 3 to 4.4 µm due to water, but the home-made glovebox did not allow us to achieve ultra-low attenuation for optical fibers. In a second time it was clear that fluoro-tellurites glasses could not withstand multiple thermal processes such as those involved in the production of lenses by the hot embossing method and optical fiber by the stack and draw method, both involving two heat treatments. Nevertheless, we have shown that the usage of halides compounds was effective to reduce the overall water content, even if the performance achieved is not sufficient due to the glove box apparatus and the purity of the raw materials. For further studies, I strongly suggest synthetizing in house TeO_2 to achieve high purity compounds. It is indeed costly and difficult to buy purity above 5N (99.999%) for TeO_2 and

other chemicals involved in the synthesis. The use of reactive gases such as fluorine could also be an interesting drying pre-step to take to drastically reduce the water content in tellurite glasses to extend the transmission up to 5.5 µm in meters long optical fibers. Concerning the inherent thermal instability of fluorotellurites, it seems that the extrusion method is the only way to date to produce extended transmission, low OH, tellurites optical fibers.

References

[1] B. Saisudha, T. Mallur, A. Ashish, K. Panakkattu, “Compositional dependence of optical band gap and refractive index in lead and bismuth borate glasses.”, Mater. Res. Bull., volume 68, pp27 (2015).

[2] A. Marczewska, M. Środa, M. Nocuń, B. Sulikowski, “Lead-gallium glasses and glass–ceramics doped with SiO_2 for near infrared transmittance.”, Opt. Mater., volume 45, p121-130 (2015).

[3] J.C. Lapp and W.H. Dumbaugh, “Gallium Oxide Glasses.”, Key Engineering Materials, volume 94-95, pp257-278, (1994).

[4] W.H. Dumbaugh and J.C. Lapp, “Heavy-Metal Oxide Glasses.”, J. Am. Ceram. Soc., volume 75, pp2315-2326 (1992).

[5] J. E. Shelby, “Lead Gallate Glasses.”, J. Am. Ceram. Soc., volume 71, pp254-256 (1988).

[6] H. Fan, G. Wang, L. Hu, “The Thermal and Optical Properties of Bi_2O_3-B_2O_3-Ga_2O_3 Glasses.”, Conference on Lasers and Electro-Optics, Pacific Rim (2009).

[7] J. C. Lapp, W. H. Dumbaugh, “Gallium oxide glasses.”, Key Eng. Mater., volume 94–95, pp254-278 (1994).

[8] I. B. Kacem, L. Gautron, D. Coillot, D. R. Neuville, “Structure and properties of lead silicate glasses and melts.”, Chem. Geol., Volume 461, pp104-114 (2017).

[9] J. E. Shelby, “Introduction to Glass Science and Technology.”, 2nd ed. Royal Society of Chemistry (2005).

[10] J. Cimek, R. Stępień, G. Stepniewski, B. Siwicki, P. Stafiej, M. Klimczak, D. Pysz, R. Buczyński, “High contrast glasses for all-solid fibers fabrication.”, Opt. Mater., volume 62, pp159-163 (2016).

[11] R. Stępień, J. Cimek, D. Pysz, I. Kujawa, M. Klimczak, R. Buczynski, "Soft glasses for photonic crystal fibers and microstructured optical components.", Opt. Eng. 53(7), pp071815 (2014)

[12] R. Stępień, R. Buczynski, D. Pysz, I. Kujawa, A. Filipkowski, M. Mirkowska, R. Diduszko, “Development of thermally stable tellurite glasses designed for fabrication of microstructured optical fibers.”, Journal of Non-Crystalline Solids, Volume 357, Issue 3, pp873-883 (2011).

[13] A. K. Varshneya, J. C. Mauro, “Fundamentals of Inorganic Glasses.” (Third Edition), Elsevier (2019).

[14] A Dietzel, Glasstech. Ber., volume 22, pp41 (1968).

[15] J.H. Welch, “A simple microscope attachment for observing high-temperature phenomena.”, J. Sci. Instrum., volume 31(12), pp458-462 (1954).

[16] J.H. Welch, “Improved microfurnace power supplv.”, J. Sci. Instrum., volume 38(10), pp402-403 (1961).

[17] D.L. Pye, A. Montenero, I. Joseph, “Properties of Glass-Forming Melts.”, CRC Press, pp489 (2005).

[18] H.M. Oo, H. Mohamed-Kamari, and W.M.D. Wan-Yusoff. “Optical Properties of Bismuth Tellurite Based Glass.”, Int. J. Mol. Sci., volume 13, pp4623-4631 (2012).

[19] Y.B. Saddeek, B. Yasser, H.A. Afifi, N.S. Abd El-Aal, “Interpretation of mechanical properties and structure of TeO_2–Li_2O–B_2O_3 glasses.”, Phys. B, volume 398, pp1–7(2007).

[20] P. Hlubina, “White-light spectral interferometry with the uncompensated Michelson interferometer and the group refractive index dispersion in fused silica.”, Opt. Commun., volume 193, pp1-7 (2001).

[21] J. A. Duffy, and M. D. Ingram, “Optical Properties of Glass.”, The American Ceramic Society, Westerville, pp159-184 (1991).

[22] I. Kujawa, R. Kasztelanic, R. Stępień, M. Klimczak, J. Cimek, A.J. Waddie, M.R. Taghizadeh, R. Buczyński, “Optimization of hot embossing method for development of soft glass micro components for infrared optic.”, Opt.Las. Technol., volume 55, pp11-17 (2014).

[23] R. Kasztelanic, I. Kujawa, R. Stępień, K. Haraśny, D. Pysz, R. Buczyński, “Molding of soft glass refraction mini lens with hot embossing process for broadband infrared transmission systems.”, Infrared Phys. Technol., volume 61, pp299-305 (2013).

[24] A. Lin, A. Ryasnyanskiy, J. Toulouse: “Fabrication and characterization of a water-free mid-infrared fluorotellurite glass.”, Opt. Lett. 36 (2011), p740-742.

[25] P. Joshi, B. Richards, A. Jha, ”Reduction of OH ions in tellurite glasses using chlorine and oxygen gases.”, Journal of Materials Research 28(23), pp3226 (2013).

[26] I. A. Zhmyreva, I. V. Kovaleva, V. P. Kolobkov, *et al., ”*Effect of deuteration on the emissive power of rare-earth elements in tellurite glasses.”, *J Appl Spectrosc* 29, pp1119–1123 (1978). https://doi.org/10.1007/BF01124874

[27] R. A. H. Mallawany, “Tellurite Glasses Handbook: Physical Properties and Data (1st ed.).”, CRC Press. (2001). https://doi.org/10.1201/9781420042085

[28] F. Désévédavy, C. Strutynski, A. Lemière, P. Mathey, G. Gadret, et al., ”Review of tellurite glasses purification issues for mid-IR optical fiber applications.”, Journal of the American Ceramic Society, Wiley, 103 (8), pp4017-4034 (2020). https://doi.org/10.1111/jace.17078

[29] M. F. Churbanov, A. N. Moiseev, A. V. Chilyasov, V. V. Dorofeev, I. A. Kraev, M. M. Lipatova, T.V. Kotereva, E. M. Dianov, V. G. Plotnichenko, et E. B. Kryukova, “Production of high-purityTeO2-ZnO and TeO2-WO3 glasses with reduced content of OH groups,” J. Optoelectron. Adv.Mater., 9, pp3229–3234 (2007).

[30] V.V. Dorofeev , A.N. Moiseev, M.F. Churbanov, T.V. Kotereva, A.V. Chilyasov, I.A. Kraev, V.G.Pimenov, L.A. Ketkova, E.M. Dianov, V.G. Plotnichenko, A.F. Kosolapov, et V.V. Koltashev, “Production and properties of high purity TeO2−WO3−(La2O3, Bi2O3) and TeO2−ZnO−Na2O−Bi2O3 glasses.”, J. Non Cryst. Solids, 357, pp2366-2370 (2011).

[31] J-P. Laval, J-R. Duclère, V. Couderc, M. Allix, C. Genevois, et al., ”Highly Transparent Fluorotellurite Glass-Ceramics: Structural Investigations and Luminescence Properties.”, Inorganic Chemistry, American Chemical Society, 58 (24), pp16387-16401 (2019). ff10.1021/acs.inorgchem.9b01955ff. ffhal-02443274f

Chapter 4: Development of chalcogenide graded index fibers and micro-lenses by the stack and draw technique

As explained in Chapter 1, chalcogenides glasses are the best glassy candidates for application in the mid-infrared for military counter-measure system [1] as well as broadband light sources involved in many other fields such as bio-imagery [2-3], spectroscopy [4] as well as meteorology [5] and nocturnal vision camera [6-7], due to the bands of interest being used for the detection of organic molecule as well as CO_2 and O_2 situated above 5 µm in the Mid-IR. Indeed, chalcogenides and their large nonlinearity allow to generate supercontinuum spanning from 1 µm to 14 µm [8-9] which makes them the perfect choice for application above 5 µm. This is reason why dispersion management is an important parameter to take into consideration for the generation of supercontinuum due the few light sources commercially available to pump chalcogenide fibers above 4 µm. Their ZDW are indeed generally situated way above 5 µm.

The most common approach so far to produce chalcogenides-based fibers was the extrusion method [10-11], controlling the number, size, and the pitch of holes around the core to design the dispersion profile, the flexibility in term of tweaking as well as the mechanical properties of the fiber produces by this method are quite limited. Core nano structuration is a new method [12-13] to produce all-solid optical fibers allowing to decrease the reaction between the water contained in the atmosphere as well as oxygen in the holes, increasing the chemical stability of the produced chalcogenides fibers, especially sensitive to water and oxygen, and to manage the dispersion profile of the all-solid fiber, with logically much better mechanical properties than PCFs obtained by the extrusion method due to their holey nature. The biggest problem is the manual work involved in the stacking of the thousand's rods, but methods to automatize the process are being under study at ITME in collaboration with other companies. This method also allows the production of graded index fibers with complex glass family such as chalcogenides by nanostructuring the fiber core to shape the RI profile as well as the dispersion of the nGrin fibers [14]. Indeed, the modified chemical vapor deposition (MCVD) and ion exchange techniques usually used to produce silica graded index fibers is not compatible with chalcogenide glasses [15-16], but it has shown to be impossible in chalcogenide fibers. Recently, the nanostructuration of fibers by the stack and draw method has shown to be very versatile for the dispersion profile management of silica fibers. [17-18]. In the nanostructured core fibers, modal, polarization and dispersion properties of the fibers are determined by the internal nanostructure in the fiber core without the need of contribution from the air-glass cladding geometry. It recently demonstrated promising possibilities for the fabrication of nanostructured graded-index (nGRIN) fibers with arbitrarily shaped index profiles [19-21]. It consists in the creation of a transverse binary pattern of two materials with different refractive indices, with each element of it being subwavelength in diameter in the final fiber, to obtain an average refractive index profile across the core area, according to the effective medium theory (EMT)**.** The resulting profile, depending on the distribution of the rods allows us to obtain a parabolic profile of the refractive index as previously demonstrated on silica fiber [22] and borosilicate graded index fibers [23].

Previous studies simulated chalcogenide fiber produced with this technique and has shown that it offers a high degree of of dispersion management, leading to the possibility to obtain flat curve or the typical

saddle shape, all normal dispersion profiles, important to increase the resolution or precision using supercontinuum generation such as optical coherence tomography [24], ultra-short pulse applications [25] and imagery [26]. Indeed, the spectral broadening being mainly based on self-phase modulation (SPM) in an all-normal regime, the coherence of the supercontinuum generated is increased in respect to the anomalous regime where soliton dynamics and noise play a key role into the spectral broadening phenomena [27-28].

In 2019, a first attempt in which I was not involved was done using $As_{38}Se_{62}$ and Ge_{10}-As_{22}-Se_{68}, but the fiber crystallized during the drawing, due to the lower thermal stability of As-Se glass system, which led us to make a second attempt based lonely on GAS system.

In this chapter, we will present the development of the first chalcogenides graded index fiber produced by the stack and draw method. This work was done in collaboration between two academic institutions of the SUPUVIR project: The University of Rennes 1 (UR1 - UMR CNRS 6226) which synthetized in-house the highly purified chalcogenides glasses and Instytut Technologii Materiałów Elektronicznych (ITME), now known as Łukasiewicz - ITME. For its fabrication, the technique based on stack and draw mentioned above was employed, using chalcogenide glasses in the Ge-As-Se system as starting materials considering their high thermal stability and their high resistance to crystallization [29]. Micro-lenses of various diameters ranging from 40 µm to 160 µm were then produced and characterized, showing the capabilities of this method to produce nanostructured micro lenses adapted for applications in the Mid-IR from 1 to 11 µm for this composition if we consider propagation along a few hundred micrometers scale.

1. Chalcogenides glasses

1.1 Synthesis conditions

First, chalcogenides such as S, Se or Te are mixed with elements from the 4^{th} and 5^{th} group of the periodic table such as germanium or arsenic. The silica tube is first cleaned with hydrofluoric acid HF and rinsed with demineralized water multiple times. The tube is then inserted into the vacuum system made of a turbomolecular pump (10^{-6} Pa) to eliminate any trace of water and oxygen, avoiding any source of contamination. To avoid damaging the vacuum pump with gases released during the process, the apparatus is immerged in a Dewar filled with liquid nitrogen to recondense the vapors. A scheme of a typical chalcogenides synthesis is shown Figure 1.

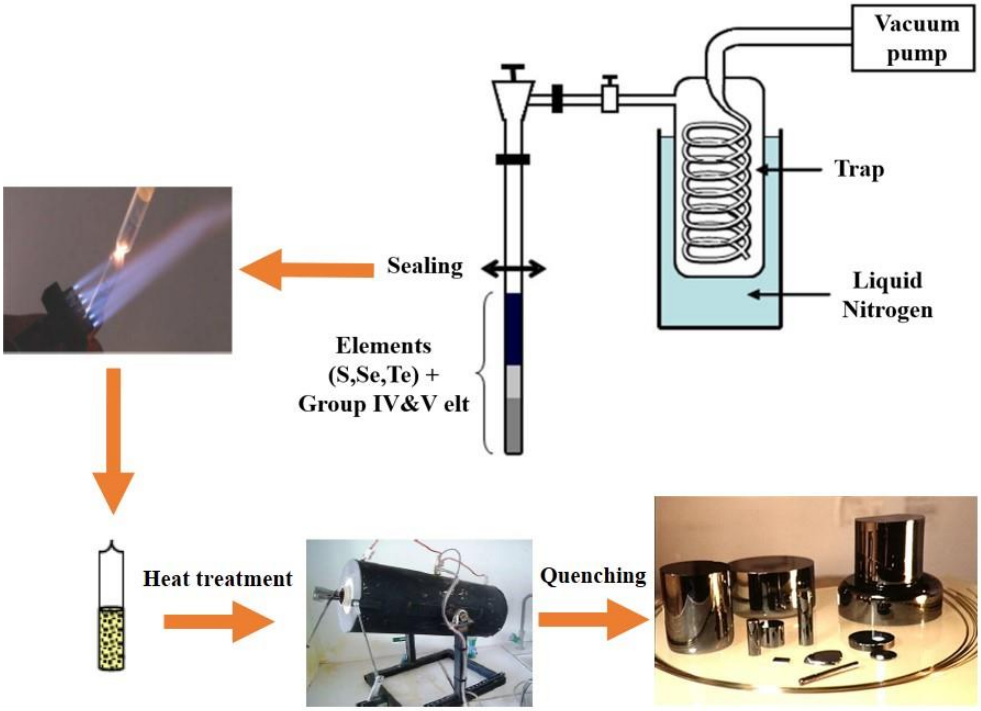

Figure 1. Synthesis condition of a typical chalcogenide glass.

The silica tube containing the composition to synthetize is then treated under vacuum again with the primary pump (10^{-3} mBar) and the turbomolecular pump (secondary pump) to achieve a pression of 10^{-5} mBar, in the secondary stage using the secondary pump. The tube is then sealed under the vacuum as shown in Figure 1 and inserted in a rocking furnace at a temperature around 850°C for approximately 8-10 hours. The rocking furnace's purpose is to homogenize the reactional melt during the synthesis. The typical heat treatment for a chalcogenide follows this route (Fig 2):

(a): Heating to the desired temperature and reaction between the elements.
(b): Fining and homogenizing the melt.
(c) and (d): Recondensation of the vapors in equilibrium with the melt.
(d): Step before the quenching, the silica ampoule is maintained in oblique position at a fixed temperature.
(e): The silica ampoule containing the melt is rapidly quenched in water corresponding to a cooling rate of 80 to 100 °C /s.
(f): Annealing at T_g ~ +10°C to release the mechanical stressed induced during the quenching
(g): Slow cooling until ambient temperature.

For the synthesis of germanium containing chalcogenide glass, the synthesis route differs as shown on Figure 2b. Indeed, the germanium contained in the composition can etch the silica tube containing the batch and pollute the final quality of the glass. For this reason, the temperature is lowered after 30 minutes at 860°C, and a short step at 840°C is done before finally getting the synthesis temperature at 680°C for a duration of 6 hours.

The quenching provokes mechanical stress due to the rapid cooling of the glass, which is why we then proceed to few hours of annealing at a temperature around the transition temperature Tg. ~ +5 – +10°C, in a furnace to allow the glass network to relax, evacuating a large part of the internal stress induced by the quenching process. A duration of 2-3 hours of annealing is considered sufficient to do so for chalcogenides, considering their viscosity properties.

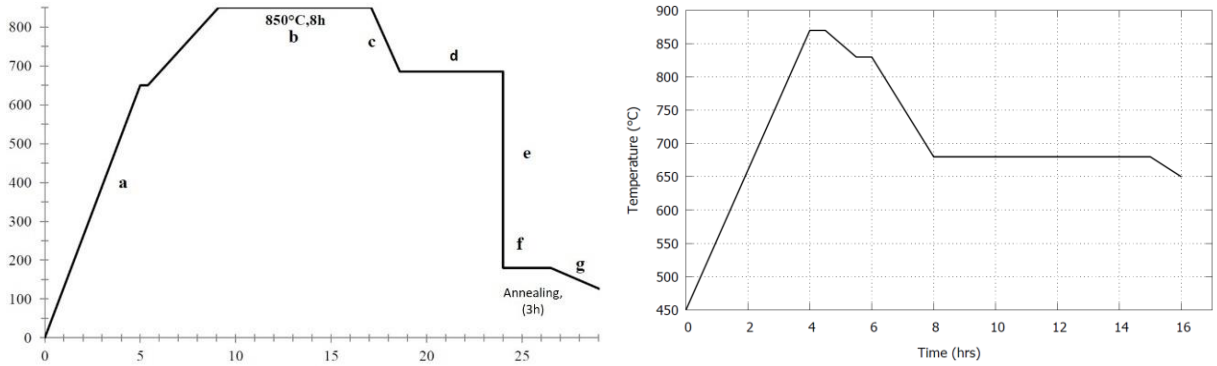

Figure 2. (left) Typical heat treatment profile of a chalcogenide synthesis. (right) Heat treatment of Ge-As-Se chalcogenide glass system.

1.2 Purification of chalcogenides glasses

Chalcogenide glasses prepared using the standard melt-quenching technique contain various impurities, coming from the starting materials as well as the synthesis setup used. This leads to an attenuation of few dB/m, as visible in Figure 3. While this is not an issue for most applications using bulk glasses or thin films, it is detrimental for applications involving long length such as optical fibers.

For the preparation of the final bulk used for the fabrication of optical elements, the glasses were purified to lower the final attenuation of the final fibers. A double distillation was performed using chemical getters added to the batch using a setup as shown Figure 4.

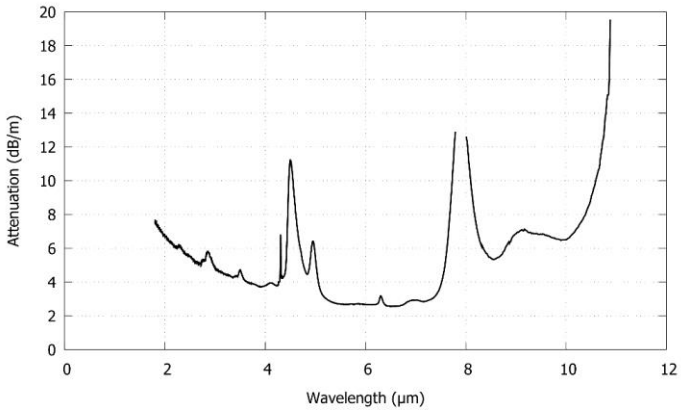

Figure 3. Typical attenuation spectrum of a selenide chalcogenide glass obtained by standard melt-quenching technique.

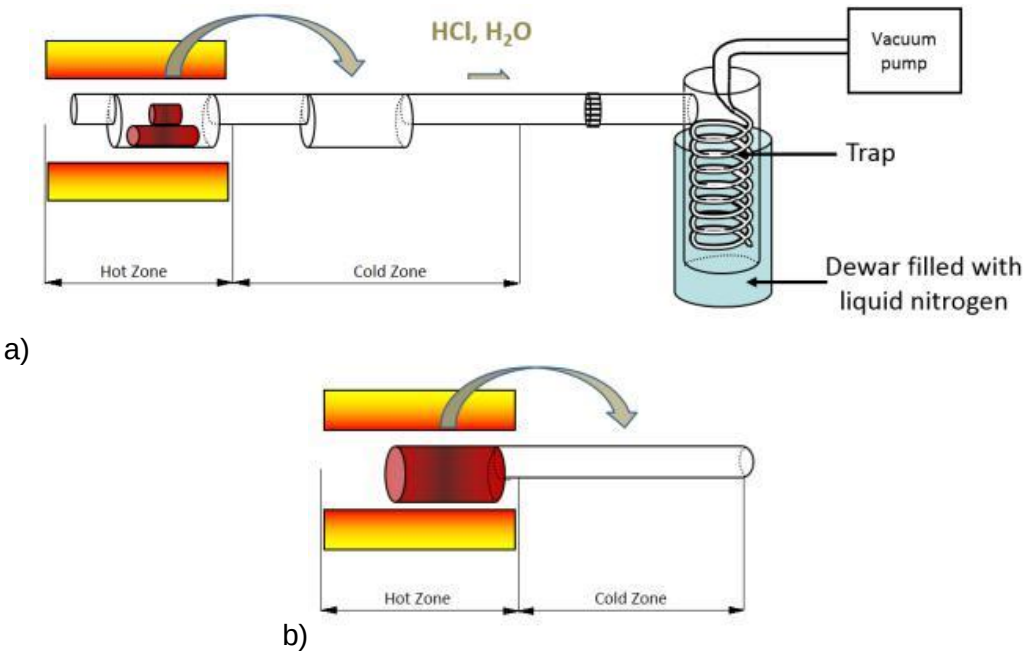

Figure 4. Schematics of the dynamic (a) and static (b) distillation processes.

The getters used for this purpose were $TeCl_4$ and Mg. Tellurium chloride was chosen because Te is well known to have the ability to enter the network of Ge-As-Se systems in small quantities without changing the glass characteristics. During the melting it reacts with hydrogen and carbon to form HCl and CCl_4, as shown below [30].

$$4\ Se\text{-}H + TeCl_4 \leftrightarrow 4\ Se + Te + 4\ HCl$$

$$C + TeCl_4 \leftrightarrow Te + CCl_4$$

Meanwhile, magnesium reacts with the oxygen forming refractory oxides such as:

$$As\text{-}O + Mg \leftrightarrow As + MgO$$

To favor these reactions, the synthesis temperature with getters is increased.

After the initial synthesis, the glass is distilled twice to remove the byproducts produced by the chemical getters. As shown in Figure 4a, dynamic distillation is first performed. The setup consists of a silica setup made of 2 zones, a hot zone and a cold zone, connected to a cold trap and a turbomolecular pump (10^{-6} mbar). The glass, introduced in the hot zone and slowly heated to 640°C, migrates to the cold zone (room temperature), leaving behind refractory impurities such as silica particles and oxides. During this first distillation, volatile byproducts such as hydrochloric acid, water and carbon tetrachloride are evacuated by the vacuum pump and trapped into the cooled silica trap.

To obtain high quality glasses, we then proceed to a static distillation to further purify the chalcogenide glass. Indeed, at this stage, the glass still contains residual traces of refractory impurities. The initial setup is sealed under vacuum to keep the batch previously purified, and a tube as shown in Figure 4b. The batch is then gradually heated until all the glass has moved from the batch to the tube, leaving behind impurities. The tube containing the desired materials is then sealed for final synthesis. Indeed, the distillation process

being thermally intensive and the various elements having different vapor pressures, the final tube contains a mixture of separated compounds, some of them being crystalline due to the lack of proper quenching and annealing. For this reason, we proceed to a final synthesis using the melt quenching technique shown in section 1.1.

Despite this double distillation, the attenuation spectra of the glasses still had high attenuation due to scattering (silica impurities from the setup entering the melt, disbalance in the stoichiometry of the getters due to various variables influencing the reaction). The double distillation process was once again performed to further purify the glass and the getters were better balanced to reduce the reaction leftovers during this second double distillation. The final attenuation spectras of the different batches synthetized of $Ge_5As_{30}Se_{65}$ and $Ge_{10}As_{22}Se_{68}$ are shown in Figure 5 and 6.

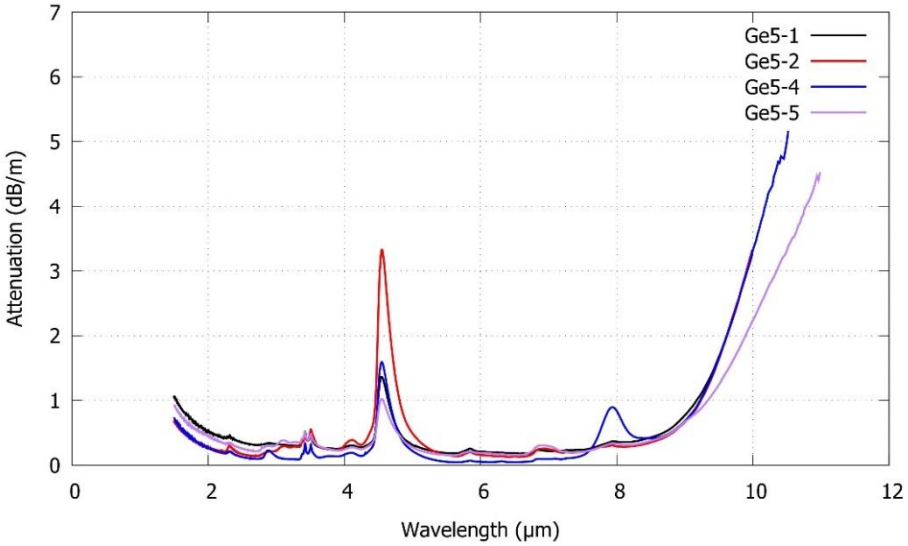

Figure 5. Attenuation spectra of the batches of glass used to produce the high index rods $Ge_5As_{30}Se_{65}$.

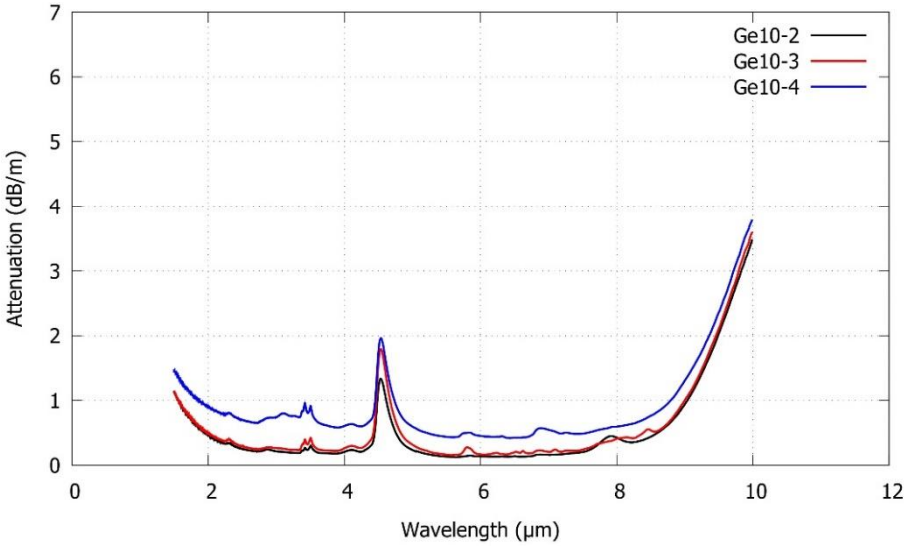

Figure 6. Attenuation spectra of the batches of glass used to produce the low index rods $Ge_{10}As_{22}Se_{68}$.

2 Fabrication of the nGrin fiber

2.1 Precursor glasses

Seeing the problems of crystallization that appeared during the first attempt of production of a graded index chalcogenide fiber, using As-Se and Ge-As-Se glass systems, a change of composition was considered. Indeed, the previous attempt led to a crystallization of the fiber due the lack of thermal stability of $As_{38}Se_{62}$ compared to the Ge-As-Se glass system. Starting from the hypothesis that $As_{38}Se_{62}$ was the source of the problem and knowing that the addition of germanium increases the stability of the glass structure, for the second attempt in the development of a graded index fiber with transmission in the Mid-IR, the following two glass compositions were used to make rods with the composition $Ge_5As_{30}Se_{65}$ and $Ge_{10}As_{22}Se_{68}$ as shown on the ternary diagram Figure 7. These two compositions exhibit a refractive index difference $\Delta n \approx 0.1$ at 1.55 µm while having similar enough T_g and viscosity to allow for simultaneous drawing: Tg = 175°C for $Ge_{10}As_{22}Se_{68}$, containing more germanium, and 165°C for $Ge_5As_{30}Se_{65}$.

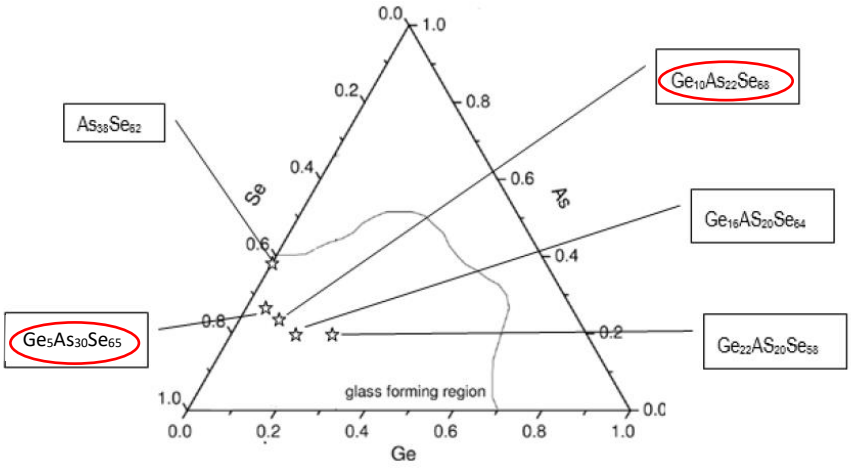

Figure 7. Ternary diagram of Ge-As-Se system showing the composition of the glass used for this study as well as the glass forming region.

2.2 Refractive index matching

The choice of glasses is based on several parameters. First, the viscosity characteristics of both glasses, in other words their working temperatures, must be close enough to be compatible for fiber drawing the preform. Here, the viscosity difference between $Ge_5As_{30}Se_{65}$ and $Ge_{10}As_{22}Se_{68}$ is negligible. The refractive index difference must also be different, here the refractive index difference $\Delta n=0.1$. Refractive index dispersion curves for both compositions were determined by shifting the Sellmeier curve for a similar composition obtained from literature ($Ge_{10}As_{23.4}$ $Se_{66.6}$, from [31]) to match it with our measurement of n at 1.55 µm and 1.31 µm done by the prism coupling. The resulting curves and coefficients can be found respectively in Figures 8 and 9, and in Table 1 as well as the measured characteristics of the 2 compositions in Table 2.

	$Ge_5As_{30}Se_{65}$	$Ge_{10}As_{22}Se_{68}$
A0	3.0841	2.806
A1	3.0082	2.7938
a1	0.40385	0.41025
A2	0.74782	0.77098
a2	38.451	39.463

Table 1. Sellmeier coefficients extrapolated for the two used compositions.

The equation used was:

$$n^2 - 1 = A_0 + \sum_{i=1}^{m} \frac{A_i \lambda^2}{\lambda^2 - a_i^2}$$

in the two poles approximation (m = 2).

Table 2. Summary of the characteristics measured on bulk samples of the two used compositions.

Composition	$Ge_5As_{30}Se_{65}$	$Ge_{10}As_{22}Se_{68}$
Average coordination number	2.4	2.42
T_g (°C, ± 2°C)	165	175
Refractive index at 1.55 µm	2.704	2.618

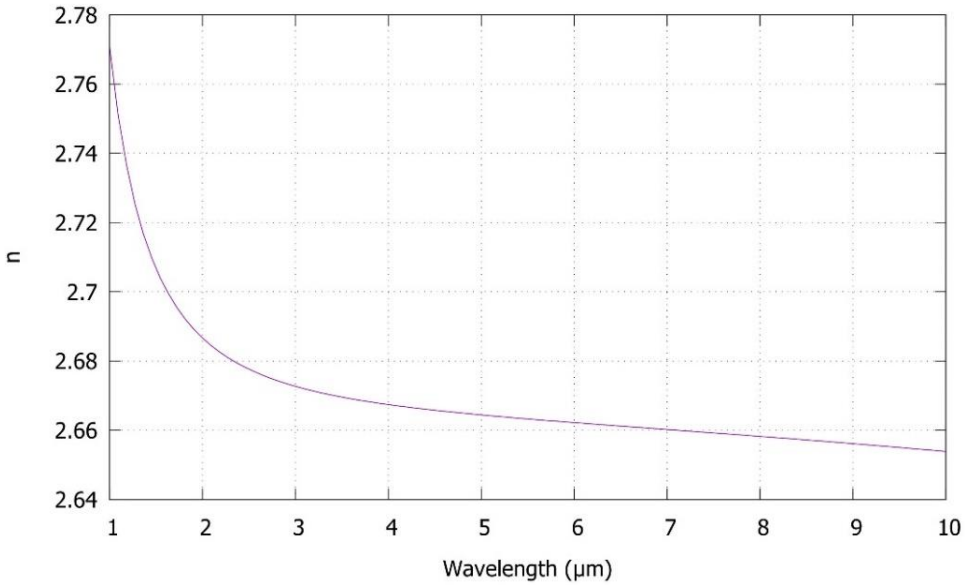

Figure 8. Fit of the Sellmeier curve of $Ge_5As_{30}Se_{65}$ glass.

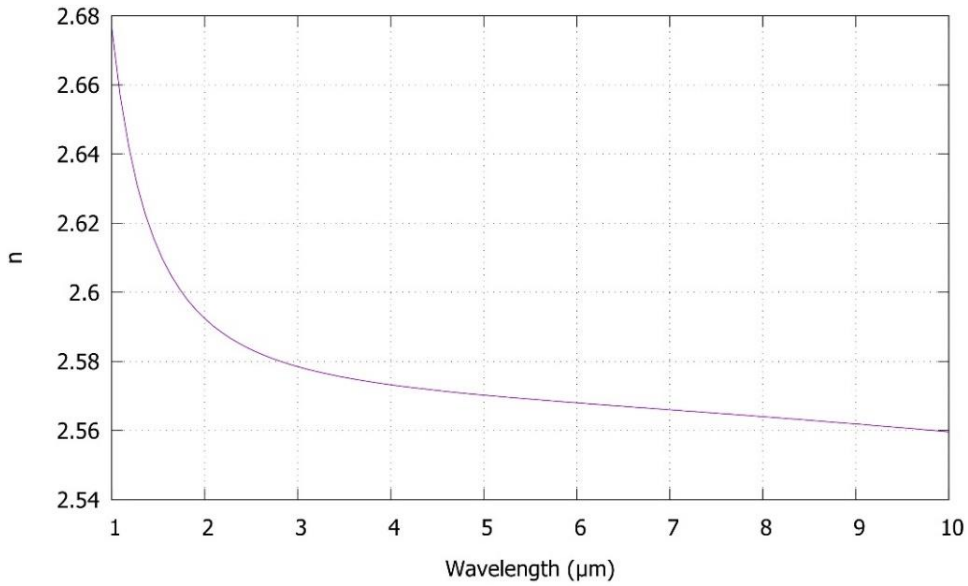

Figure 9. Fit of the Sellmeier curve of $Ge_{10}As_{22}Se_{68}$ glass.

2.3 Simulation of the core structure

The simulated annealing method, based on a Monte-Carlo simulation like direct binary search and the genetic algorithm was used to generate a complete random distribution of the two compositions in a first step. At every iteration, the composition of one random element is changed, and the standard deviation of the averaged index distribution in the core to the desired index pattern is calculated. If the value is smaller than the previous iteration, the change is accepted. If it is larger, the change is accepted with a probability p such as (Eq 5).

$$p = k.e^{\frac{\Delta}{T(I)}}$$

where k is a constant, Δ is the difference in standard deviation, and T(I) is a parameter that is decreased exponentially with the number I of iteration steps. At the end, structures shown in Figure 10a and 10b are obtained.

The difficulty involved in the stacking of the preform induces some limitations. Firstly, if the rods to stack are too small, they become too flexible making the stacking process impossible, especially for chalcogenide glasses, and secondly, the accuracy of the manual stacking decreases due to eventual mistakes. There is also a limitation due to the size of the silica furnace used to draw the fiber. For this reason, the core structure was limited to 817 rods, with a diameter of 450 µm, corresponding to a preform diagonal composed of 33 rods (Figure 10).

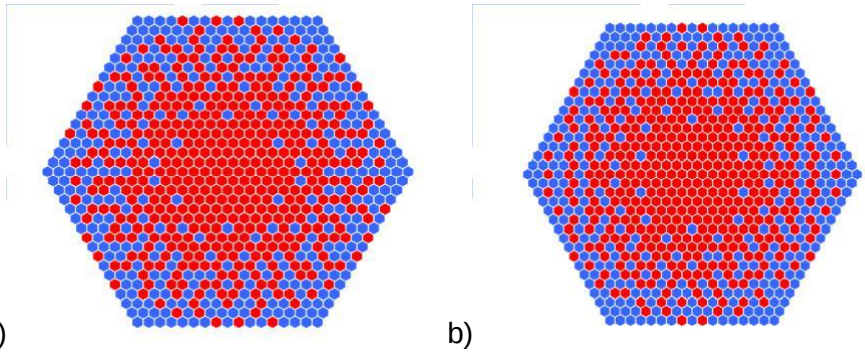

a) b)

Figure 10. Stack configuration simulated for preform A (a) and preform B (b), with the low n rods in blue and the high n ones in red.

2.4 Rods preparation

To prepare the stacks, the glasses presented in the previous sections were drawn into 450 µm diameter rods with a length of 9 cm for the $Ge_5As_{30}Se_{65}$ composition and of 10 cm for the $Ge_{10}As_{22}Se_{68}$ composition. This allows us to differentiate the two glass compositions for the stacking process. In case of mistake, the rods can be sorted and restacked. The diameter of the rod is controlled by the preform motion on the y axis, the feeding rate, and the drum rotation speed carrying the fiber. The section area must match the volume flow of the glass at the desired temperature leading to a condition which must be respected such as:

$$S_p . v_p = S_f . v_f$$

With S_p and V_p the section area and the speed of the preform, and S_f and V_f respectively the section and the pulling speed of the fiber.

Assuming a circular shape of the final fiber and of the preform used, we can determine the diameter of the produced fiber ϕ_f from the preform diameter and the speed of the preform v_p and the fiber drawing speed v_f such as:

$$\phi_f = \phi_p . \sqrt{\frac{v_p}{v_f}}$$

Before starting to heat the preform, a 30 min purge of the furnace with argon (due to its lower cost compared to helium) was performed to avoid glass oxidation during the drawing procedure. After this, the gas was switched from Ar to He, with a flow of 1.5 L/min, and the furnace was heated up to drawing temperature. The preforms were drawn using a capstan. The drawing speed, of about 0.7 m/min, was calculated for the different preforms (which had slightly different diameter) using Equation 2 when the final fiber diameter is obtained, the drawing speed is adjusted so it satisfies the equation:

$$v_f = v_p . \frac{\phi_p^2}{\phi_f^2}$$

With ϕ_p, v_p indicating respectively the diameter and speed of the preform and ϕ_f, v_f, the ones of the fiber. The preform motion speed was set at 1 mm/min. Note that about 1800 rods fitting our diameter

requirements have been obtained, and ovality has been < 1% for the whole duration of all the drawings Preform stacking.

2.5 Preform stacking

The obtained rods after being cleaned with vacuum cleaner were stacked in a hexagonal lattice, following the configuration in Figure 11.a and 11b, by hand. The process is fastidious and meticulous. Indeed, a simple mistake can cause the operator to restart the whole stacking process from the beginning due to the impossibility to control the many layers at the bottom, which means going through the whole glass triage and cleaning process again. The resulting preform is then fixed with hexagonal steel rings to keep its shape (Figure 11b).

Figure 11. (left) example of stacked structure is shown on the apparatus used to stack, (right) final sealed stack of preform B.

2.6 Preparation of the clad

The cladding tubes for the fiber drawing attempts were prepared by rotational casting technique: shards of high purity $Ge_{10}As_{22}Se_{68}$ were placed in 10 cm long silica tubes, sealed under high vacuum. The internal diameter of the silica tubes was 12 mm. The glass was afterwards melted at 550 ℃ and, as soon as it was taken out of the furnace, spun at 3000 rpm until it cooled down to a temperature slightly higher than T_g (in our system, this happens in around 6.5 minutes). The resulting tubes were annealed at 170℃ for 30 minutes.

2.7 Core rod drawing

Due to the nature of chalcogenides glasses, the structure of this drawing tower is a bit more complex than the usual towers used for other glasses. The fiber drawing tower used for these fibers is schematized in Figure 12. It is composed of silica tube enclosure connected to a vacuum pump as well as helium and argon gas arrivals with a heating ring, used to heat up the preform at the working temperature in order to draw it into optical fibers.

The preform, sealed with Teflon, is connected to the vacuum pump, the argon arrival as well as a motor moving the preform along the y axis. The feeding rate is defined as the speed the preform is inserted into the heating zone.

To obtain a sub preform from the stack, two steps are needed: partial collapsing and drawing. Partial collapsing is a critical step to obtain high quality chalcogenides fibers using this method. They are indeed sensitive to the presence of oxygen and elements like hydrogen as explained before, and the structure has to be conserved. For this reason, the stack must be collapsed in an airtight Teflon top layer to clean the stack and conserve the structure. We first apply helium into the sub-preform stack and then put it under a low vacuum for 30 minutes (-50 mBars) while we flux the furnace with argon for 30 minutes. We then switch the furnace gas input from Ar to He and slowly increase the temperature. Once reached 335℃, a decrease in the diameter of the stack could be observed in the hot zone, and therefore the preform motion was started with a speed of 5 mm/min, allowing to heat the whole preform. The goal of this procedure was to reduce the viscosity of the external layers of rods while pressing them together by the tension of Teflon and the effect of vacuum. This allows for the affected rods to stick together, creating an airtight layer that will allow drawing without the use of Teflon coating. The resulting partially collapsed preform can be seen in Figure 14.a. These parameters led to a strong deformation of the core, causing it to become heavily twisted as shown on Figure 13b and Figure 14b. The twisting of the core preform is not a concern considering it becomes negligeable once drawn into a long length fiber. This phenomenon could be due to the forces induced by the rings holding the core preform unevenly at the top as well as the force induced by the Teflon holding the structure in place, causing it to rotate during the partial collapsing procedure.

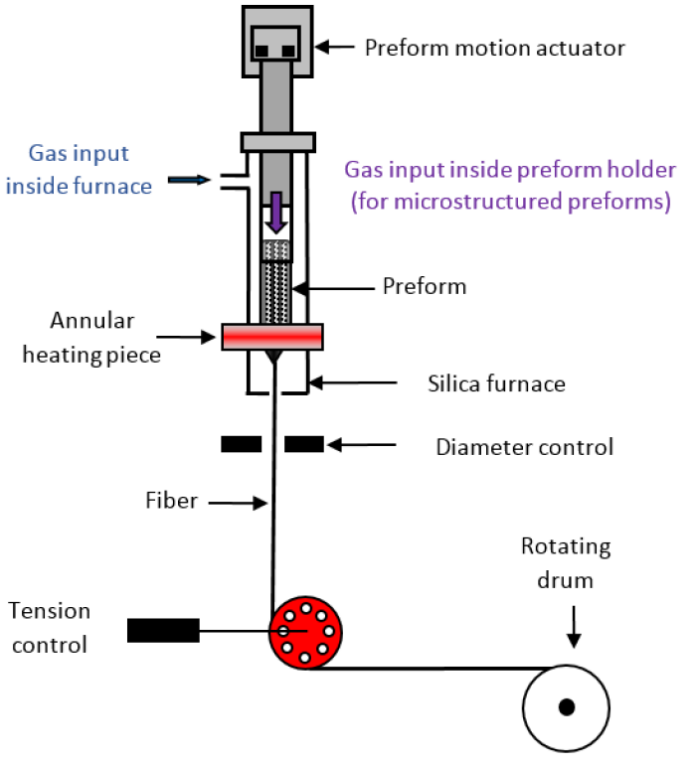

Figure 12. Schematic of the drawing tower used for chalcogenides.

a)  b) 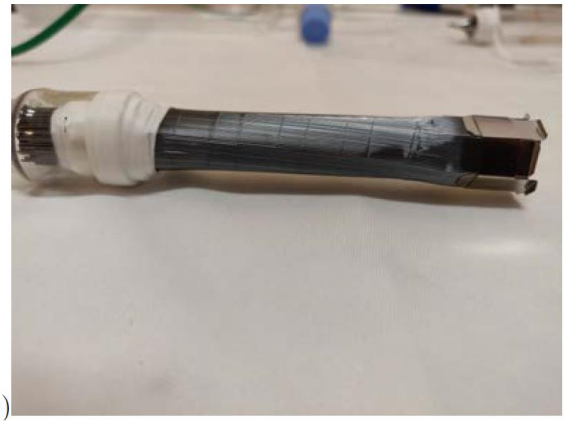

Figure 13. (a) stacked covered with a Teflon tape before the collapsing process, (b) partially collapsed preform B with a visible torsion on the structure.

a)  b) 

Figure 14. a) Airtight Teflon cladding of the stack connected to the drawing tower after the collapsing process at 335 degrees, b) Partially collapsed stack without the Teflon coat.

This preform was then, using a capstan, drawn into canes to be used as core for our nGRIN fibers; once again, during this procedure, vacuum was applied in the attempt to close the remaining interstitial holes. Two different diameters were drawn: 1 and 2 mm. The goal is to use the 1 mm cane to obtain a 125 µm fiber with a core of around 10 µm and rods diameter of around 300 nm. However, being at the technological limit of what can be accomplished by our method (the clad was to be prepared by rotational casting, and the minimum obtainable diameter of the hole is 3 mm), the other sizes were drawn in case of impossibility in using the 1 mm one.

As visible in Figure 15, the structure was conserved in the drawing. Not all the empty spaces were completely collapsed, but this problem can be addressed during the fiber drawing, assuming the holes are through along the whole rod and therefore vacuum can be applied to them.

2.8 Microscope imaging of core rods

To obtain informations of the actual state of collapsing and conservation of the core structure in the sub-preform, and therefore carefully plan the next steps of drawing, imaging under optical microscope was performed. The pictures obtained this way are shown in Figure 15.

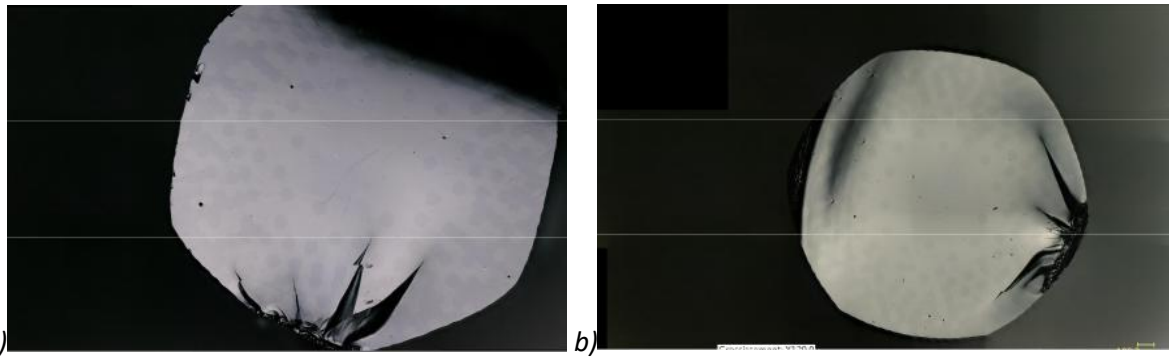

Figure 15. Microscope imaging at 1000X magnification of the 1 and 2mm rods obtained from preform A (a) and preform B (b).

2.9 Fiber drawing

Using the core rods and the tubes obtained in the previous sections, fibers were obtained by standard rod-in-tube technique. To begin, the core rod was placed in the tube and fixed in place with the use of Teflon tape, carefully avoiding to completely close the tube's hole. The tube was then placed on the drawing tower, and a 30 min purge of the furnace with argon was performed. After this, the gas was switched from Ar to He, with a flow of 1.5 L/min, and the furnace was heated up to drawing temperature. Upon formation of the drop, vacuum was applied to the internal part of the tube, helping it to collapse around the rod.

2.9.1 Preform A

Not being sure a 1 mm diameter rod would be working, we started with a 2 mm diameter rod inserted in a tube of ϕ_{ext} = 12.1 mm, ϕ_{int} = 3.1 mm. Using this rod, it was possible to obtain a homogeneous fiber, without visible defects or core deformation. Two different fibers were drawn, ϕ250 µm with a 40 µm core and ϕ125 µm with a 20 µm core.

Once these fibers were produced, we moved to an attempt with a 1mm core rod to produce ϕ125µm with a 10 µm core. In this case too, we succeeded in drawing fibers showing no interface defects visible with an optical microscope up to a 100x magnification. During the drawings, two different regimes were used: a low tension, low vacuum one (15 g, - 20 mbar, 331℃) and a high tension, high vacuum one (25 g, - 50 mbar, 318℃).

2.9.2 Preform B

For the preform B, in order to have a comparison with preform A, we drew exactly the same diameters of fibers and cores (ϕ250 µm with a 40 µm core, ϕ125 µm with a 20 µm core and ϕ125 µm with a 10 µm core). The tube used as cladding for preform B had ϕ_{ext} = 12.05 mm, ϕ_{int} = 2.5 mm. For preform B, 10 µm core, in addition to the parameters mentioned in the previous section, a new set of parameters was

attempted to increase the diffusion of germanium between the core elements, thus reducing scattering losses (tension of 7-8 g, vacuum - 20 mbar, 360℃).

2.9.3 Tapering

To obtain lower diameter fibers, tapering was attempted. The 10 µm core fiber obtained from preform B, being seemingly the most promising one, according to preliminary results showing that the transmission of the preform B was far superior to preform A, preform B was used as the base for an attempt at taper production (Section 3.1.1 and 3.1.4). The first target chosen was to reach a core size of 5 – 6 µm. The tapers were produced by installing the fibers on the drawing tower, heating them in helium atmosphere and elongating them the same way a preform is elongated during fiber drawing. A temperature of 230℃, corresponding to a tension of 25-30 g, was used. Two tapers were produced this way, both having a waist diameter of 70 µm, corresponding to a 6 µm core. One has a waist length of 20 cm, and the other of 8 cm. In the second one, light transmission at 1.55 µm was observed, as shown in Figure 16. Tapers with different lengths and core diameters were prepared for the measurements described above (4.4, 5.6 and 7 µm cores).

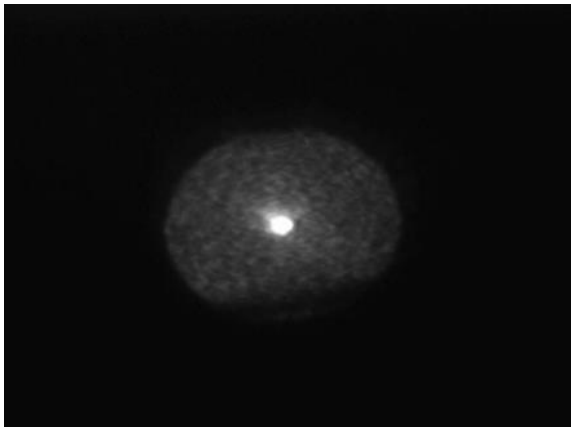

Figure 16. Mode image of the 10 µm core fiber obtained from Preform B, tapered along 8 cm to a core size of 6 µm.

3 Characterization of the developed nGriN chalcogenides fibers

3.1 Fiber characterisation

3.1.1 Optical microscope imaging

All the fibers drawn were sampled in different points along the fibers and imaged using a Keyence VHX 5000 digital optical microscope, to check for the presence of defects. No defects were found, and the core was visible, as shown in Figure 17. The various core diameters estimated with the microscope matched the expected core diameters. Later, imaging with better contrast conditions performed on the fibers obtained from preform B showed that the error on the core diameters of the 40 and 20 µm core fibers is less than 1%, while the fiber with the nominal core diameter of 10 µm seems to have an actual one of about 11 µm.

a) 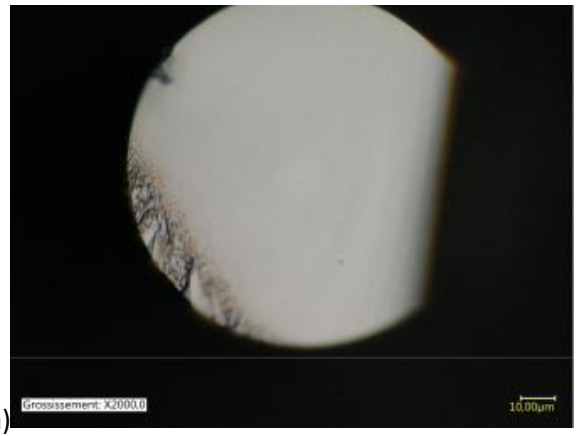

b) 

Figure 17. Microscope image of the 10 µm core fibers obtained from Preform A(a) and preform B (b).

In some sections of the fiber, however, small holes are present inside the core, as shown Figure 18. This can be attributed to the presence of bubbles in the core rods, due to the incomplete collapsing of the initial stack.

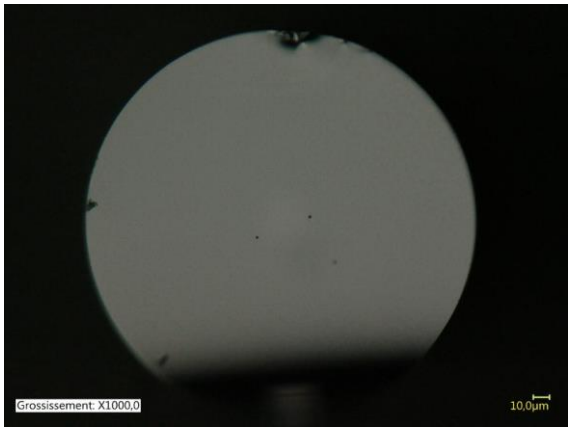

Figure 18. Microscope image of the 40 µm core fibers obtained from Preform B. Some defects are visible in the core.

3.1.2 Mode imaging with CO_2 laser

Using a CW CO_2 laser with lines of wavelength between 9.3 and 10.6 µm, images of the mode profiles in the core of the different produced fibers were taken. To isolate the core of the fiber, graphite was applied on the external fiber surface. Having extremely high absorption in the Mid-IR, graphite can eliminate most of the light propagating in the cladding of the fiber, leaving only light guided in the core to be detected. This allowed us, using a proper lensing system and a forward looking Infrared (FLIR) camera A-600 series, to get pictures of the modes propagating in the core of the fiber.

In the 10 µm core fibers, for both preforms, we observed a single mode behavior with a Gaussian mode profile whereas the 20 µm and 40 µm have shown to be multimode. Pictures collected with the camera for the 10 µm fibers, along with the corresponding mode profiles, are shown in Figure 19.

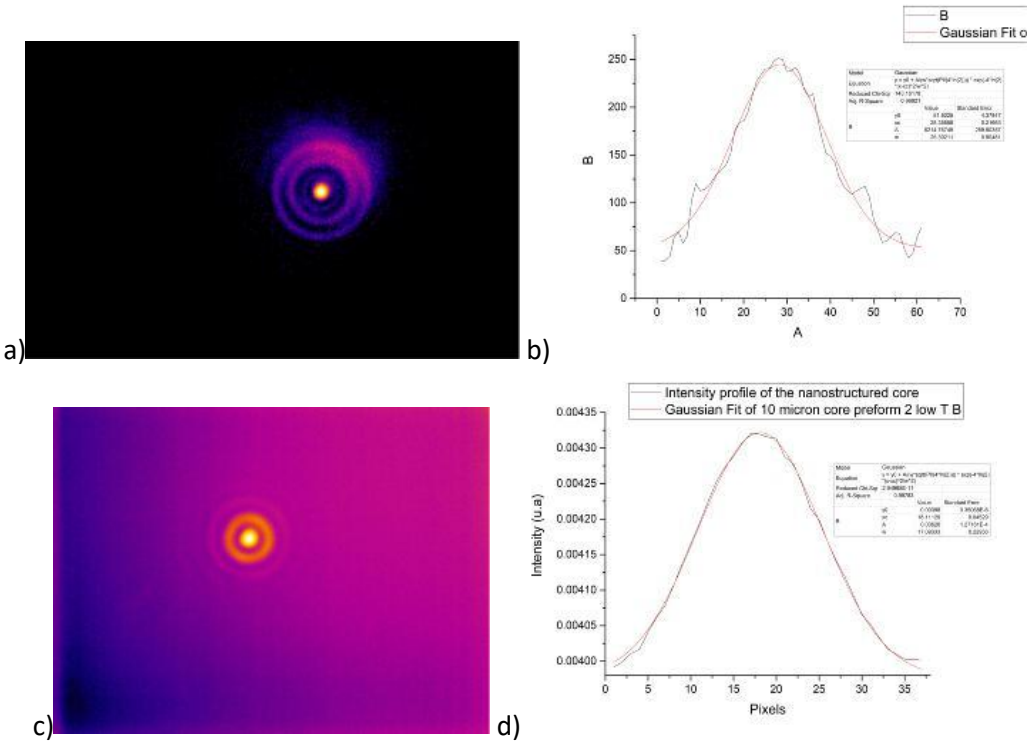

Figure 19. Mode image and corresponding profile of the 10 µm core fibers obtained from Preform A (a, b) and preform B (c, d) when injected with a 10.5 µm laser.

3.1.3 Mode imaging with 1.55 µm laser

In order to picture the core at 1550 nm, we used a 1.55 µm CW laser and injected the fiber core. Once again, we applied graphite on the fibers to prevent light propagation in the cladding, due to the high attenuation of graphite.

Confinement losses could be observed for all the fibers measured but seemed much lower for the nGrins developed from the Preform B, with a 10 µm core drawn at low temperature, based on the intensity of the output. The propagation at 1.55 µm could not be observed for the first Preform, for the 40 µm and 20 µm core fibers. On the contrary, the 10 µm core and all fibers developed from the second preform presented a propagation at this wavelength as shown on Figure 20. At this wavelength, all fibers have shown to be strongly multimode. The propagation at 1550 nm was also confirmed by the transmission spectra measured using an FTIR and an MCT detector, presented in Section 3.1.4.

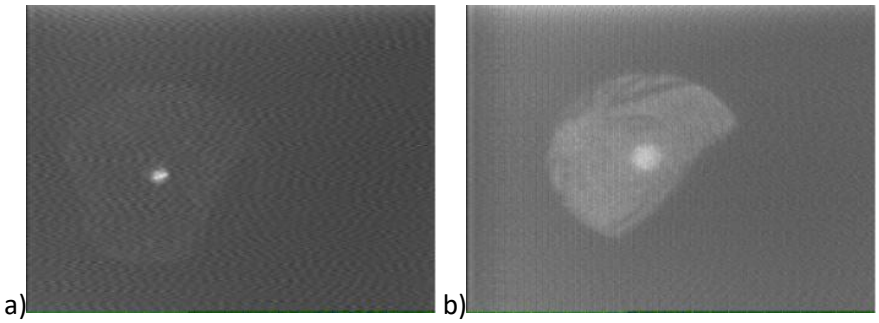

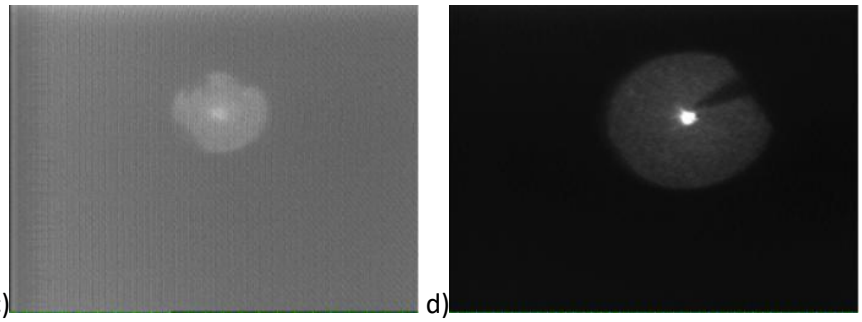

c) d)

Figure 20. Mode image of the 10 µm core fibers obtained from Preform A (a) and 40 µm, 20 µm and 10 µm obtained from Preform B with a low temperature drawing (b, c and d), when injected with a 1.55 µm CW laser.

3.1.4 Transmission measurements

For all the obtained fibers (apart from the one drawn at low tension and high temperature from Preform B, which has been shown to be of poor quality), transmission was measured on a Bruker T37 FTIR apparatus, using an external Mercury-Cadmium-Telluride (MCT) detector to collect the signal. To be able to compare the results, all fibers were cut to the same length of 20.5 ± 0.3 cm. The fibers are then cleaved, covered with graphite to remove the light from the cladding as explained in previous sections, and placed in the measurement setup using fast connectors. Transmission spectra in the 1-12.5 µm range were then collected. To compare the transmission of the fibers with different core sizes, T was normalized by the core area. The normalized transmission is comparable for the 10 and 20 um cores for the 2 preforms while the transmission of the 40 µm cores is clearly much more lossy (Figure21 a and b).

The transmission of the 10 µm core fibers, obtained by both preforms, is compared in Figure 22. Looking at this, the one obtained from preform B seems to be the most promising, especially at lower wavelengths.

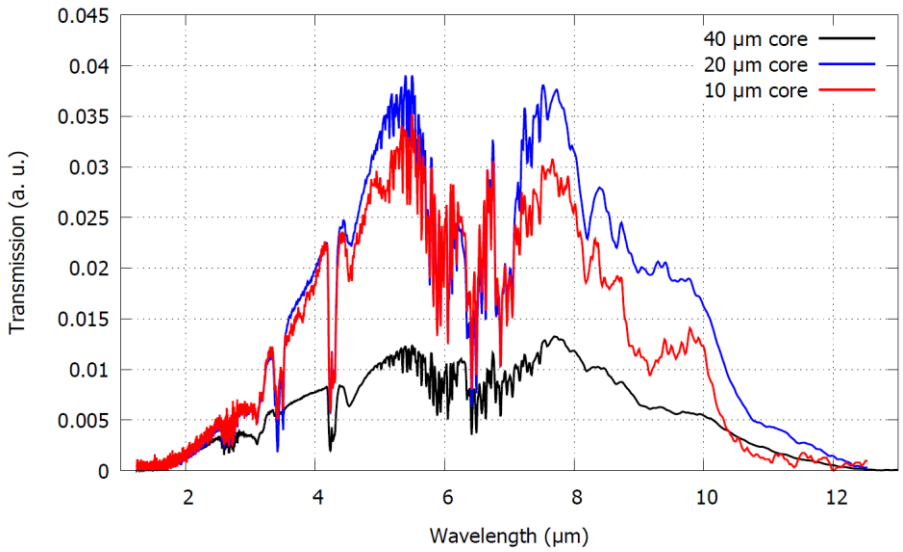

(a)

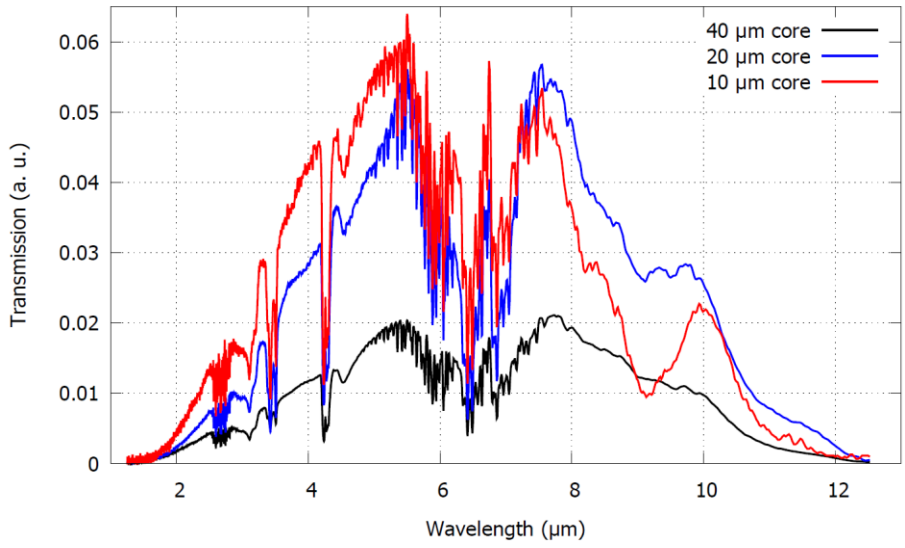

(b)

Figure 21. Transmission, normalized by core area, of the fibers obtained from preform A (a) and preform B (b).

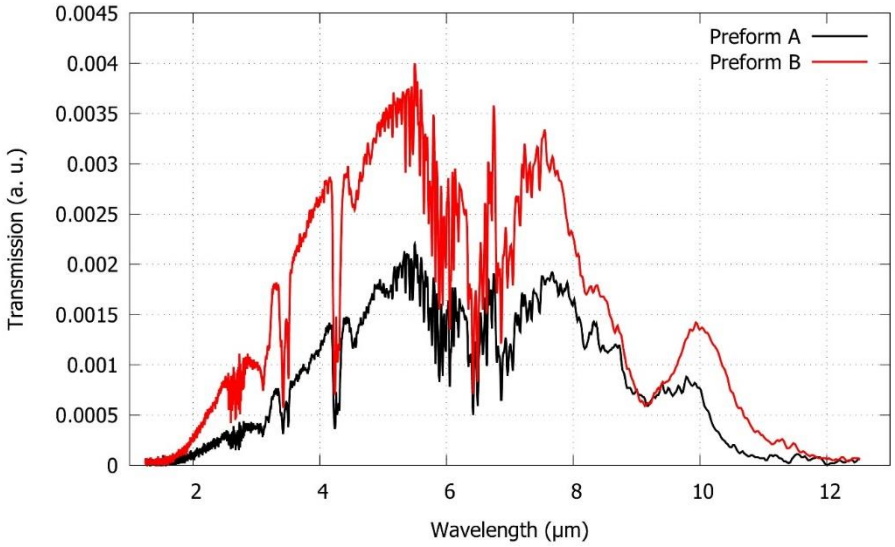

Figure 22. Transmission of the 10 µm core fibers obtained from preforms A and B.

Based on the transmission characteristic of the 2 preform, the preform B having a higher transmission as shown on Figure 22 and based on the number of defect visible using an optical microscope as shown section 3.1.1, we have chosen preform B to be our base preform to produce optical fibers.

3.1.5 Attenuation measurement

Attenuation of 10, 7, 5.6- and 4.4 µm core fibers were measured using the cutback method, from 1.2 µm to 2.4 µm, using an Optical Spectrum Analyzer Yokogawa and a supercontinuum source from LEUKOS spanning from 200 nm to 2400 nm. Due to the high absorption of the glass at wavelengths lower than 1 µm, wavelengths lower than 1.2 µm were filtered out to avoid damaging the fibers. Two consecutive cutbacks were performed at equal lengths (5 cm), and an average was made between the different

attenuation measurements (Fig. 23). The attenuation peak around 1.5 µm is explained by the coating used, absorbing light at these wavelengths, this can also be seen in Figure 24. We observe a diminution of the attenuation with the core size which is easily explained by the better confinement of smaller cores.

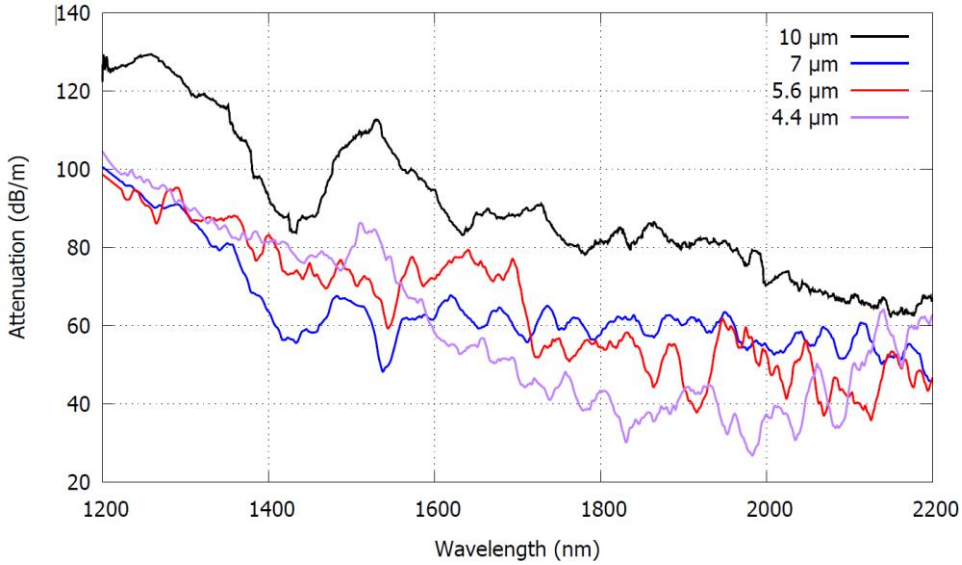

Figure 23. Attenuation measurement in the range 1.2 to 2.4 µm of the 4.4, 5.6, 7 and 10 µm core fibers obtained from preform B.

Attenuation measurements were also performed using an FTIR from 2 to 11 µm, using an MCT detector. Graphite was, once again, applied on the fiber, before finally proceeding to a single 10 cm cut-back measurement. The measurement from 1.2 to 2.4 µm and the measurements from 1 to 11 µm follow the same trend, as shown in Figure 24.

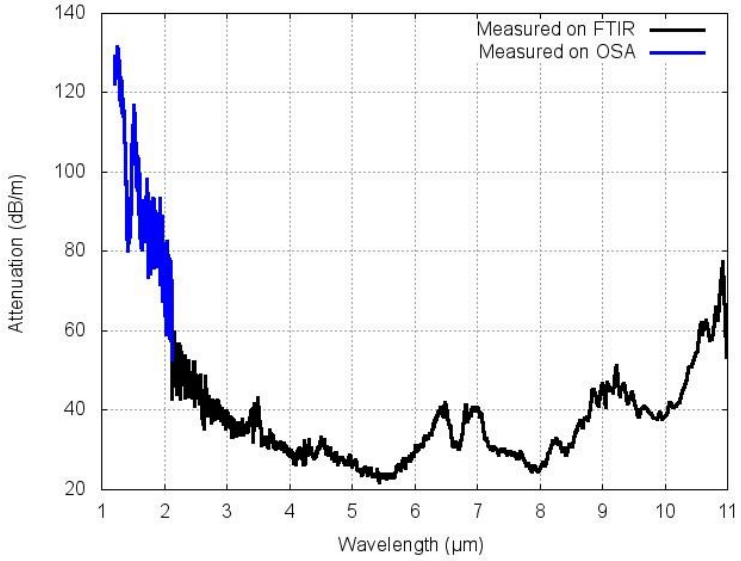

Figure 24. Comparison of the attenuation measurements performed in the range 1.2 to 2.4 µm and 2 µm and 11 µm ranges, for the 10 µm core fiber obtained from Preform B.

3.1.6 Dispersion measurement

The theoretical dispersion curve of the fundamental mode could then be obtained doing the simulation of various fibers core size issued from preform B, using the finite difference method (FDE). 6 µm, 10 µm, 20 µm, 40 µm core sized were simulated to evaluate the dispersion dependance of the core size. Results were plotted on Figure 25. As we can see, the dispersion decreases with smaller cores and acquired a saddle shape from 10 µm core diameter. The zero-dispersion wavelength for the 40 µm core and the 20 µm core are very close, around 7 µm, while the 10 and 20 µm core dispersion curves stay in normal regime ($D < 0$).

Dispersion was experimentally measured using a Mach Zehnder interferometer setup and a supercontinuum source from LEUKOS, spanning from 200 nm to 2400 nm (Fig. 26).

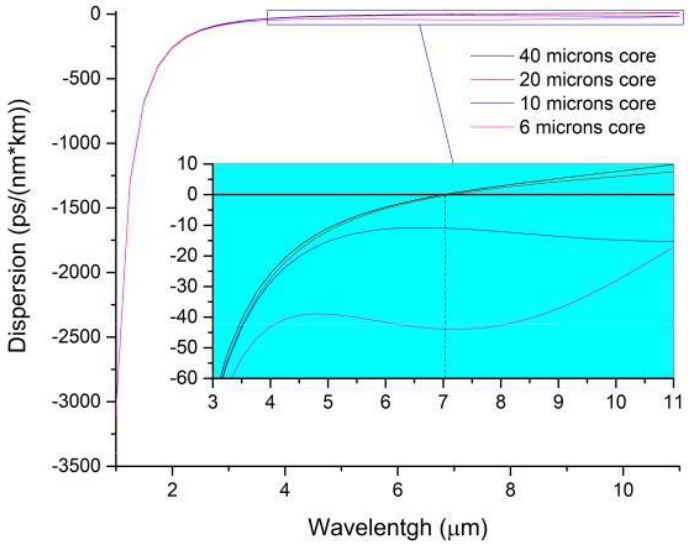

Figure 25. Dispersion simulation in the range 1.5 to 11 µm of the 6 µm, 10 µm, 20 µm and 40 µm core fibers obtained from preform B.

The optical path difference (OPD) introduced by the fiber in the signal arm was then measured as a function of the equalization wavelength from 1200 to 2400 nm, using a Yokogawa Optical Spectrum Analyzer (OSA) AQ6375B and a LEUKOS supercontinuum source spanning from 200 to 2400 nm (Figure 27). It was also measured separately at DTU from 3.4 to 4.6 µm using a custom NKT SuperK MIR supercontinuum source (Figure 28) and a scanning spectrometer. For the calculation, we also took into consideration the small OPD induced by the optical elements introduced in the optical setup, using the dispersion and thickness characteristics of the lenses and filters (C230TM, A110TM lenses and an ND filter). The group refractive index was then fitted to a 5 parameters functions:

$$N(\lambda) = \frac{A_1}{\lambda^4} + \frac{A_2}{\lambda^2} + A_3 + A_4.\lambda^2 + A_5.\lambda^4$$

The dispersion was then obtained from the first derivative of N(λ) such as:

$$D(\lambda) = \frac{10^4}{3} \cdot \left(\frac{-4A_1}{\lambda^5} + \frac{-2A_2}{\lambda^3} + 2A_4.\lambda + 4A_5.\lambda^3 \right)$$

10, 7, 5.6 and 4.4 µm core fibers from Preform B were measured, as shown in Figure 27.

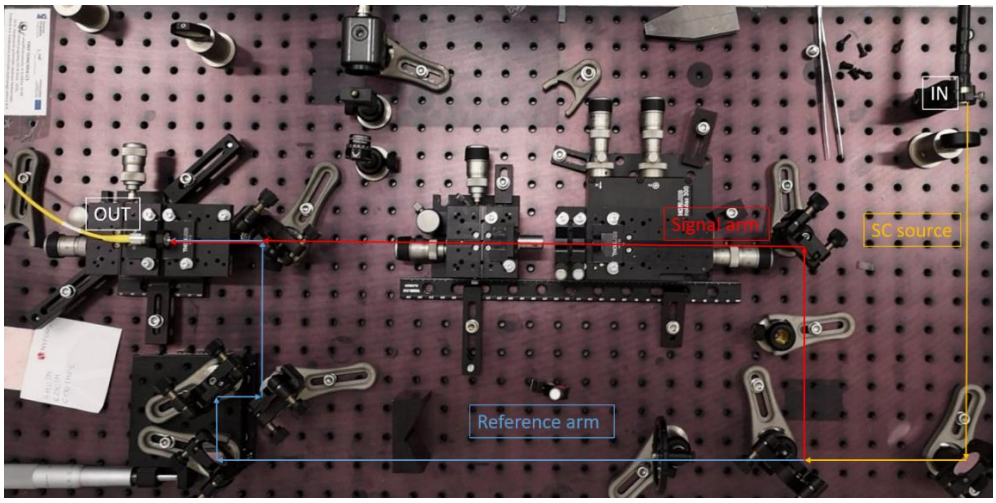

Figure 26. Mach Zenhder interferometer setup used to make the dispersion measurements.

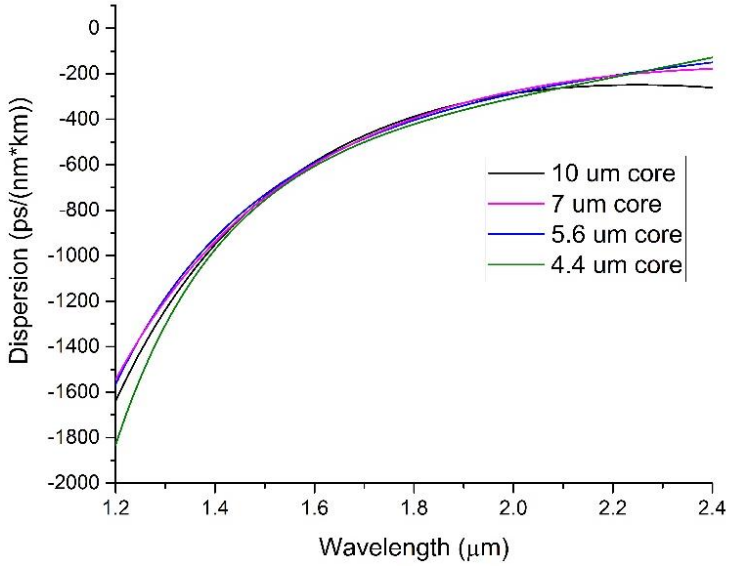

Figure 27. Dispersion of the 10, 7, 5.6 and 4.4 µm core fibers obtained from preform B.

In the range of measurement, the dispersion curves of the various fibers are very similar. We can notice a trend showing that the dispersion increases with the core size above 1.5 µm. This should be regarded as an experimental error, and we should consider the dispersion to be very close in this range. Indeed, the inherent multimode nature of the examined fibers at these wavelengths makes the excitation of the fundamental mode alone impossible, due to the various modes excited during the measurement causing a margin of error. Nevertheless, for near-infrared and mid-infrared, the simulation is in well accordance with the experimental data, as shown in Figure 28.

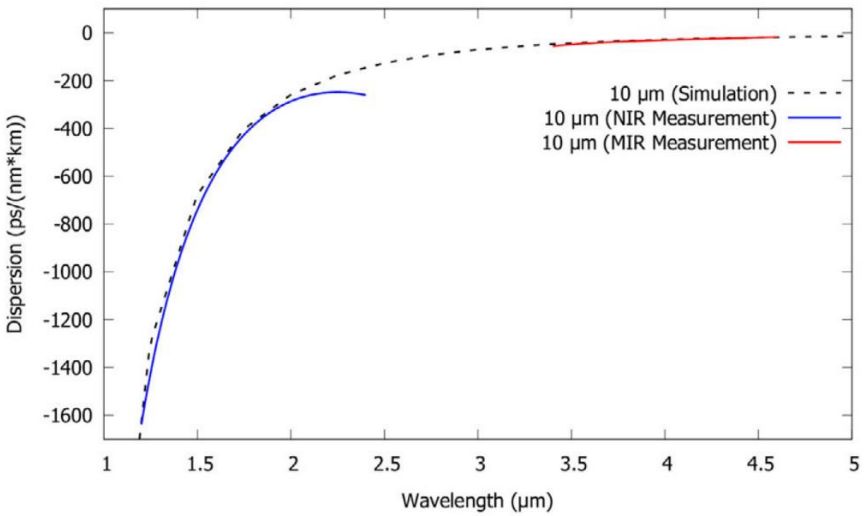

Figure 28. Comparison of the dispersion profile of the 10 µm core fiber simulated from preform B and the one measured from 1.5 to 2.4 and 3.4 to 4.6 µm.

The 20 and 40 µm core fibers were impossible to measure due to the important number of modes excited, which produces a lot of interferences in a close range, making it impossible to distinguish the equalization wavelength of the fundamental mode. Due to the large size of the cores, intermodal interferences also made the measurement too delicate to be performed.

3.1.7 Numerical aperture measurement

The Numerical Aperture (NA) was measured using a Continuous Wave (CW) 1550 nm laser and a near-infrared sensitive camera as a detector. Inputting the intensity profile for different distances between the output of the fiber and the camera's sensor, we calculated the divergence of the beam as a function of the distance of the camera to calculate fibers' NA (Table 3). The NA is almost the same for all fibers, with a slight tendency to increase when increasing the core size. This could also be an error due to different excitations of the cores.

Table 3. Numerical aperture calculated for the 4.4, 5.6, 7, 10 and 20 µm core fibers obtained from preform B.

Fiber	**4.4 µm core**	**5.6 µm core**	**7 µm core**	**10 µm core**	**20 µm core**
Numerical aperture (+/- 0.1)	0.5	0.55	0.54	0.54	0.57

3.1.8 Scanning electron microscope imaging and EDS

SEM and EDS measurements were performed on samples from all the fibers drawn. As visible in Figure 29, no defects at the core-clad interface or between the elements of the core were visible, even with the resolution of this technique which confirms the high quality of the fiber drawing. Using EDS along a line

passing through the core, it is possible to clearly distinguish the compositional variation due to the structured nature of the core, as shown in Figures 30 and 31 for preforms A and B respectively. The parabolic composition profile was observed into the core of the three fibers with a diameter of 10, 20 and 40 µm as shown Figure 30 and 31. We can see that the concentration of arsenic (blue line) presents a parabolic distribution into the core, the highest concentration being at the center of the core. The concentration of germanium (purple line) also has a parabolic profile decreasing at the center of the core. This shows that the drawing temperature and tension of the fiber was appropriate allowing us to keep the initial structure of the preform. Composition profile of the 10 µm core fiber produced from the preform B, drawn at high temperature (359 Celsius degrees), could not be observed. This is attributed to the higher diffusion of the different components of the core (Ge-5 and Ge-10 chalcogenides rods), causing the loss of the core structure. Too low tension/high temperature should be avoided for this type of composition considering the obvious structure deformations, as shown on Figure 32. The higher diffusion leads to a homogeneous core composition, inevitably leading to a refractive index equal all along the fiber transverse section.

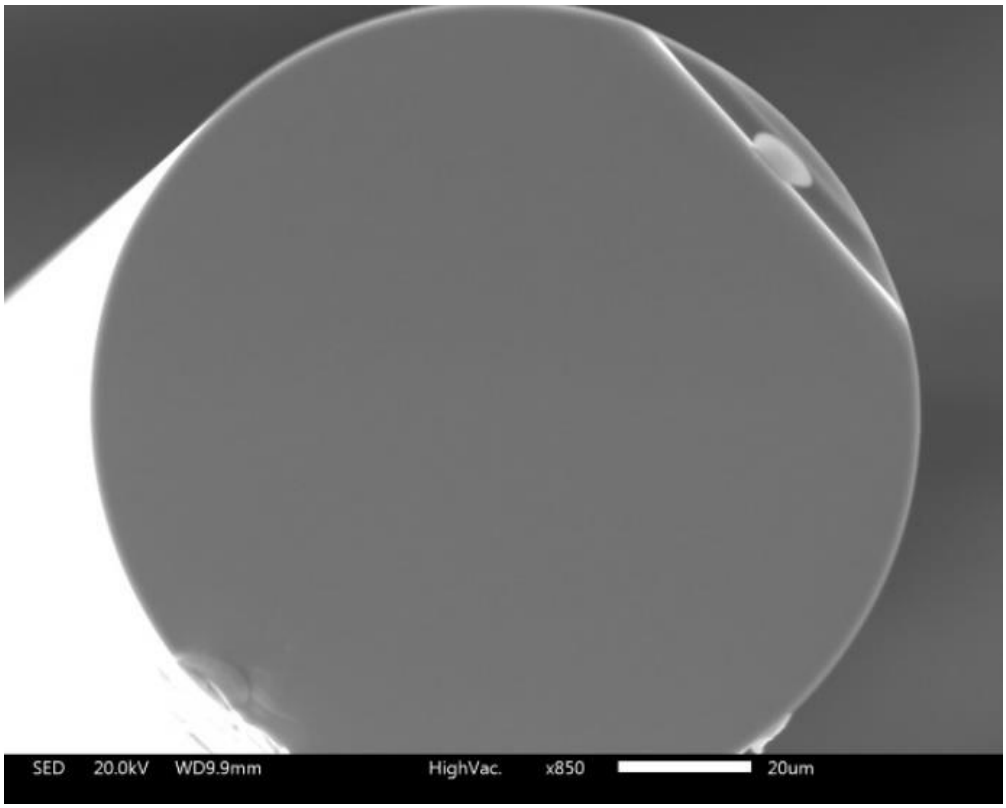

Figure 29. SEM image of a section of the 20 µm core fiber obtained from preform B.

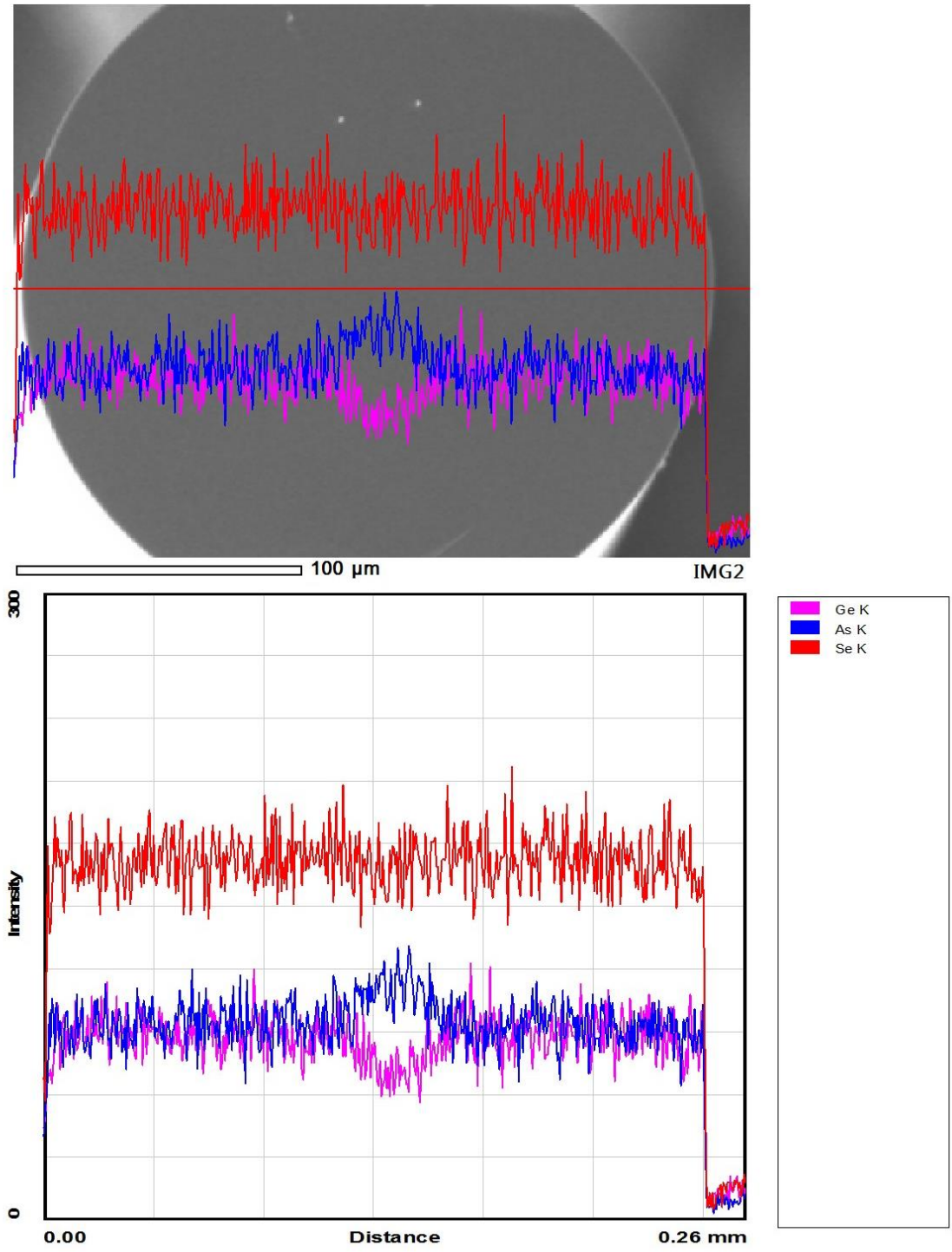

Figure 30. SEM image of a section of the 40 µm core fiber obtained from preform A along with the line scan of the concentration of Ge, As and Se obtained by EDS.

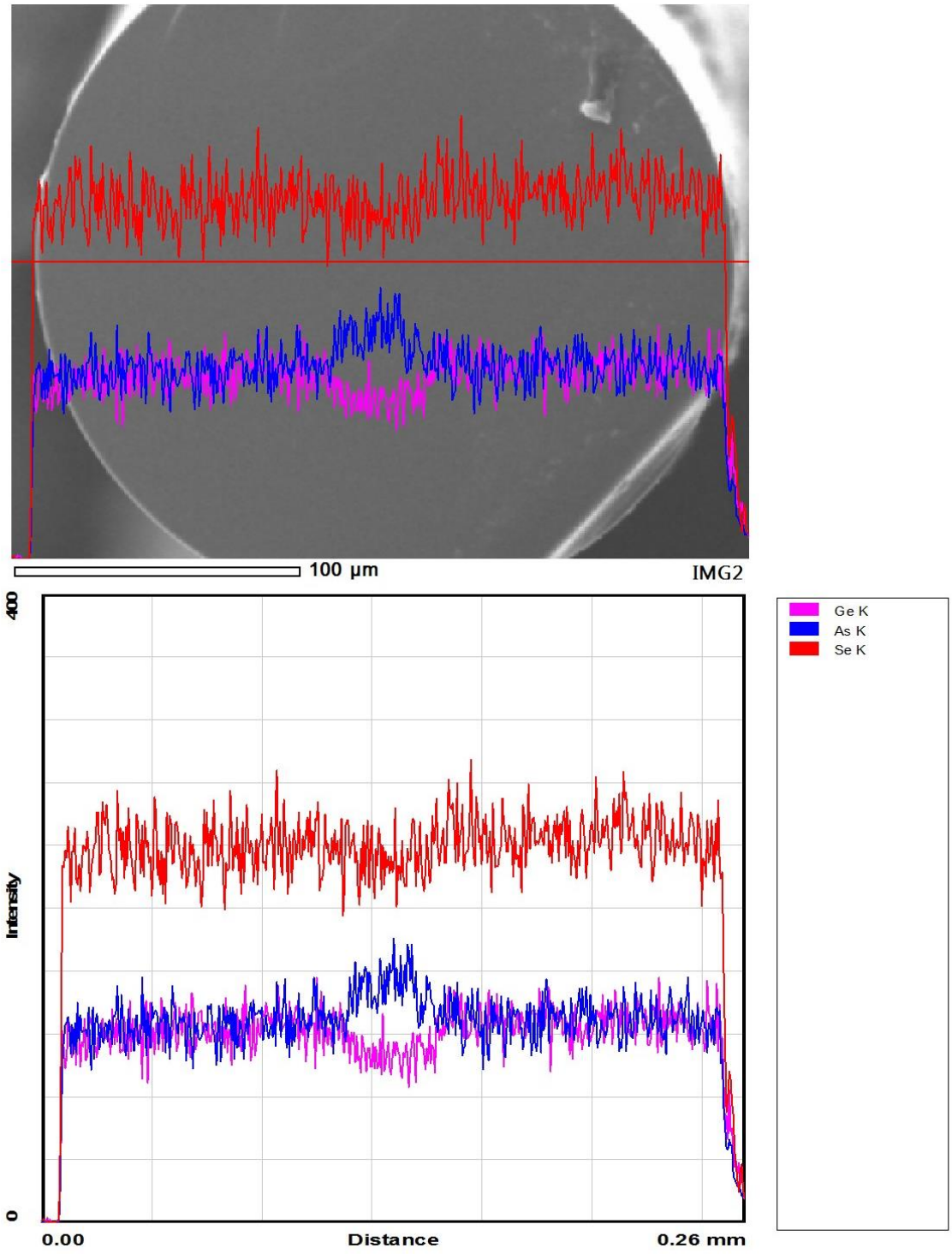

Figure 31. SEM image of a section of the 40 µm core fiber obtained from preform B along with the line scan of the concentration of Ge, As and Se obtained by EDS.

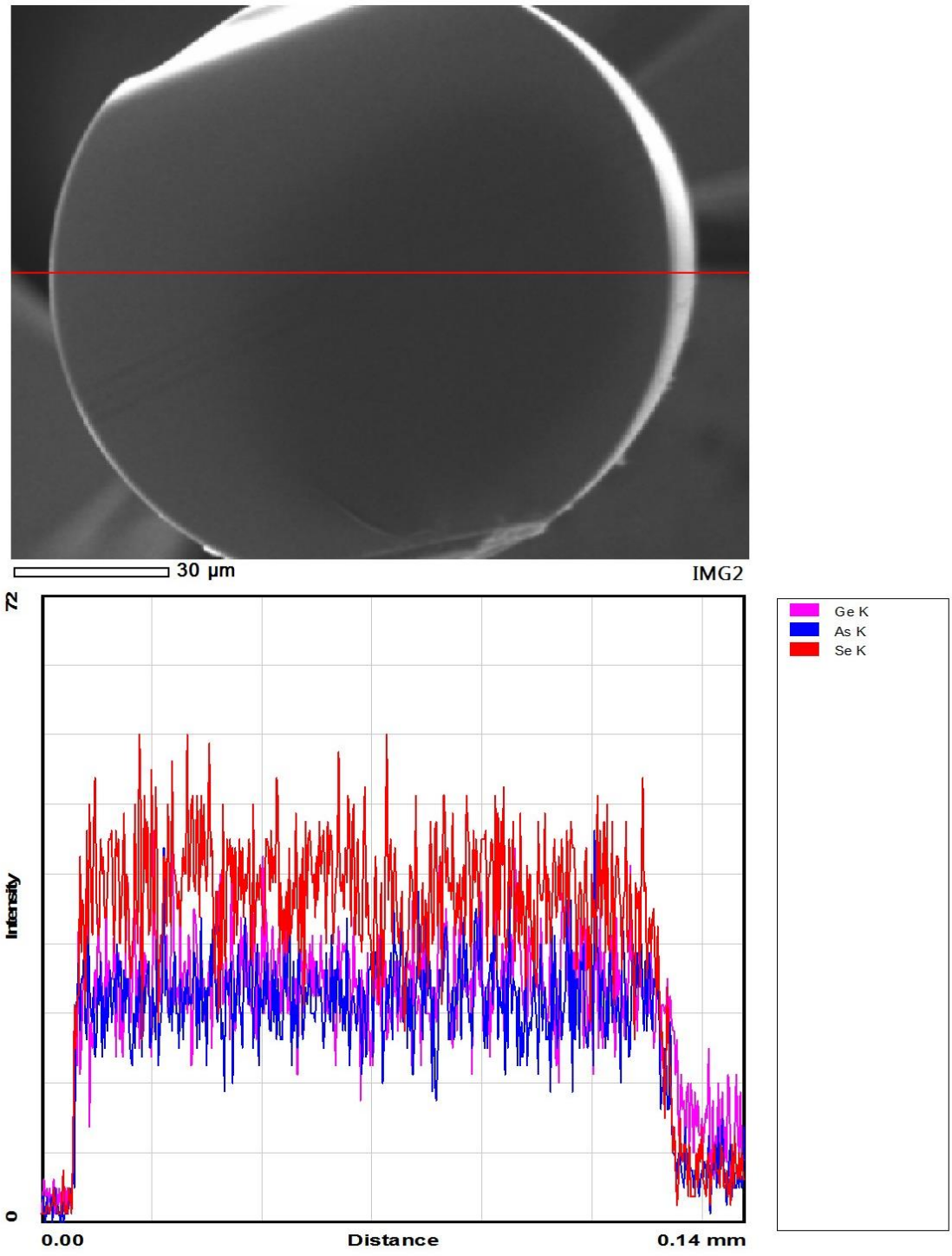

Figure 32. SEM image of a section of the 10 µm core fiber obtained from preform B with heavily high temperature and low tension along with the line scan of the concentration of Ge, As and Se obtained by EDS.

4. Chalcogenides graded index microlenses

As a proof of concept, we tried to produce chalcogenides graded index microlenses from the preform B used to make the nGrins presented previously in this chapter. The growing needs of micro-optics for various industries, in particular in the mid-infrared range, has led to recent research effort in alternative ways to produce micro-optic components. In particular, the injection systems used for mid-IR applications are particularly interesting to couple light at the input and output of a mid-IR optical fiber. Chalcogenides glasses and their exceptional transmission up to 24 µm and extremely high nonlinearity make them the perfect candidate for the production of such optics.

It also allows a fast and low-cost production of micro-optic elements compared to the other methods traditionally used to produce micro-lenses. This approach allows to exploit the light-bending properties of graded index profiles to progressively redirect light rays to the focal point (Figure 33) [32].

To produce graded index microlenses from chalcogenide glasses, 80, 120 and 160 µm core fiber canes were drawn at the University of Rennes 1 from the preform A and B developed previously to make nanostructured core chalcogenides fibers. Unsuccessful attempts were done with 40 µm core fiber, but the carving method as well as the small size of the fiber were inappropriate for this method.

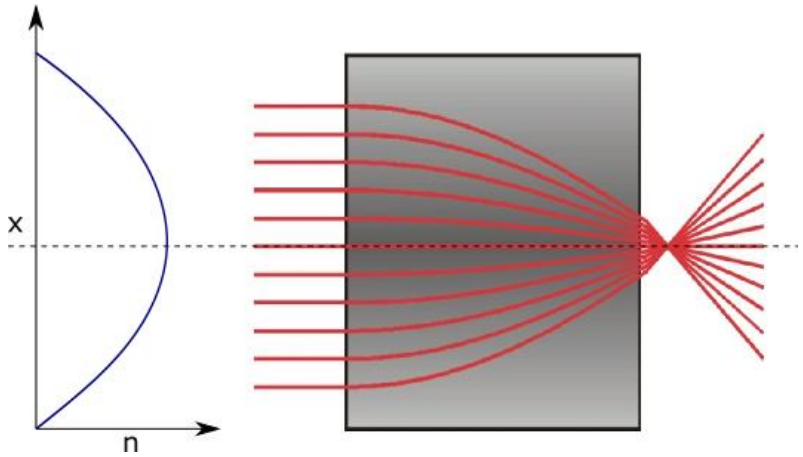

Figure 33. Schematics of the functioning principle of graded index microlenses.

4.1 Fabrication

As a base to produce microlenses, canes with a graded index core were drawn with the same method used for the fabrication of the graded index fibers presented in section 3. Three core diameters were chosen for this study: 80, 120 and 160 µm, produced from preform B structure, corresponding to a total diameter of 500, 700 and 1000 µm respectively with the cladding. Once we have determined the target diameters, the corresponding thickness is calculated to have the focal point outside of the microlenses, at a distance below a quarter pitch, which corresponds to a quarter of the length of a full sinusoidal period of the light entering the lens perpendicularly to its surface and propagating through the lens as shown on Figure 33. The pitch can be calculated such as:

$$\Lambda = \frac{2\pi}{\sqrt{g}}$$

where g is the gradient constant describing the shape of the refractive index variation on the lens surface [33]. The structure of the lenses has been designed to have a parabolic RI profile along the core which allow us to express the constant g such as:

$$g = \frac{2(n_{max} - n_{min})}{n_{max}.r^2}$$

The distance between the lens surface output and the focal point, called working distance (WD), can be expressed as follow:

$$WD = f.\cos(\sqrt{g}.l)$$

where l is the lens thickness, and f is the focal length such as:

$$f = \frac{1}{n_{max}.\sqrt{g}.\sin(\sqrt{g}.l)}$$

Due to the uncertainty of the thickness among the polished samples, we obtain various thicknesses averaging the initial thickness target at +/-10 nm.

The obtained canes were then cut into 10 cm long rods, which were then cut into three equal pieces, glued to silica plates using epoxy resin with a theoretical gluing force of 3000 N/cm^2 approximately (Figure 34a). Grooves were preemptively carved in the plates to ensure a perfect alignment of the rods and ease the carving step. An 18-minute heat treatment at 140 °C was performed to further harden the resin, reaching a theoretical force of 3400 N/cm2. The plates were then cut at equal spacing of 400 µm, with an automatized high pressure water cutting machine leading to slices of unpolished lenses, as shown Figure 34b.

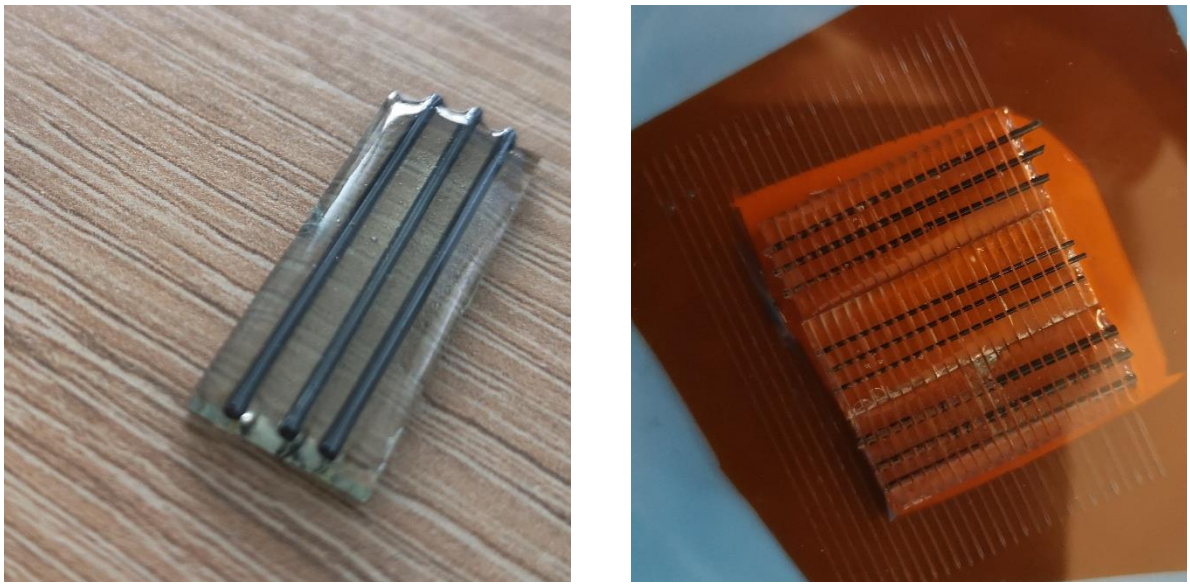

Figure 34. (a) Micro rods carved with epoxy on a silica plate before the cutting (160 µm core rods are pictured here). (b) lenses of different diameters cut with the high pression water jet cutting machine.

The resulting embedded micro-lens preforms are then glued with hot epoxy onto holders heated at 135 °C and reduced to the target thickness by polishing them on both sides (Figure 35). While the lenses are

normally mechanically removed from the epoxy resin after detaching them from the holders, it was decided to let them embed in the resin due to the mechanically fragile nature of chalcogenides glass. This is not detrimental to the measurements and allows to obtain easy to handle microlenses. After polishing, we heat up the holder again at 135 °C to remove and clean the lenses. The parameters of the obtained lenses are summarized in Table 4. The reason for the difference between the target and real thicknesses lies in the technical difficulty of achieving micrometric precision in the polishing step of production.

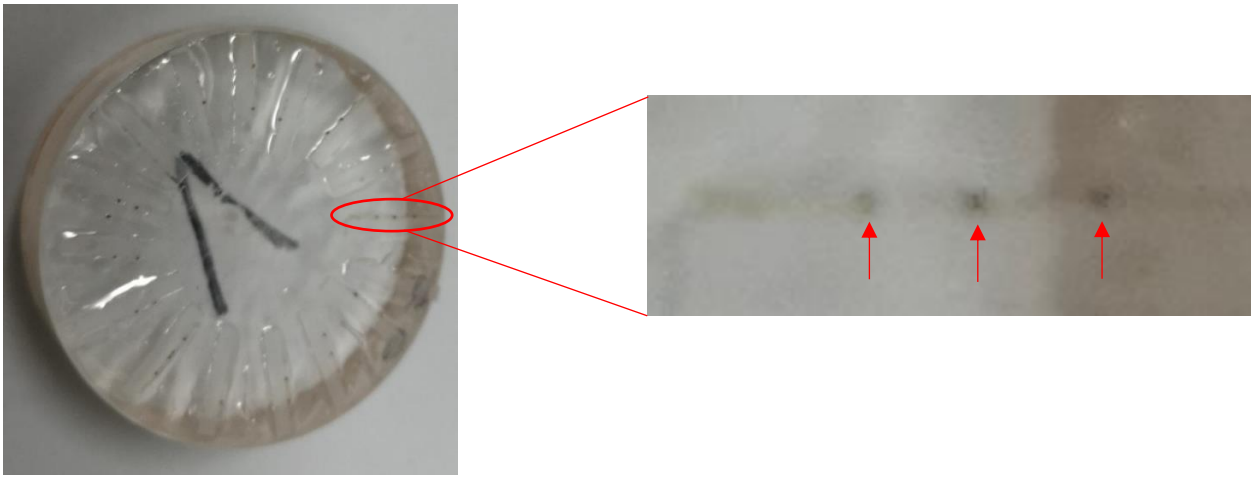

Figure 35. Micro-lenses holder used for the optical polishing with a zoom showing the lenses, of the final result after polishing (red arrows).

Table 4. Parameters of the nGrin chalcogenide lenses produced from preform B, with a core diameter of 80, 120 and 160 µm.

Core size (µm)	External size (µm)	Q-pitch (µm)	WD for l = 0.22 (um)	WD for l = 0.1_ (um)
80	500	249	11	81
120	750	374	17	121
160	1000	438	22	161

To verify the validity of this new method to fabricate chalcogenide lenses, microscope pictures of the micro lenses produced were taken. The structure, as shown on Figure 36, is well-preserved despite the heavy process involved for its production. We can clearly distinguish the structure initially simulated and stacked, which proves the process to be highly effective for the fabrication of chalcogenides micro lenses.

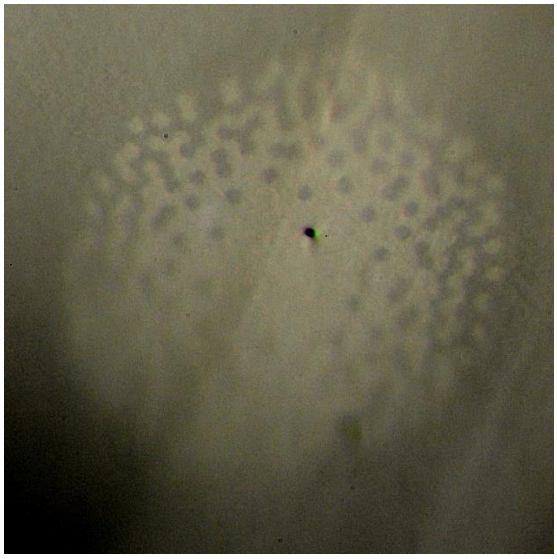

Figure 36. Microscope picture taken microscope showing the 160 µm core diameter chalcogenide micro-lens structure.

Conclusion

In this chapter, we have demonstrated the first example of chalcogenide graded index fibers [15], with a nanostructured core composed by elements of different refractive indices, producing a parabolic refractive index profile along the core. The chalcogenides glasses used within the Ga-As-Se system have proven to be stable enough to withstand the multithermal processes involved in the production of these all-solid nGRIN fibers. We have produced various fibers with core sizes ranging from 4.4 to 160 µm. It has shown to be a highly effective way to shape the dispersion profile to comply with the constraints caused by the nature of chalcogenides glasses, mostly because of the zero-dispersion wavelength in the mid-infrared being located up to 7+ µm, making the supercontinuum generation pump solutions difficult to find. By changing the nanostructuration, we can get a flat dispersion profile or a saddle shape, allowing us to effectively exploit the non-linearity of the chalcogenide glass developed over a wide range of wavelengths. Despite the high losses, light transmission was achieved in the fiber from 1 to 12 µm. A direct link between attenuation and core size was observed.

As a proof of concept, we have shown that we could produce micro lenses of various diameters based on the stack and draw method. The high versatility of this process allows the production of low-cost graded index chalcogenide-based lenses for applications up to 17 µm. The microlenses produced will be measured at the University of Rennes 1 in the future.

References

[1] H. Guo, H. Zhang, L. Liu, X. Xiao, G. Farrell, “Industrial, Medical and Military Applications of Fluoride and Chalcogenide Glass Fibers”, Mid-Infrared Fluoride and Chalcogenide Glasses and Fibers. Progress in Optical Science and Photonics, vol 18. Springer, Singapore (2022). https://doi.org/10.1007/978-981-16-7941-4_9

[2] J. Keirsse, C. Boussard-Plédel, O. Loreal, O. Sire, B. Bureau, B. Turlin, P. Leroyer, J. Lucas, “Chalcogenide glass fibers used as biosensors”, Journal of Non-Crystalline Solids, Volumes 326–327, pp430-433 (2003). https://doi.org/10.1016/S0022-3093(03)00434-4

[3] J.S Sanghera, I.D Aggarwal, “Active and passive chalcogenide glass optical fibers for IR applications: a review”, Journal of Non-Crystalline Solids, Volumes 256–257, pp6-16 (1999). https://doi.org/10.1016/S0022-3093(99)00484-6.

[4] Y. Wu, M. Meneghetti, J. Troles, and J-L. Adam, "Chalcogenide Microstructured Optical Fibers for Mid-Infrared Supercontinuum Generation: Interest, Fabrication, and Applications", *Applied Sciences* 8, no. 9, pp1637 (2018). https://doi.org/10.3390/app8091637

[5] P. Lucas, C. Boussard-Pledel, A. Wilhelm, S. Danto, X. H. Zhang, P. Houizot, S. Maurugeon, C. Conseil, B. Bureau, “The Development of Advanced Optical Fibers for Long-Wave Infrared Transmission.”, *Fibers*, *1*, pp110-118 (2013). https://doi.org/10.3390/fib1030110

[6] L. Calvez, H-L. Ma, J. Lucas, X.H. Zhang, ‘Glass and glass-ceramics transparent from the visible range to the mid-infrared for night vision", *International Journal of Nanotechnology (IJNT), Vol. 5, No. 6/7/8, (2008).*

[7] X.H. Zhang, Y. Guimond, Y. Bellec, “Production of complex chalcogenide glass optics by molding for thermal imaging”, Journal of Non-Crystalline Solids, Volumes 326–327, pp519-523 (2003). https://doi.org/10.1016/S0022-3093(03)00464-2.

[8] T. Cheng, K. Nagasaka, T. H. Tuan, X. Xue, M. Matsumoto, H. Tezuka, T. Suzuki, and Y. Ohishi, "Mid-infrared supercontinuum generation spanning 2.0 to 15.1 µm in a chalcogenide step-index fiber.", Opt. Lett. 41, pp2117- 2120 (2016).

[9] J. Troles, L. Brilland, C. Caillaud, and J-L. Adam. “Original designs of chalcogenide microstuctured optical fibers”. In: Advanced Device Materials 3.1, pp7–13 (2017).

[10] J. Knight. “Photonic crystal fibres”. *Nature* 424, pp847–851 (2003). 10.1038/nature01940

[11] V. V. Ravi Kanth Kumar, A. K George, W. H. Reeves, J. C. Knight, P. St. J. Russell, F.G. Omenetto, and A. J Taylor, "Extruded soft glass photonic crystal fiber for ultrabroad supercontinuum generation," Opt. Express 10, 1520-1525 (2002)

[12] F. Deiss, N. Sojic, D. J. White, *et al.* Nanostructured optical fibre arrays for high-density biochemical sensing and remote imaging.”, *Anal. Bioanal. Chem.* 396, pp53–71 (2010). https://doi.org/10.1007/s00216-009-3211-0

[13] D. J. White and P. R. Stoddart, "Nanostructured optical fiber with surface-enhanced Raman scattering functionality.", Opt. Lett. 30, pp598-600 (2005).

[14] X. Yu et al., "Silica-Based Nanostructure Core Fiber.", IEEE Photonics Technology Letters, vol. 20, no. 2, pp162-164 (2008). doi: 10.1109/LPT.2007.912486.

[15] M. Meneghetti, X. Forestier, C. R. Petersen, R. Kasztelanic, M. Klimczak, O. Bang, R. Buczyński. and J. Troles, "Graded Index Chalcogenide Fibers with Nanostructured Core.", Adv. Photonics Res. 2, pp2000091 (2021). https://doi.org/10.1002/adpr.202000091

[16] Xunsi Wang, Qiuhua Nie, Tiefeng Xu, Liren Liu, "A review of the fabrication of optic fiber," Proc. SPIE 6034, ICO20: Optical Design and Fabrication, 60341D (2006). https://doi.org/10.1117/12.668147

[17] A. Anuszkiewicz, R. Kasztelanic, A. Filipkowski et al., "Fused silica optical fibers with graded index nanostructured core.", Sci. Rep. 8, pp1–13 (2018).

[18] A. Anuszkiewicz, M. Bidus, A. Filipkowski et al., "Experimental analysis of axial stress distribution in nanostructured core fused silica fibers.", Opt. Mater. Express 9, pp4370.

[19] F Hudelist, R Buczynski, A. J. Waddie, and M. R. Taghizadeh. "Design and fabrication of nanostructured gradient index microlenses.", Optics express 17.5, pp3255–3263 (2009).

[20] R. Buczynski, M. Klimczak, T. Stefaniuk, R. Kasztelanic, B. Siwicki, G. Stepniewski, J. Cimek, D. Pysz, and R. Stepien. "Optical fibers with gradient index nanostructured core", Optics express 23.20, pp25588–25596 (2015).

[21] B. Siwicki, A. Filipkowski, R. Kasztelanic, M. Klimczak, and R. Buczynski. "Nanostructured graded-index core chalcogenide fiber with all-normal dispersion– design and nonlinear simulations", Optics express 25.11, pp12984–12998 (2017).

[22] X. Forestier, T. Karpate, G. Huss,V. Tombelaine, G. Stepniewski, A. Anuszkiewicz, R. Kasztelanic, A. Filipkowski, D. Pysz, M. Klimczak, R. Buczynski, "Supercontinuum generation in nanostructured core gradient index fibers.", *Appl Nanosci* 10, pp1997–2005 (2020). https://doi.org/10.1007/s13204-020-01319-9

[23] R. Buczynski, M. Klimczak, T. Stefaniuk, R. Kasztelanic, B. Siwicki, G. Stepniewski, J. Cimek, D. Pysz, and R. Stepien. "Optical fibers with gradient index nanostructured core", Optics express 23.20, pp25588–25596 (2015).

[24] N. M Israelsen, C. R Petersen, A. Barh, D. Jain, M. Jensen, G. Hannesschläger, P. Tidemand-Lichtenberg, C. Pedersen, A. Podoleanu, and O. Bang. "Real-time high-resolution mid-infrared optical coherence tomography", Light: Science & Applications 8.1, pp11 (2019).

[25] E. A. Anashkina and A. V. Kim, "Numerical Simulation of Ultrashort Mid-IR Pulse Amplification in Praseodymium-Doped Chalcogenide Fibers", *Journal of Lightwave Technology*, vol. 35, no. 24, pp5397-5403 (2017). doi: 10.1109/JLT.2017.2775864.

[26] C. Poudel and C. F. Kaminski, "Supercontinuum radiation in fluorescence microscopy and biomedical imaging applications," J. Opt. Soc. Am. B 36, A139-A153 (2019)

[27] J. M. Dudley, G. Genty, S. Coen, “Supercontinuum generation is photonic crystal fiber”. Rev. Mod. Phys. 78, pp1135-1184 (2006). 10.1103/RevModPhys.78.1135.

[28] L.C. Van, A. Anuszkiewicz, A. Ramaniuk, R. Kasztelanic, K.X. Dinh, V.C. Long, M. Trippenbach, R. Buczynski, “Supercontinuum generation in photonic crystal fibres with core filled with toluene”, J. Opt. 19 (2017).

[29] M. Meneghetti, C. Caillaud, R. Chahal, E. Galdo, L. Brilland, J-L. Adam, and J. Troles, "Purification of Ge-As-Se ternary glasses for the development of high quality microstructured optical fibers." *Journal of Non-Crystalline Solids* 503 pp84-88 (2019).

[30] V. Q. Nguyen, J. S. Sanghera, B. Cole, P. Pureza, Frederic H Kung, and Ishwar D Aggarwal, “Fabrication of arsenic sulfide optical fiber with low hydrogen impurities”, Journal of the American Ceramic Society 85.8, pp2056–2058 (2002).

[31] H. G. Dantanarayana, N. Abdel-Moneim, Z. Tang, L. Sojka, S. Sujecki, D. Furniss, A. B. Seddon, I. Kubat, O. Bang, and T. M. Benson, “Refractive index dispersion of chalcogenide glasses for ultra-high numerical-aperture fiber for mid-infrared supercontinuum generation”, Optical Materials Express 4.7, pp1444–1455 (2014).

[32] S. H. Wang, C. J. Tay, C. Quan, and H. M. Shang, “Collimating of diverging laser diode beam using graded-index optical fiber”, Optics and lasers in engineering 34.2, pp121–127 (2000).

[33] R Buczynski, A Filipkowski, B Piechal, H. T. Nguyen, D Pysz, R Stepien, A Waddie, M. R. Taghizadeh, M Klimczak, and R Kasztelanic, “Achromatic nanostructured gradient index microlenses.”, Optics express 27.7, pp9588–9600 (2019).

Chapter 5: Supercontinuum generation in nanostructured core all-solid photonic crystal fibers

High-brightness broadband light sources in science are of increasing importance due to applications in optical coherent tomography [1], frequency combs generation for high precision metrology [2], and in spectroscopy, LIDAR, biomedical imaging and microscopy [3]. Imaging cancer tissues [4], as well as chemical sensing [5] for example need increasing quality of coherent light sources to gain into precision. Optical fibers are particularly adapted to supercontinuum generation due to their strong light confinement, as well as for the possibility to design the chromatic dispersion, allowing to match the nonlinear optical properties of the medium more easily with the intended pump lasers [6-8]. Coherent and spectral properties of fiber-based supercontinuum can be widely modified to fulfill various application requirements [9-11]. In 2000, Ranka et al. [12] demonstrated for the first-time supercontinuum generation in photonic crystal fibers (PCFs). Photonic Crystal fibers have shown to be a disruptive step forward in the field for the generation of supercontinuum because of relevant characteristics of a PCF, i.e., most notably the chromatic dispersion profile which can be modified by the PCF lattice geometry [8]. PCFs have been reported with various designs, such as hexagonal lattice structure, suspended core structure, enabling the engineering of their properties such as dispersion, confinement losses, effective mode areas, and nonlinearity improving the efficiency and control of the supercontinuum generation and its dynamics compared classic, step-index fibers. Supercontinuum generation in PCFs has been intensively studied last decades leading to applications involving wavelengths from the ultraviolet [13], the visible up to the mid-infrared [14-15]. In this context, various glass families are investigated due to their drastically different optical properties such as the wavelengths range and the nonlinear optical properties of the glasses as explained in Chapter 1. The most common and industry-accepted standard for optical fiber development, including PCFs drawn by various methods like extrusion or the stack and draw, is the silica glass due to its outstanding physico-chemical properties allowing telecommunication systems applications, requiring good mechanical and durability properties, as well as bio-imagery and sensing systems, making it the glass of choice for biomedical sensing applications [16]. For supercontinuum generation in the mid-infrared wavelengths, various soft glasses such as tellurites, fluorides or chalcogenides are considered for “classic” step-index fibers, index guiding PCFs or nGRINs, as these glasses have broad transmission windows exceeding that of silica. The motivation to develop new concept of optical fibers, to make high quality, coherent supercontinuum light sources with characterized with ease of use by users without training in physics is growing, which is why all-solid glass fibers are interesting from the applications point of view [17-18]. Indeed, it is a robust solution for industry due to its all-solid nature, offering good mechanical properties compared to holey fibers obtained by extrusion as explained in previous chapters. It is especially true for non-specialist applications such as medical professionals and technicians requiring reliability and ease of use.

Among different approaches, we propose the use of nanostructured graded-index fiber (nGRIN) as a novel material for supercontinuum generation. Indeed, graded-index fiber, commonly fabricated by Modified

Chemical Vapor Deposition (MCVD) or ion exchange techniques [19], do not allow the use of complex multicomponent glasses and make the development of arbitrary refractive index profile graded-index core fibers virtually impossible. Recently, a new type of structuration demonstrated promising possibilities for dispersion management and the fabrication of nGRIN fibers with arbitrarily shaped index profiles [20-22].

As explained in chapter 4, EMT was used to produce the gradient refractive index profile desired, depending on the pattern arrangement. This method gives a good versatility for dispersion, index distribution profile, polarization and modal engineering [23]. Other advantages include the possibility to develop multicore fibers, and large mode area (LMA) fibers, important in the context of power scaling. Our group has demonstrated LMA fibers using the nGRIN approach before [24-25]. Multicore fiber supercontinuum generation and soliton shifting has also been recently reported using standard stacking of multicore photonic crystal fibers [26]. The nano-structuration of all-solid fibers also gives a clear mechanical advantage compared to holey fibers for example and is logically less prone to energy related damages, due to its “volume glass” nature. We recently introduced the concept of silica single mode fiber [27]. We also demonstrated theoretical studies with a potential mid-IR graded index fiber [21]. We also validated that this complex structure does not suffer from internal stresses due to the stacking process.

In this work, we validate the use of such nanostructured core fibers for robust all-solid fibers for near-infrared supercontinuum generation, where our nGRIN fiber is used with industry-accepted components in terms of commercial supercontinuum lasers. Chiefly we use a standard, low cost 1 ns pulsed laser diode around 1550 nm as the pump source. We begin with a brief description of the fiber used, including its design, fabrication and linear, as well as nonlinear characteristics. We then go on to report and discuss experimental results on supercontinuum generation. Spectral broadening was observed from 1400 nm to 2300 nm, which is supported with an interpretation of these experimental results using a numerical model based on nonlinear Schrödinger equation.

In a second time, due to the success of SGC in silica fiber for visible and near IR applications using nanosecond pulses [28], we validate the use of chalcogenides glasses for supercontinuum generation in all-solid nGRINs in the femtosecond regime [29]. The innovative present work represents a big step up from classical chalcogenide glass-based fibers, made by the extrusion method due their insufficient thermal stability. For the first time, chalcogenides glasses could be engineered into nanostructured core fibers by the stack and draw method, achieving a milestone producing versatile and robust mid-IR optical fibers for supercontinuum generation operating up to 7 µm. For this purpose, we use fibers with various core diameters made from the Ge-As-Se system used in Chapter 4 to compare it with silica nanostructured core fibers. We begin with a brief description of the fibers used, including their design, fabrication and linear, as well as nonlinear characteristics. Next, we present experimental results on supercontinuum generation supported with contributing phenomena explanation based on numerical modeling results obtained using nonlinear Schrödinger equation.

1 Nanostructured core all-solid silica fiber

1.1 Materials and design

The nanostructured fiber was previously designed and developed (prior to the author doctoral work) at the Institute of Electronic Materials Technology (ITME) [27] by the stack and draw technique, in a hexagonal lattice with a structure as shown on Figure 1. The core is composed of 2017 glass rods made of two different glasses with a different refractive index. The outer diameter of the fiber was 135.8 µm and the nanostructured core diameter was 7.15 µm.

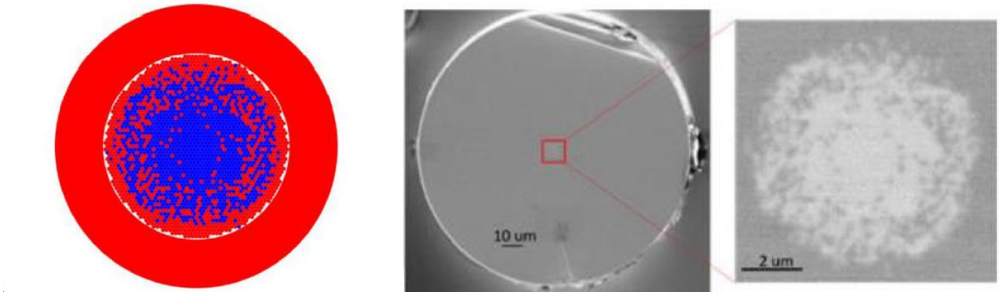

Figure 1. (a) Core structure of the developed nGRIN fiber with an effective parabolic index profile. The core is composed of 2107 glass rods of low index fused silica (red) and high index GeO2- doped silica. (b) structure of the optical fiber developed showing a well-preserved structure by electronic microscopy.

The two glasses, selected for their similar thermal properties (similar CTE, similar transition temperature and viscosity as explained chapter 3 and 4), consist in commercial fused silica glasses Ohara SK1310, selected as low refractive index glass in the core and germanium doped silica containing 4.9 %mol GeO_2 from the company Optacore, selected as high refractive index glass in the core. For the cladding, fused silica glass F300 from Heraus was selected. Their respective refractive index can be found Figure 2

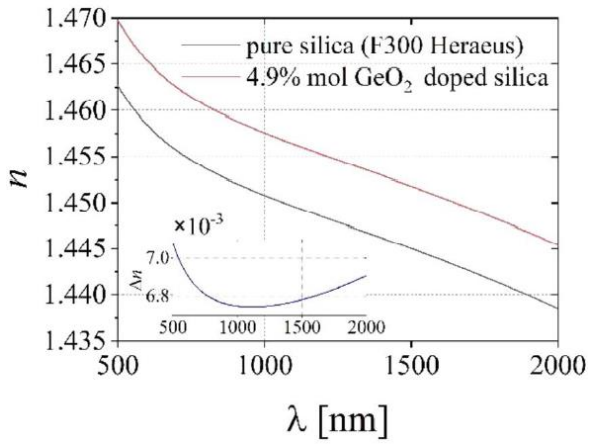

Figure 2. Material dispersion of the two glasses used to form nGRIN fiber and their refractive index difference.

The data for fused silica from Heraus was taken directly from the company data while the refractive index of Ohara SK1310 was given by the producer was n_d=1.4609 at 545 nm. The refractive index of GeO_2 doped silica was calculated using a modified Sellmeier equation as follow:

For well-known glasses such as 2 components binary silicates, we can easily calculate the refractive index using a modified Sellmeier equation [30] such as:

$$n_{(\lambda)}^2 - 1 = \sum_{i=1}^{3} \frac{[BS_i + X(BG_i - BS_i)]\lambda^2}{\lambda^2 - [CS_i + X(CG_i - CS_i)]^2}$$

With λ the wavelength in vacuum, BS_i, CS_i and BG_i, CG_i are the Sellmeier coefficients for SiO_2 GeO_2 respectively [31]. The value of X corresponds to the GeO_2 concentration in %mol (here X=4.9 %mol.

As explained in chapter 4, the nanostructuration of the core was calculated using Maxwell-Garnet effective medium approach to obtain a parabolic profile of the effective index distribution in the core of the fiber. In order to determine the final rods distribution in the core, simulated annealing was used [32-33]. The structure was well preserved during fiber drawing as shown in figure 1-b

1.2 Measurement methods

1.2.1 Chromatic dispersion

As used in chapter 4, the chromatic dispersion was measured using a Mach-Zehnder interferometer with a commercial supercontinuum laser source from LEUKOS with a spectral range spanning from 450 nm to 2400 nm. Light was coupled into the fiber using a lens (L1) with a focal length of 2 mm whereas for the output coupling from the fiber, a lens (L2) with a 4.5 mm focal length was used. Signal detection was achieved using various detectors covering from the visible to near-IR. An Optical Spectrum Analyzer (OSA) Yokogawas AQ6375B from 1200 to 2400 nm and a Czerny-Turner spectrometer from Ocean Optics, RedTide USB650 operating from 350 to 1000 nm. The Optical Path Difference (OPD) introduced by the fiber placed in the signal arm was measured as a function of the equalization wavelength. We also took into consideration the small OPD induced by the optical elements used in the setup such as lenses or filters, knowing the dispersion and the thickness of the various elements.

1.2.2 Supercontinuum generation

The silica-based fiber called MS15B3 was pumped with 1550 nm modulated amplified laser diode with a peak power of 9.4 kW delivering 1 ns pulses with a 250 kHz repetition rate. To couple the input beam into the nGRIN fiber, a 20x microscope objective was used, achieving a 37% coupling efficiency. The average power injected in the filter was 100 nW, which corresponds to 400 nJ pulse energy. The output beam was collected directly with an OSA (Yokogawa AQ6375B) as mentioned in section 1.2.1.

1.3 Results

1.3.1 Fiber characterization

1.3.1.1 Dispersion

The nGRIN fiber labeled MS15B has monotonically increasing dispersion profile with relatively low, positive slope over the entire wavelength range over which spectral broadening occurs in experiments conducted in this work, Figure 3. The zero-dispersion wavelength (ZDW) is located at 1370 nm. This enables the use of standard nanosecond pulse lasers to pump it efficiently at wavelengths, where the fiber has anomalous dispersion, which facilitates efficient supercontinuum generation. The maximum wavelength range covered in our measurements is 2400 nm, where the fiber's dispersion reaches 60 ps/nm/km.

At the short wavelength range below 1370 nm, the dispersion profile reaches − 70 ps/nm/km at a wavelength of 900 nm. Such a dispersion profile is typical for silica single-mode fibers.

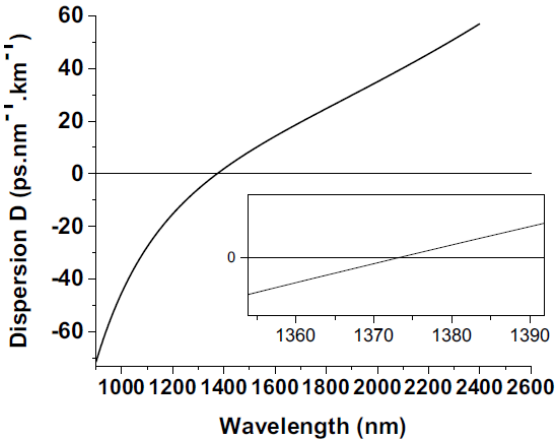

Figure 3. Measurements of chromatic dispersion (D) for the fundamental mode.

1.3.1.2 Confinement losses

The confinement losses of the nGRIN fiber were measured using the cut-back method in range 600–1700 nm starting with almost a 20 m long nGRIN fiber sample. Five consecutive cut-backs have been made down to 1.5 m. Attenuation of the whole developed nGRIN fiber series in this wavelength range remains below 50 dB/km, besides the characteristic peak around 1400 nm due to the water content in the fiber structure, where the losses reach 500 dB/km, as shown in Figure 4a. Figure 4b contains spectrum recorded at the output of the starting length of the fiber sample (19.5 m) and the shortest sample (following five cut-backs) in the measurement. This part of the experiment confirms that no additional source of pollution was introduced during the stacking of the preform. High level of the water peak is related to quality of silica rods used for fiber assembly and research-grade level of preform assembly conditions, where water level in the assembly cabinet was not reduced. The presence of water peaks may influence supercontinuum generation spectral range. The confinement losses of the fiber are not related fundamentally to the stack-and-draw method, and they can be significantly reduced when high-quality glass components are used to preform assembly in clean-room conditions, similarly to high-quality silica-based photonic crystal fibers previously reported [34].

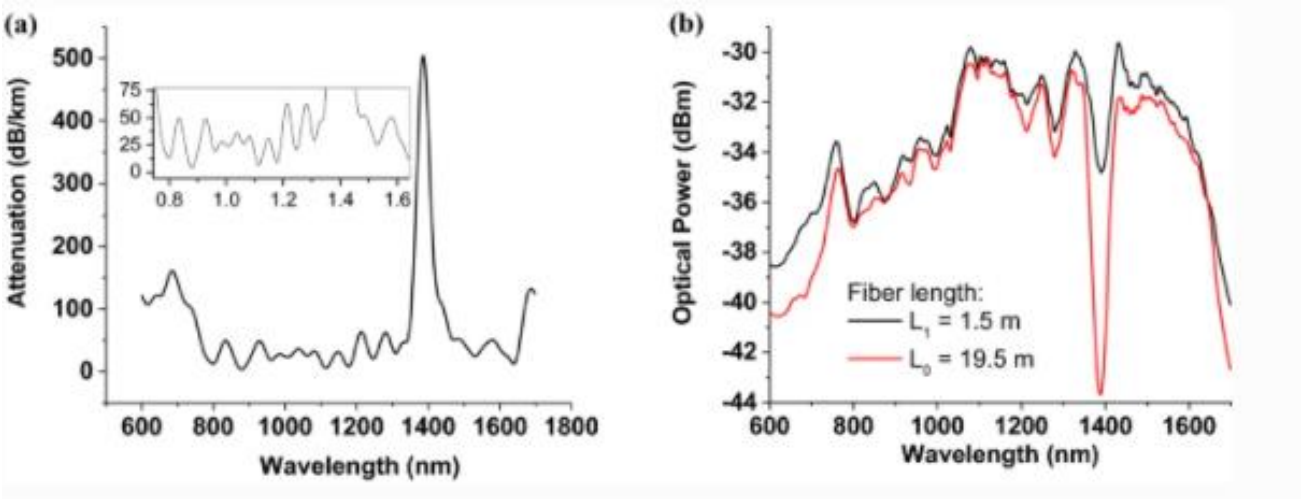

Figure 4. (a) Attenuation of MS15B3 series measured by the cut-back method over wavelength spanning from 600 to 1700 nm, (b) reference spectrum at the output of the fiber samples for the longest (starting) and the shortest (final) fiber length.

1.3.2 Supercontinuum generation in nanosecond regime

The nonlinear propagation was modeled using the general nonlinear Schrodinger equation (GNLSE). In nanosecond pulse pumping conditions, the primary nonlinear phenomenon responsible for dramatic spectral broadening of the input pulse is modulation instability (MI) [8, 35-36]. While numerical simulation of nonlinear propagation of nanosecond pulses would not be feasible to run on a standard personal computer, similar dynamics are observed under tens of picosecond pump pulses and such an approach was taken in this work. In our simulations, we input a Gaussian pulse with a temporal FWHM of 12 ps. Fiber length assumed in modeling was equal to 33.4 cm used in the following experiments. The width of the temporal window grid of the simulation was 100 ps. The input peak power assumed in the simulation was 33.3 kW, which corresponded with peak power of the laser in the experiment. The pump assumed in the modeling was operating at a wavelength of 1550 nm with a repetition rate of 250 kHz. At this wavelength, the fiber had anomalous dispersion of D = + 11.4 ps/nm/km. Frequency-dependent loss has been included in the simulations, considering the background loss level of 14.5 dB/km, a 500 dB/km water peak centered around the wavelength of 1400 nm and a gradually rising attenuation towards the long-wavelength cut-off modeled after silica single-mode fibers. Fixed value of 55 μm^2 was used for the effective mode area in our modeling [27]. For estimation of the nonlinear refractive index n_2 of this graded-index profile fiber, we used an approximate formula developed and established for a series of different Ge-doped silica single-mode fibers by Kato et al. [23]. It has been proposed there to include parameters like the maximum (Ge-doped silica) and minimum (pure silica) refractive index values, as well as effective mode areas and radial distributions of the mode field intensity. For a given dopant concentration (in case of our fiber Ge), the nonlinear refractive index can be approximated as $n_2 = (2.76 + 0.0947X)\ 10– 20\ m^2/W$, where X = 4.9 mol% stands for GeO_2 concentration in the high index silica glass rods used for the nanostructured core preform stacking. The nonlinear refractive index values obtained for our fiber using this approximation is $3.2 \times 10–20\ m^2/W$. Finally, to take into account MI as the primary supercontinuum driving mechanism under long pulse pumping, we included a one photon with random phase in each numerical

bin of the time window (one-photon- per-mode noise). A total of 20 simulations have been performed and averaged to obtain the final result.

We performed several test simulations runs to verify that, after around 20 simulations, the averaged supercontinuum spectrum did not change significantly. The time grid used in the simulation has to be wide enough to accommodate the entire initial pulse, as well as entire output pulse, which is evidenced in Figure 5 showing temporal evolution of the pump pulse from input of the fiber to its output.

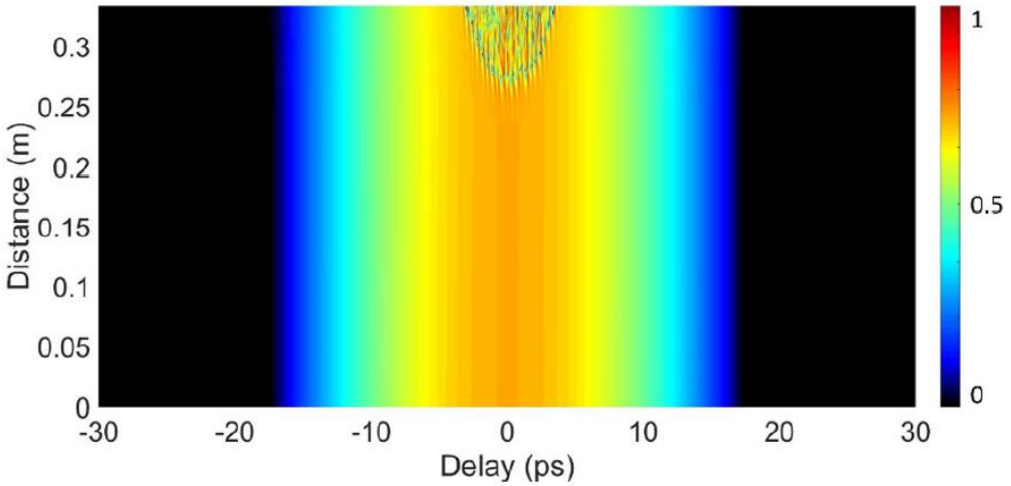

Figure 5. Temporal profile evolution of the simulated supercontinuum (picosecond) pulse along the 33.4 cm length of the fiber, colorbar: normalized intensity in linear scale (a.u.).

The implemented GNLSE model considers the effects of chromatic dispersion, Raman scattering and the nonlinear response of fused silica with germanium doping. Spectral broadening in the 'long pulse regime' leads to pulse breakup in the time domain due to the fluctuations in the noise-induced modulation instability. Further spectral broadening in the fiber is due to the high number of solitons present after wave-breaking, as can be seen in Figure 6. With the above parameters, the numerically obtained spectral broadening reached to 2300 nm at 100 mW input average power, which agrees with the results obtained experimentally and discussed below (Figure 6). The consequence of using picosecond or longer pump pulses is decoherence of the input pulse along propagation in the fiber, which is the cost of rapid and broadband spectral broadening of the pulse spectrum [35]. We verified the dominant role of MI in spectral broadening by running the nonlinear propagation simulations with one-photon-per-mode noise included and taken out of the model (Figure 6a). We note that upon excluding of the noise term from the simulation, spectral broadening is limited to a Raman scattering cascade and no continuous spectrum is observed (Figure 6b). In the absence of noise, only Raman scattering peaks are observed.

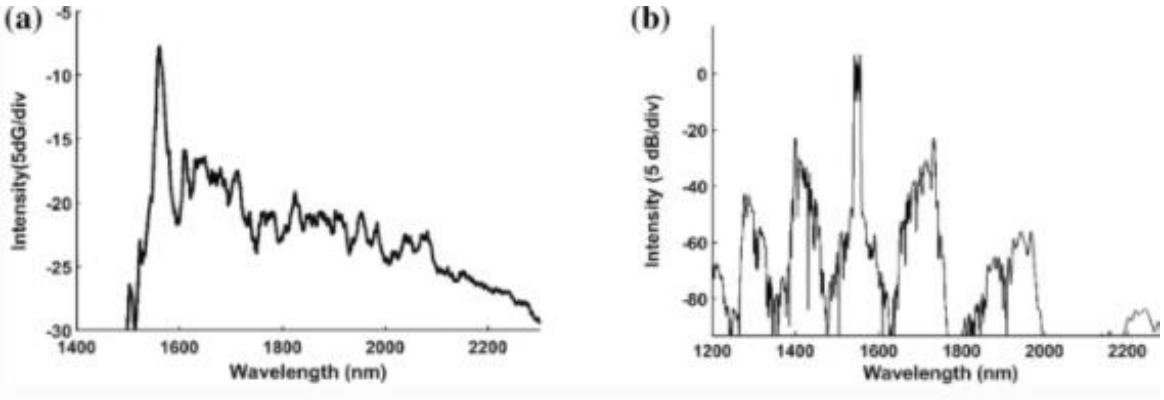

Figure 6. (a) Numerical simulation showing supercontinuum generation due to noise-driven Modulation Instability (MI), (b) Raman scattering of cascading solitons in the absence of noise seeds in the simulation.

In the experiment, we used fibers with different lengths, between around 12 cm to over 1 m. No significant spectral broadening could be obtained in samples longer than around 30 cm. At shorter sample lengths, excessive unconverted pump was recorded. While the 33.4 cm fiber sample was ultimately used out of convenience, it is reasonably close to optimal for this case. The factors which could be related to this include high attenuation of the fiber around 1400 nm due to OH absorption and non-optimal spectral separation between the ZDW at 1370 nm and the 1560 nm pump wavelength. We observed spectral broadening steadily increasing with the input energy from the pump laser diode. At 100 mW of average power, which corresponded to pulse energy of 400 nJ, a spectrum spanning 1400–2300 nm was recorded, as shown in Figure 7. As a result of the large separation of the pump wavelength from the ZDW and very poor efficiency of dispersive wave generation, as well as large attenuation of fiber around 1400 nm due to hydroxyl groups OH^- absorption, the short wavelength part of the supercontinuum is missing, as compared to e.g., state of the art visible to near-infrared commercial supercontinuum lasers (Leukos; NKTPhotonics). The red-shifted spectrum almost matches the commercial counterparts with its maximum wavelength reach. The generated supercontinuum is remarkably flat, which is a trait of modulation instability-driven broadening process [35]. Its limited spectral width of around 800 nm (between 1500 and 2300 nm, which is a sought-after spectral range in tissue optical coherence tomography (OCT) has the important advantage of significantly higher spectral power density compared to the commercial supercontinuum devices covering in excess of two octaves under the same pump power. The numerically generated supercontinuum matches the experimental result with rather limited accuracy, which we assign to limited accuracy in parametrizing the nonlinear properties of the fiber, i.e., its dispersion of nonlinearity (frequency dependence of the effective mode area). In the simulation, flat fiber nonlinearity was assumed corresponding to a fixed value of nonlinear coefficient. We note that in the physical fiber used in the experiment, expansion of the mode area with wavelength would decrease nonlinearity and limit spectral widening. This discrepancy between the experiment and simulation motivates detailed study of effective mode area dependence on wavelength in this series of fibers, which would be subject of a future study.

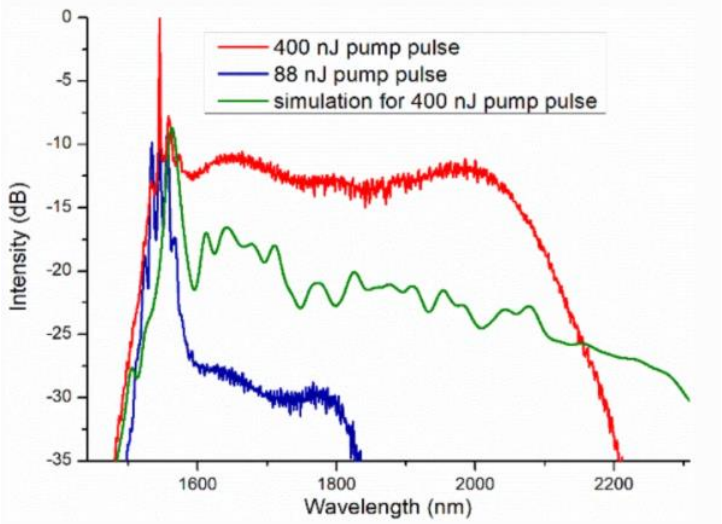

Figure 7. Supercontinuum generated in MS15B3 nGRIN fiber using a 1550 nm laser diode with 1 ns pulses and simulation results.

Considering that the used fiber is short and robust (silica, no airholes, compatible with high pulse energy pumping from a laser diode), it could be an interesting alternative for cheap, high-brightness, hand-held light sources for medical OCT applications.

Importantly, the nGRIN fiber concept has been discussed in context of broad-bandwidth chromatic dispersion engineering [21-37], which could allow improved designs of fibers for enhanced spectral coverage of MI-driven supercontinuum in a small foot-print package. Furthermore, the nGRIN concept enabling mode profile engineering would be advantageous for cascaded supercontinuum setups [38]. This is because nGRIN fibers do not have airholes and the effective mode area can be matched from the initial fiber design level to the following fiber used in the cascade.

Considering we validated the use of nanostructured core fiber for the generation of supercontinuum in near Infrared in nanosecond regime, we decided to explore the possibility to generate spectral broadening in Mid-IR fibers such as chalcogenide fibers, which transmit above 10 µm, in the femtosecond regime. For this purpose, we used the nanostructured core chalcogenide fiber developed in Chapter 4 to investigate this possibility, and pumped femtoseconds laser around the ZDW, to see if the supercontinuum generation in nanostructured core fibers could also occur with chalcogenide glasses.

2 Supercontinuum generation in femtosecond regime in the developed chalcogenide all-solid graded index nanostructured core fibers

The optical characteristics of the fiber such as the linear refractive index of both glasses as well as the dispersion profile were presented in Chapter 4. We pumped the nGRIN chalcogenide fibers previously developed in chapter 4 tapered with a core diameter of respectively 5.5, 7 and 10 µm, at 4 µm using an Optical Parametric Oscillator (OPO), with 250 femtosecond pulses. Spectral broadening was observed for the three fibers as shown in the figure below. Logically, increasing the energy of the pump increases the spectral broadening. For the 5.5 µm core fiber, spectral broadening was observed from 2 to 5.5 µm while a supercontinuum was successfully generated from 2 to 6 µm for the 7 µm core fiber (Figure 8 and 9). The

10 µm core was much less effective at generating a supercontinuum, nevertheless, broadening from 2.9 to 5.7 µm was observed (Figure 8 and 9). This could be explained by the larger surface of the core, hence a smaller energy per µm². Given the complex spatiotemporal nature of SCG in nGRIN fibers [39-40], it is difficult to predict whether coherence is preserved at these conditions but judging from the output spectrum with increasing pump power, there is no indication of modal or geometric instabilities. The fiber's output was imaged to confirm the confinement of the light in the fiber's core, as shown in Figure 9.

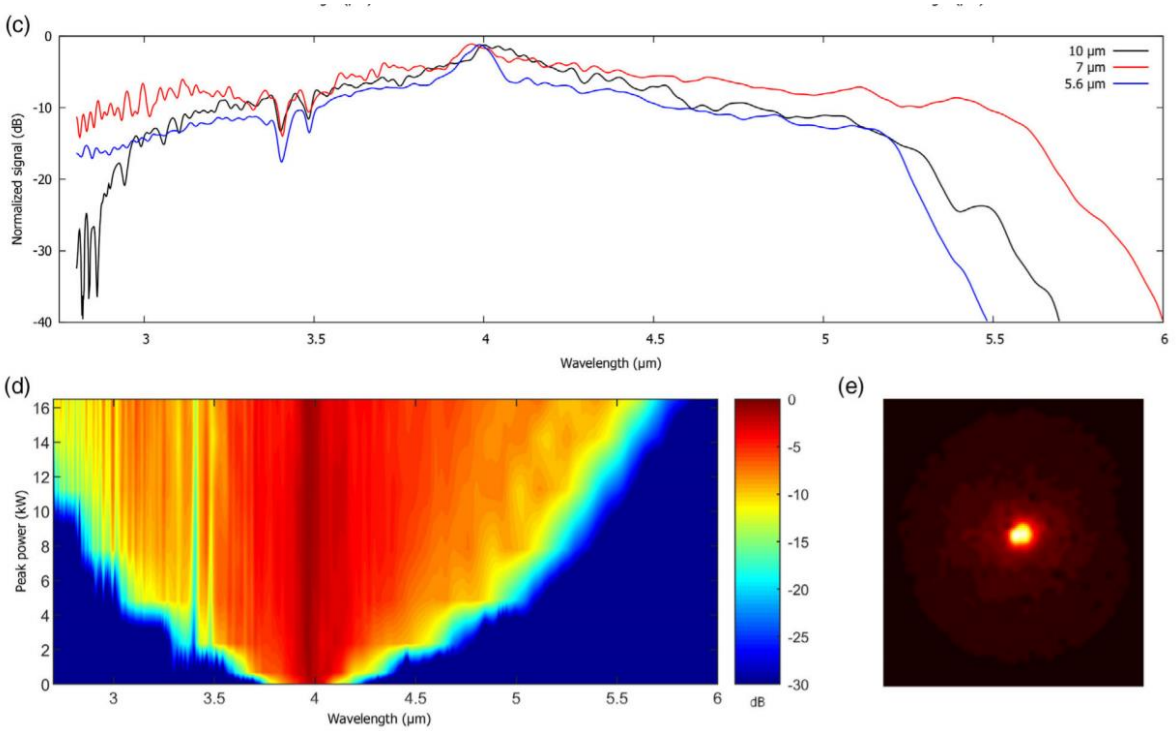

Figure 8. a) Maximum spectral broadening obtained for the 5.6, 7 and 10 um ngrin chalcogenide fiber produced, pumping with an OPO at 4um with femtosecond pulses. b) Spectral broadening dynamics with increasing pump power in the fiber with core diameter of 7 µm. c) Near field image of light confined in the fiber with core diameter of 7 µm.

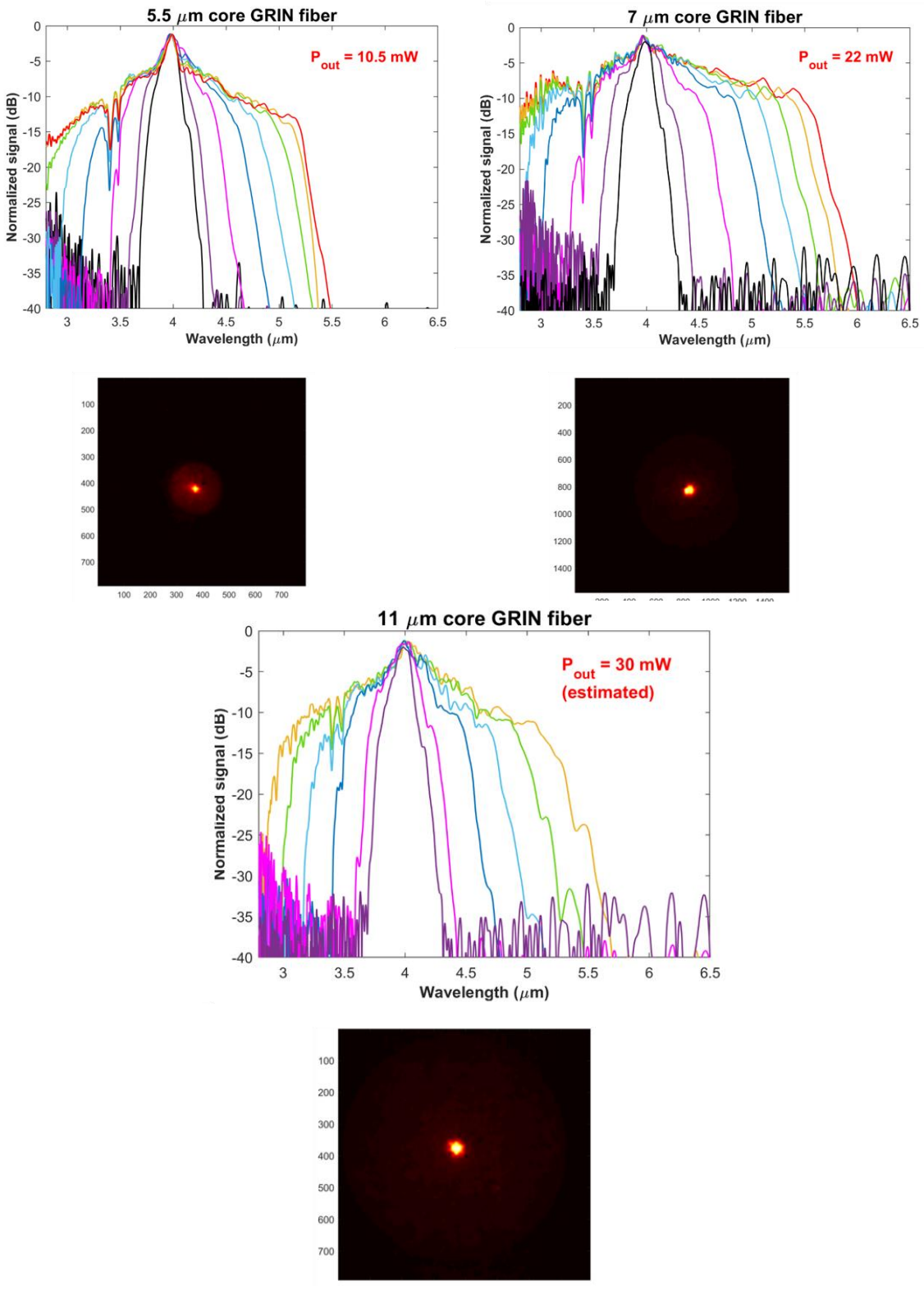

Figure 9. Spectral broadening obtained pumping 5.5 (a), 7 (b) and 10 µm core fiber (c) at 4 µm, using optical parametric generation. with femtosecond pulses and 240 Hz repetition rate with different energy and the corresponding near-field image of the output signal taken with an infrared CCD detector at maximum output power.

To demonstrate the applicability of nGRIN chalcogenide fibers for nonlinear applications, the ~5.6, 7, and 10 µm core fibers were tested for ANDi SCG. For this, we use an Optical Parametric Oscillator (OPO) producing 250 fs pulse at a repetition rate of 240 Hz. Figure 8a shows the output spectrum of the three fibers, corresponding to an average output power of 10.5, 22, and 30 mW, respectively. Despite the higher transmission of the 10 µm core fiber, the 7 µm core fiber was found to produce the broadest spectrum spanning from < 2.6–6 µm. This was attributed to the higher nonlinear coefficient of a fiber with smaller core combined with a flatter dispersion profile near the 4 µm pump wavelength. While the 10 µm core fiber has a lower numerical value of dispersion, the dispersion slope is higher and more importantly the value of the dispersion is continuously increasing up to a wavelength of about 6.5 µm, while the dispersion varies only 6.31 $ps.nm^{-1}.km$ between 4.08 and 10.48 µm in the 7 µm core simulated fiber. The observed spectral broadening dynamics with increased pump power is illustrated in Figure 8b for the 7 µm core fiber. The figure shows the smooth, symmetric broadening typically associated with self-phase modulation and optical wave breaking of femtosecond ANDi SCG dynamics [41]. The output beam was also imaged to confirm confinement of the light to the core of the fiber, as shown in Figure 8c. It is known from previous studies in silica PCFs that such an ANDi continuum can be highly coherent, provided that the noise of the pump laser is fairly low,[11] and the product of the nonlinearity, peak power, and fiber length is maintained at a moderate level [42].

The pump relative intensity noise was measured to be 2.1%, and from the 22 mW average output power the peak power coupled to the fiber was estimated to be around 16.5 kW, taking into consideration the Fresnel reflection at the output facet (22.6% for n= 2.67), and 30 dBm^{-1} propagation loss (6.6 dB for 22 cm fiber length).

Conclusion

Characterization of nanostuctured core graded index fibers made of silica glass in a supercontinuum generation application was conducted and supported with non-linear propagation simulations. We have shown that the nanostucturation of the core by the stack and draw method was particularly adapted to the development of graded index core fiber in chapter 4. It allows to design the dispersion and index distribution profile, as well as the mode area and polarization.

We have first successfully generated a supercontinuum in the anomalous dispersion regime, using a nanosecond 1550 nm laser in silica nGRIN fibers. We observed spectral broadening from 1400 nm to 2300 nm which can be considered typical for the chromatic dispersion profile measured for the used fiber, and for the 1550 nm nanosecond pulse pump laser used in the experiment.

The ability to generate supercontinuum in all-solid nanostructured core fiber was validated and complements results previously obtained [26]. It also confirms that the fiber can withstand high energy pump nanosecond pulses, due to its all-solid structure made of silica. Indeed, it does not have air holes making it easily integrable for industry-accepted pump lasers. It also allows power scaling using large mode area fiber or new supercontinuum laser concepts using multicore fiber based on nanostructrured core fibers. The internal nanostructure of the fiber core does not introduce any additional nonlinear effects related to this discrete core structure and this nanostructured fiber can be treated as an effective optical medium. The single-mode nGRIN fiber used in our experiments was not optimized for hyperspectral

broadening in terms of the zero-dispersion wavelength, but nano-structuring allows large modification of the dispersion profile through modification of the all-solid glass core, which was previously demonstrated by our group using numerical simulations for designing of normal dispersion profiles or shifting of the zero-dispersion wavelength [21, 37]. Thus, the nanostructured core optical fibers have been shown as an alternative in chromatic dispersion engineering in fibers for nonlinear optics applications. The results reported in this work complement the state-of-the-art results available in literature mentioned earlier. We confirmed that the developed nGRIN fiber can withstand high-energy laser pump pulses without laser-induced damage, which we relate to its all-solid glass structure made of silica. Our work opens up new applications in power scaling of supercontinuum lasers using large-mode area fibers and new supercontinuum laser concepts using free-form nanostructured core fibers. Which is why we moved to chalcogenides glasses in the femtoseconds regime to test the validity of this concept to mid-IR glasses like chalcogenides.

We successfully validated the use of femtosecond pulses for chalcogenides glass based nanostructured core GRIN fibers produced by the stack and draw method and obtained a supercontinuum generation in femtoseconds regime from 1 to 7 µm allowing applications in the mid-IR. Due to their inherent lack of thermal stability, all-solid chalcogenide nGRIN fibers by the stack and draw were never produced to date. This proof of concept opens considerable routes to the production of highly engineered fibers as spectroscopic and imagery solutions needing bands covering from 1 µm to 10 µm [43] as well as industry robust sensing solutions.

References

[1] G. Humbert, W. J. Wadsworth, S. G. Leon-Saval, J. C. Knight, T. A. Birks, P. St. J. Russell, M. J. Lederer, D. Kopf, K. Wiesauer, E. I. Breuer, and D. Stifter, "Supercontinuum generation system for optical coherence tomography based on tapered photonic crystal fibre," Opt. Express 14, pp1596-1603 (2006).

[2] D. J. Jones, S. A. Diddams, J. K.Ranka et al, "Carrier-envelope phase control of femtosecond mode-locked lasers and direct optical frequency synthesis.", Science 288, pp635–639 (2000). https://doi.org/10.1126/scien ce.288.5466.635

[3] K. Shi, Li P, S. Yin, Z. Liu, "Chromatic confocal microscopy using supercontinuum light.", Opt Express 12, pp2096-2101 (2004). https://doi.org/10.1364/OPEX.12.00209 6

[4] C. R. Petersen, N. Prtljaga, M. Farries, J. Ward, B. Napier, G. Rhys Lloyd, J. Nallala, N. Stone, and O. Bang, "Mid-infrared multispectral tissue imaging using a chalcogenide fiber supercontinuum source," Opt. Lett. 43, pp999-1002 (2018).

[5] C. Kaminski, R. Watt, A. Elder, J. H. Frank, J. Hult, "Supercontinuum radiation for applications in chemical sensing and microscopy", Appl. Phys. B 92 pp367-378 (2008). https://doi.org/10.1007/s00340-008-3132-

[6] R. R. Alfano, S. L. Shapiro, "Emission in the region 4000–7000 Å via four-photon coupling in glass.", Phys Rev Lett 24, pp584–587 (1970a). https ://doi.org/10.1103/PhysR evLet t.24.584

[7] R. R. Alfano, S. L. Shapiro, "Observation of self-phase modulation and small-scale filaments in crystals and glasses.", Phys Rev Lett 24, pp592–594 (1970b). https://doi.org/10.1103/PhysR evLet t.24.592

[8] J. M. Dudley, G. Genty, S. Coen, "Supercontinuum generation in photonic crystal fiber.", Rev Mod Phys 78, pp1135–1184 (2006). https://doi.org/10.1103/RevMo dPhys .78.1135

[9] M. Klimczak, B. Siwicki, A. Heidt, R. Buczyński, "Coherent supercontinuum generation in soft glass photonic crystal fibers.", Photonics Res 5, pp710-727 (2017). https://doi.org/10.1364/PRJ.5.00071 0

[10] B. Wetzel, M. Kues, P. Roztocki P et al., "Customizing supercontinuum generation via on-chip adaptive temporal pulse-splitting.", Nat Commun 9, pp4884 (2018). https://doi.org/10.1038/s4146 7-018-07141 -w

[11] E. Genier, P. Bowen, T. Sylvestre, J. M. Dudley, P. Moselund, O. Bang, "Amplitude noise and coherence degradation of femtosecond supercontinuum generation in all-normal-dispersion fibers.", J Opt Soc Am B 36, pp161-167 (2019). https://doi.org/10.1364/JOSAB .36.00A16 1

[12] J. K. Ranka, R. S. Windeler, A. J. Stentz, "Visible continuum generation in air–silica microstructure optical fibers with anomalous dispersion at 800 nm.", Opt Lett 25, pp25-27 (2000). https://doi.org/10.1364/OL.25.00002 5

[13] X. Jiang, N. Y. Joly, M. A. Finger, F. Babic, G. K. L. Wong, J. C. Travers, P. St. J. Russell, "Deep-ultraviolet to midinfrared supercontinuum generated in solid-core ZBLAN photonic..crystal fibre.", Nat Photonics 9, pp133–139 (2015). https://doi.org/10.1038/nphot on.2014.320

[14] D-P. Wei, T.V. Galstian, I. V. Smolnikov et al., “Spectral broadening of femtosecond pulses in a single-mode As–S glass fiber.”, Opt. Express 13, pp2439 (2005). https://doi.org/10.1364/opex.13.00243 9

[15] L. Liu, T. Cheng, K. Nagasaka et al., “Coherent mid-infrared supercontinuum generation in all-solid chalcogenide microstructured fibers with all-normal dispersion.”, Opt Lett 41, pp392 (2016). https://doi.org/10.1364/OL.41.00039 2

[16] M. Śmietana, M. Koba, P. Mikulic, W. J. Bock, “Towards refractive index sensitivity of long-period gratings at level of tens of µm per refractive index unit: fiber cladding etching and nano-coating deposition.”, Opt Express 24, pp11897 (2016). https ://doi.org/10.1364/OE.24.01189 7

[17] I. Kujawa, P. Szarniak, R. Buczynski, D. Pysz, R. Stepien, "Development of all-solid photonic crystal fibers," Proc. SPIE 6182, Photonic Crystal Materials and Devices III (i.e. V), 61822Q (April 2006);

[18] M. Klimczak, B. Siwicki, P. Skibiński, D. Pysz, R. Stępień, A. Heidt, C. Radzewicz, and R. Buczyński, "Coherent supercontinuum generation up to 2.3 µm in all-solid soft-glass photonic crystal fibers with flat all-normal dispersion.", Opt. Express 22, pp18824-18832 (2014).

[19] K. Oh and U. C. Paek, ”Silica Optical Fiber Technology for Devices and Components: Design, Fabrication, and International Standards.”, Wiley; 1 edition, Hoboken, USA (2012).

[20] F. Hudelist, R. Buczynski, A. J. Waddie, M. R. Taghizadeh, “Design and fabrication of nano-structured gradient index microlenses.”, Opt. Express 17, pp3255–3263 (2009).

[21] B. Siwicki, A. Filipkowski, R. Kasztelanic, M. Klimczak, and R. Buczyński, "Nanostructured graded-index core chalcogenide fiber with all-normal dispersion–design and nonlinear simulations.", Opt. Express 25, pp12984-12998 (2017).

[22] R. Kasztelanic, A. Filipkowski, A. Anuszkiewicz, *et al.*, "Integrating Free-Form Nanostructured GRIN Microlenses with Single-Mode Fibers for Optofluidic Systems.", *Sci Rep* 8, pp5072 (2018). doi:10.1038/s41598-018-23464-6

[23] T. Kato, Y. Suetsugu, and M. Nishimura, "Estimation of nonlinear refractive index in various silica-based glasses for optical fibers.", Opt. Lett. 20, pp. 2279-2281 (1995).

[24] M. Franczyk, K. Stawicki, J. Lisowska, D. Michalik, A. Filipkowski, R. Buczyński, "Numerical studies on large-mode area fibers with nanostructured core for fiber lasers," J. Lightwave Technol. 36, pp5334-5343 (2018).

[25] M. Franczyk, R. Stepień, A. Filipkowski, D. Pysz and R. Buczyński, "Nanostructured core active fiber based on ytterbium doped phosphate glass.", *Journal of Lightwave Technology*. doi: 10.1109/JLT.2019.2941664

[26] A. Antikainen and G. Agrawal, "Supercontinuum generation in seven-core fibers.", J. Opt. Soc. Am. B 36, pp2927-2937 (2019).

[27] A. Anuszkiewicz, R. Kasztelanic, A. Filipkowski *et al.*, "Fused silica optical fibers with graded index nanostructured core.", *Sci Rep* 8, pp12329 (2018). doi:10.1038/s41598-018-30284-1

[28] X. Forestier, T. Karpate, G. Huss *et al., "*Supercontinuum generation in nanostructured core gradient index fibers.", *Appl Nanosci* 10, pp1997–2005 (2020). https://doi.org/10.1007/s13204-020-01319-9

[29] M. Meneghetti, X. Forestier, C. R. Petersen, R. Kasztelanic, M. Klimczak, O. Bang, R. Buczyński, J. Troles, "Graded Index Chalcogenide Fibers with Nanostructured Core.", Adv. Photonics Res. 2, pp2000091 (2021). https://doi.org/10.1002/adpr.202000091

[30] J. W. Fleming, "Dispersion in GeO_2–SiO_2 glasses", Appl Opt 23, pp4486 (1984). https://doi.org/10.1364/AO.23.00448 6

[31] I. H. Malitson, "Interspecimen comparison of the refractive index of fused silica.", J Opt Soc Am 55, pp1205 (1965). https ://doi.org/10.1364/JOSA.55.00120 5

[32] S. Kirkpatrick, C. D. Gelatt, M. P. Vecchi, "Optimization by simulated annealing.", Science 220, pp671–680 (1983). https ://doi.org/10.1126/scien ce.220.4598.671

[33] F. Hudelist, R. Buczynski, A. J. Waddie, M. R. Taghizadeh, "Design and fabrication of nano-structured gradient index microlenses.", Opt Express (2009). https ://doi.org/10.1364/oe.17.00325 5

[34] M. D. Nielsen, C. Jacobsen, N. A. Mortensen et al., "Low-loss photonic crystal fibers for transmission systems and their dispersion properties.", Opt Express 12, pp1372 (2004). https ://doi.org/10.1364/OPEX.12.00137 2

[35] A. Demircan, U. Bandelow, "Supercontinuum generation by the modulation instability.", Opt Commun 244, pp181–185 (2005). https ://doi.org/10.1016/J.OPTCO M.2004.09.049

[36] J. M. Dudley, G. Genty, F. Dias et al., "Modulation instability, Akhmediev breathers and continuous wave supercontinuum generation.", Opt Express 17, pp21497 (2009). https://doi.org/10.1364/OE.17.02149 7

[37] D. Michalik, T. Stefaniuk, R. Buczyński, "Dispersion management in hybrid optical fibers.", J Lightwave Technol. (2019). https ://doi.org/10.1109/JLT.2019.29522 50

[38] N. M. Israelsen, C. R. Petersen, A. Barh et al., "Real-time high-resolution mid-infrared optical coherence tomography.", Light Sci Appl 8, pp11 (2019). https ://doi.org/10.1038/s4137 7-019-0122-5

[39] M. Eftekhar, Z. Sanjabi-Eznaveh, H. Lopez-Aviles, S. Benis, J. AntonioLopez, M. Kolesik, F. Wise, R. Amezcua-Correa, D. Christodoulides, Nat. Commun., 10, 1 (2019).

[40] K. Krupa, C. Louot, V. Couderc, M. Fabert, R. Guénard, B. Shalaby, A. Tonello, D. Pagnoux, P. Leproux, A. Bendahmane, R. Dupiol, Opt. Lett., 41, pp5785 (2016).

[41] A. M. Heidt, A. Hartung, G. W. Bosman, P. Krok, E. G. Rohwer, H. Schwoerer, H. Bartelt, Opt. Express, 19, pp3775 (2011).

[42] I. B. Gonzalo, R. D. Engelsholm, M. P. Sørensen, O. Bang, Sci. Rep., 8, 1 (2018).

[43] C. Poudel and C. F. Kaminski, "Supercontinuum radiation in fluorescence microscopy and biomedical imaging applications," J. Opt. Soc. Am. B 36, pp139-153 (2019).

CONCLUSION AND OUTLOOK

In this thesis, I addressed the difficulty of synthesizing heavy metal oxide glasses with high thermal stability and appropriate mid-IR properties needed to develop optical components. Indeed, glasses tend to crystallize with the thermal treatments involved in the production of lenses, PCFs and nGRINs due to the glass working temperature being close to the crystallization temperature. The more heat treatments are involved in the production, the more stable the glass needs to be. This is especially true for nanostructured all-solid fibers, and lenses produced by hot embossing involving multiple thermally intensive treatments. The possibility to generate supercontinuums in all-solid nanostructured core nGRIN optical fibers was also explored using nanoseconds to femtoseconds regimes for very different families of glasses, silica and chalcogenides.

Highly stable new soft glasses were first developed within the SiO_2-PbO-CdO-Ga_2O_3 system to produce lenses by the hot-embossing method. A large number of compositions were investigated, and the best glass was selected. This glass system has shown to be particularly adapted to produce lenses and optical fibers for mid-IR applications due to its high thermal stability and its optical properties. Lenses were successfully produced and measured, opening the way to the production of cost-effective lenses for applications from visible to 5 µm.

In a second time, the validity of tellurites glasses purification to extend the transmission of optical fibers produced by the stack and draw method was tested. For this purpose, TeO_2-ZnO-Na_2O, was synthetized in a glove box with a controlled atmosphere and halides compounds to reduce the amount of water contained in the glass to extend its transmission range to 5.5 µm. We have confirmed that it was an effective way to drastically reduce the absorption bands located above 3.0 µm. However, the production of optical fibers was unsuccessful due to the decreased thermal stability of tellurites. We have concluded that this type of tellurite glasses, purified with halides, was not appropriate to produce optical fibers by the stack and draw method. For further studies about tellurites fibers, I strongly suggest synthetizing in house TeO_2 to achieve high purity compounds. The use of reactive gases such as fluorine could also be an interesting drying pre-step to take to drastically reduce the water content in tellurite glasses to extend the transmission up to 5.5 µm in meters long optical fibers. Concerning the inherent thermal instability of fluorotellurites, it seems that the extrusion method is the only way to date to produce extended transmission, low OH, tellurites PCFs and that the multiple heat treatments involved with the stack and draw method make the use of this type of glass system impossible this way.

In a collaboration with the University of Rennes 1, highly stable chalcogenides glasses within Ge-As-Se system synthetized by the glass and ceramic department in Rennes were used to develop the first example of chalcogenide graded index fibers for applications above 6 µm, using the stack and draw method to obtain a nanostructured all-solid core composed by hundreds of elements. The parabolic profile of the refractive index was obtained designing the distribution of the elements composing the core of the fiber made of two glasses with different refractive indexes. Transmission from 1 µm to 11 µm was observed in the produced fibers, however, the optical losses are two orders of magnitude larger than the bulk glasses. Possible ways to decrease the attenuation are being investigated. Simulations performed for the various fibers show the great versatility in the dispersion profile management, allowing the possibility to have flat

ANDi profile over the whole mid-IR region. This new method can also be used to produce chalcogenides-based multicore fibers and polarization maintaining fibers.

Using the method to make nGRINs, chalcogenide graded index microlenses were produced for the first time, with a transmission theoretically spanning from 1 µm up to 17 µm based on the transmission spectra and the attenuation of the bulk glass. The development of broadband infrared transmission graded index chalcogenides-based microlenses could enable new coupling and imaging systems.

Finally, the possibility to generate supercontinuum in nanostructured core nGRIN fibers was investigated. We first tried to pump silica nGRIN silica fibers with nanosecond pulses in normal dispersion regime and successfully obtained spectral broadening from 1.45 µm to 2.2 µm. Considering the success on silica, the chalcogenides fibers developed in Chapter 4 were used for SCG. Using an OPO, the nGRINs were pumped in ANDi regime with femtosecond pulses at 4 µm. Spectral broadening was observed for the first time for this type of new chalcogenide fibers, from 1 µm to 6 µm. This opens the possibility to the development of robust all-solid fiber sources for the mid-IR supercontinuum. The high compactness, brightness, and spatial coherence of this type of fiber as well as the versatility of use for example for spectroscopy, remote sensing, microscopy, and tomography can enable progress in many fields.

Acknowledgment

This project has received funding from the European union's Horizon 2020 research and innovation program SUPUVIR, under Grant Agreement No 722380.

Annex 1 Sellmeiers coefficients

	Sellmeier coefficients					
	B1	B2	B3	C1	C2	C3
SPCG1B	2.2860004	0.2676274	0.3363165	0.0195302	0.0862373	58.4360
SPCG2B	2.2934904	0.3122492	0.0962427	0.0144952	0.0995960	34.5907
SPCG3B	2.2496469	0.4128865	1.8550755	0.0191284	0.0738834	207.1074
SPCG4B	2.2879307	0.3843901	4.0000000	0.0259877	0.0576978	295.0608
SPCG5B	2.2832089	0.4251855	2.0558794	0.0190812	0.0789427	250.0000
SPCG0C	2.2260472	0.4580070	0.1151607	0.0161229	0.0736734	21.4515
SPCG1C	2.2065901	0.4374321	0.1308677	0.0178881	0.0749653	24.0461
SPCG3C	2.0058902	0.6685237	0.2016625	0.0144459	0.0673399	34.2226
SPCG4C	2.1276564	0.5839574	1.5320049	0.0159745	0.0728240	214.3810
SPCG5C	2.5992090	0.1272097	2.4008329	0.0258130	0.1132925	270.5981
SPCG0D	2.1585834	0.3944738	0.2863098	0.0167787	0.0715992	41.2875
SPCG1D	2.0008162	0.5652997	2.4000215	0.0140470	0.0653053	297.4703
SPCG2D	2.3015259	0.2754106	1.0046092	0.0190429	0.0844385	135.9643
SPCG3D	2.3975935	0.2000000	0.2449257	0.0213246	0.0918612	36.9704
SPCG4D	2.4000000	0.2464867	0.0657511	0.0198281	0.0932517	17.3433
SPCG5D	2.0443259	0.6266668	0.5674441	0.0146371	0.0691784	79.8454

List of figures

Chapter 1

Chapter 2

Chapter 3

Chapter 4

Chapter 5

List of tables

Chapter 1

Chapter 3

Chapter 4